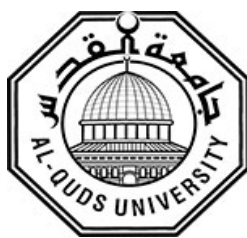


DEANSHIP OF GRADUATE STUDIES

AL_QUDS UNIVERSITY



JAMILA

Joint mAsTer of MEDITERRANEAN IInitiatives on renewAbLe and sustainAbLe
energy

Macroscopic magnetic properties and magnetocaloric effect in single crystalline Mn_5Si_3 and derived compounds

Nour Thabet Ahmad Abboushi

M.Sc. Thesis

Jerusalem-Palestine

1442 / 2021

**Macroscopic magnetic properties and magnetocaloric effect in
single crystalline Mn_5Si_3 and derived compounds**

Nour Thabet Ahmad Abboushi

Supervisors

Dr. Husain Alsamamra

Physics Department, Al-Quds University, Palestine

apl. Prof. Dr. Karen Friese

Jülich Centre for Neutron Science-2, Forschungszentrum Jülich,
Germany

Dr. Jörg Voigt

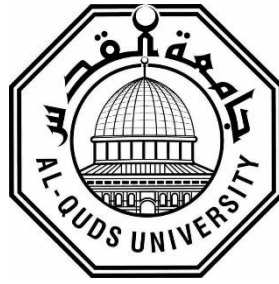
Jülich Centre for Neutron Science, Forschungszentrum Jülich,
Germany

A thesis submitted in partial fulfillment of requirements for the degree of master of science in
Renewable Energy & Sustainability

Al-Quds University

Palestine Polytechnic University

1442/2021



Al-Quds University

Deanship of Graduate Studies

Renewable Energy & Sustainability

Thesis approval

Macroscopic magnetic properties and magnetocaloric effect in single crystalline Mn_5Si_3 and derived compounds

Nour Thabet Ahmad Abboushi

Registration No.: 21812552

Supervisors

Dr. Husain Alsamamra, Physics Department, Al-Quds University, Palestine.

apl.Prof. Dr. Karen Friese, Jülich Centre for Neutron Science-2, FZ Jülich, Germany.

Dr. Jörg Voigt, Jülich Centre for Neutron Science, FZ Jülich, Germany.

Master thesis submitted and accepted, Date: 24 / 5 / f2021

The names and signatures of the examining committee members as follows:

- | | |
|--|-----------|
| 1- Head of Committee: Dr. Husain Alsamamra | Signature |
| 2- Internal Examiner: Dr. Omar Ayyad | Signature |
| 3- External Examiner: Dr. Mustafa Abu Safa | Signature |

Jerusalem-Palestine

1442 / 2021

Dedication

With the spirit of gratitude, I dedicate this work to the love of my life, Dr. Nasr Abboushi and my three children, Kinda, Younis, and Kinan. They have borne a great burden during my absence and my preoccupation with work.

To the three women in my life, my mother Sadaa, who raised me on human values, and to my two sisters Ola and Sabreen.

To my father soul.

To my friends in Germany, Deema, and Fatima, who have given me the warmth of the family.

To my homeland, Palestine, the land of peace, which has never seen the peace.

To Gaza, where dreams grow and nightmares fall.

To all the patient and strong Palestinian women, I know how many challenges we face, but we always win.

With my love,

Nour

Declaration

I, Nour Ahmad Abboushi, certify that this thesis “**Macroscopic magnetic properties and magnetocaloric effect in single crystalline Mn_5Si_3 and derived compounds**” is submitted for the degree of M. Sc., is the result of my own research based on the results found by myself. Materials of works found by other researchers are mentioned by references, except where otherwise acknowledged, and that this thesis, neither in whole nor in part, has been previously submitted for any degree to any other university or institution.

I declare that this work was done under the supervision of Dr. Husain Alsamamra, from the Physics Department, Al-Quds University, Palestine, and apl.Prof. Dr. Karen Friese, Jülich Centre for Neutron Science-2, FZ Jülich, Germany, and Dr. Jörg Voigt, Jülich Centre for Neutron Science, FZ Jülich, Germany¹.

Nour Thabet Ahmad Abboushi

Date: 24 / 05 / 2021

¹ This project is part of a collaborative effort under the framework collaboration between FZ-Jülich Research Center, Germany, and Al-Quds University, Palestine, and coordinated by Karen Friese, Jülich Centre for Neutron Science CNS-2 and Husain Alsamamra from the Department of Physics.



Acknowledgements

I offer my thanks and gratitude to all people that “Allah” put on my way to guide me to the end.

First, I would like to thank the **PALGER funding programme** that gave me this opportunity among the project number 01DH17013.

I’m grateful to Dr. Husain Alsamamra who nominated me as a beneficiary of the mutual scientific cooperation between Al-Quds University and the FZ- Jülich Research Centre.

Special thanks to Prof. Dr. Thomas Brückel for his generosity and support, as he is the head of the JCNS-2/PGI-4.

I would like to thank apl. Prof. Dr. Karen Friese who gave me the opportunity to work with her team. In addition to her wise guidance during the research period, and her constant work of improving my scientific writing.

I don’t know how to express my deep thanks and appreciation for Dr. Jörg Voigt, my scientific advisor. He supervised, instructed, and taught daily with great patient and generosity. He taught me how to solve the problems, without forbidding me to solve them by myself.

I want to say thanks to DP. Jörg Persson for helping in preparing the samples.

I’m grateful to all my colleagues at the JCNS-2, they are really wonderful and hospital people.

I don’t forget to extend my thanks to miss Barbara Daegerer for her support in the administrative matters.

Place of experimental work

The experimental work of this thesis was performed at the Jülich Center for Neutron Science at the Forschungszentrum Jülich GmbH in Germany.

The Jülich Centre for Neutron Science JCNS design and operates instruments at the national and international leading neutron sources FRM II, ILL and SNS. JCNS provides external users with access to world class instruments at the neutron source best suited for their respective experiments. The research in the center focuses on nano-magnetism, soft matter, correlated electron systems, functional materials and biophysics.

This work was performed at the Jülich Centre for Neutron Science-2 *Quantum Materials and Collective Phenomena*.



Jülich Center for Neutron Science (JCNS)

Abstract

Recently, the magnetocaloric effect (MCE) has been extensively studied theoretically and experimentally, not only because of its potential for application in magnetic refrigeration technologies, but also to gain a more solid understanding of the physical properties of the materials. The magnetic refrigeration is a promising, energy-efficient technology and may be an alternative to the conventional compression-expansion gas cycle refrigeration in the future, as it has less environmental impact due to the fact that no greenhouse or ozone-depletion gases have to be used.

The MCE is a thermodynamic phenomenon in which the magnetic entropy is changed in an isothermal process, or the temperature of the material is changed in an adiabatic process, when it is exposed to a magnetic field. There are two main quantities that characterize the MCE of a material: the change in temperature in an adiabatic process ΔT_{ad} , and the change in magnetic entropy in an isothermal process ΔS_M .

Magnetocaloric Mn_5Si_3 has received special attention with respect to its magnetic properties. It shows two first-order transitions to two antiferromagnetic phases AFM1 and AFM2, at 66 K and 99 K respectively. Another intermediate magnetic configuration AFM1' occurs if a magnetic field is applied, through which the compound transforms from the AFM1 phase to the AFM2 state. Interestingly, the first magnetic transition around 99 K is associated with a structural transition, at which the symmetry of the crystal structure changes from hexagonal to orthorhombic. Moreover, this compound exhibits a less common type of MCE which is named inverse MCE. This effect is associated with the phase transition between the two antiferromagnetic phases AFM2-AFM1 where the spin arrangement changes from collinear to non-collinear magnetic order.

In this thesis, the direction dependent macroscopic magnetic properties of a single crystal of Mn_5Si_3 were investigated using the Vibrating Sample Magnetometer (VSM) option. The mass magnetization measurements were performed with the magnetic field applied along the three different crystallographic directions a, b and c of the orthorhombic unit cell of the low temperature structure. The magnetization measurements were performed for every sample under two different protocols, the isothermal and the isofield conditions

Five main observations were obtained from field and temperature dependent magnetization curves. (i) Low temperature-low magnetic field features were observed for application of the field parallel to the orthorhombic base vectors

(ii) Features which are associated with the phase transition of AFM1' - AFM2.

(iii) Features in the high temperature -low magnetic field region when the magnetic field is applied in the ab-plane.

(iv) Features that can be attributed to the transition from AFM1 to the AFM1' phase. These are only observed when the magnetic field is applied parallel to the c-direction.

(v) Features corresponding to the transition from the PM phase to the AFM2 state. These can only be observed, when small fields are applied || to the b-direction.

Based on these observations a field-temperature phase diagram could be obtained and it can be concluded that the magnetic response of the sample is strongly affected by the direction of the applied magnetic field. Our results show clearly that the magnetic response in the low temperature phase AMF1 depends strongly on the field direction and is more complex than previously thought. This complexity can most probably be mainly attributed to the existence of two different crystallographic sites for the Mn ions within the crystal structure and the mutual magnetic interactions between them.

Moreover, the magnetic entropy change ΔS_M of Mn_5Si_3 was extracted based on Maxwell relation between entropy/temperature and magnetization/field, which allows the calculation from the field-dependent of the isothermal entropy change from magnetization data. The compound exhibits an inverse MCE which corroborates the prevalence of AFM interactions. A switch of the sign of magnetic entropy occurs around the transition temperature from the non-collinear AFM1 to the collinear AFM2 phase. The maximum positive value of ΔS_M is roughly 3.5 J/kg. K for a field change of 5.0 T at approximately 60 K.

Regarding the $(Mn_5Ge_3)_x(MnFe_4Si_3)_{1-x}$ compound in powder form, there was a doubt about the reliability of earlier magnetization results for the sample with $x = 0.8$. According to the earlier investigations, the saturation magnetization value exceeded $250 Am^2Kg^{-1}$ at 20 K, compared to the much lower saturation magnetization of approximately $100 Am^2Kg^{-1}$ for the other samples with $x = 0.6, 0.4, 0.2$. To check this observation, a polycrystalline sample of $Mn_{4.2}Ge_{2.4}Fe_{0.8}Si_{0.6}$ was re-synthesized and x-ray powder diffraction was used to confirm the phase purity of the compound. Afterwards, the magnetization was re-measured by performing isofield measurements with two modes: field cooling (FC) and field warming (FW), and isothermal measurements over a temperature range from 350 to 20 K. We find that the saturation magnetization at 20 K is around $100 Am^2Kg^{-1}$ as expected, and that evidently the formerly reported value of $250 Am^2Kg^{-1}$ is erroneous.

Table of contents

Declaration.....	v
Acknowledgments.....	vi
Place of experimental work.....	vii
Abstract.....	viii
List of tables.....	xii
List of figures.....	xii
List of abbreviations.....	xvi
1 Introduction.....	1
1.1 Motivation.....	1
2 Theory.....	3
2.1 The magnetocaloric effect (MCE).....	3
2.1.1 History and definition.....	3
2.2 Thermodynamics of the MCE.....	5
2.3 Inverse MCE.....	7
2.4 Determination of MCE.....	8
2.4.1 Direct determination of MCE.....	8
2.4.2 Indirect determination of MCE.....	9
2.5 Scattering basics and diffraction techniques.....	9
2.5.1 X-ray powder diffraction.....	11
2.5.2 Laue single crystal diffraction.....	11
2.5.3 The Le Bail method.....	12
3 The magnetocaloric materials of this work.....	14
3.1 Introduction.....	14
3.2 The intermetallic compound Mn_5Si_3	16
3.2.1 Crystal structure of Mn_5Si_3	16
3.2.2 Magnetic structures of Mn_5Si_3	18
3.2.3 Summary of macroscopic magnetization measurements on Mn_5Si_3 as described in the literature.....	20
4 Instrumentation.....	26
4.1 Cold crucible induction melting device.....	26

4.2	The MWL120 real-time back-reflection Laue camera.....	27
4.3	Huber G670 powder diffractometer	28
4.4	Vibrating sample magnetometer (VSM) of physical property measurement system (PPMS).....	29
5	Experimental procedures.....	31
5.1	Experimental part concerning Mn_5Si_3 samples.....	31
5.1.1	Sample preparation	31
5.1.1.1	Sample synthesis and single crystal growth	31
5.1.1.2	Laue diffraction experiment using MWL120 camera	31
5.1.2	Magnetization measurements.....	33
5.1.2.1	Iso-field magnetization measurements.....	33
5.1.2.2	Iso-thermal magnetization measurements	35
5.2	Experimental part corresponding to the $Mn_{4.2}Ge_{2.4}Fe_{0.8}Si_{0.6}$ sample	36
5.2.1	Sample preparation	36
5.2.1.1	Synthesis of the polycrystalline sample of $Mn_{4.2}Ge_{2.4}Fe_{0.8}Si_{0.6}$	36
5.2.1.2	X-ray powder diffraction using Huber G670 diffractometer	37
5.2.2	Magnetization measurements.....	40
5.2.2.1	Iso-field and iso-thermal magnetization measurements	41
6	Data analysis (results and discussions).....	42
6.1	Laue diffraction of Mn_5Si_3 single crystal samples	42
6.2	The LeBail refinement of $Mn_{4.2}Ge_{2.4}Fe_{0.8}Si_{0.6}$ powder diffraction data.....	46
6.3	Magnetization measurements on Mn_5Si_3	49
6.3.1	Magnetization measured under isofield conditions	49
6.3.2	Magnetization measured under isothermal conditions	53
6.3.2.1	Magnetization measurements with H applied to the a- and b-direction	53
6.3.2.2	Magnetization measurements of H c-direction	58
6.3.3	Characterization of the MCE.....	64
6.4	Magnetization measurements on $Mn_{4.2}Ge_{2.4}Fe_{0.8}Si_{0.6}$	68
6.4.1	The previous work results.....	68
6.4.2	Results of the measurements performed in the course of this thesis.....	70
7	Conclusions and Outlook	72
	References	76

List Of Tables

	page
Table 3.1: Crystallographic data of Mn_5Si_3 .	16
Table 6.1: The initial unit cell parameters and the parameters from the LeBail refinements of the patterns measured with the Huber diffractometer of $Mn_{4.2}Ge_{2.4}Fe_{0.8}Si_{0.6}$ powder sample.	48
Table 7.1: Summary of the main anomalies observed in the isothermal and isofield magnetization measurements that were performed on the single crystal of Mn_5Si_3 .	73

List Of Figures

Chapter 2		page
Figure 2.1: (left) The adiabatic magnetization, (right) The adiabatic demagnetization.		4
Figure 2.2: S-T diagram of MCE.		6
Figure 2.3: Bragg's Law is represented as schematic illustration.		10
Figure 2.4: Schematic drawing of Debye-Scherrer cones.		12
Chapter 3		
Figure 3.1: (left) Sketch of a magnetic phase diagram of the system $Mn_{5-x}Fe_xSi_3$ ($x = 0,1,2,3,4,5$), (right) The magnetic entropy change for a field change of 2T and 5T.		14
Figure 3.2: Mn_5Si_3 hexagonal unit cell projected along [001], green spheres represent Mn ions, red ones represent Si ions.		17
Figure 3.3: Projection of the crystal structure of Mn_5Si_3 along [001]. The hexagonal unit cell and orthorhombic unit cell are presented with bold lines.		17
Figure 3.4: The magnetic structure of Mn_5Si_3 . (1) The collinear AFM2 Phase. (2) The non-collinear AFM1 phase. (3) The non-collinear AFM1' phase.		19
Figure 3.5: Magnetic phase diagram of Mn_5Si_3 .		21
Figure 3.6: Magnetic phase diagram of Mn_5Si_3 .		22
Figure 3.7: Isothermal magnetization curves of Mn_5Si_3 from (2-100) K.		23
Figure 3.8: Isothermal magnetization curves of Mn_5Si_3 . σ_a, σ_b represents the magnetization values in the non-collinear and collinear phases respectively.		23
Figure 3.9: The magnetic entropy change ($-\Delta S_M$) of the Mn_5Si_3 compound.		25

Chapter 4		
Figure 4.1: (left) Scheme of a cold crucible induction melting apparatus (Schematic view), (right) photo of the CCIM devise at the JCNS-2.		26
Figure 4.2: (left) A sketch of the MWL120 camera, (right) A photo of the MWL120 camera at JCNS-2 which was used in this work.		28
Figure 4.3: (left) Schematic view of the G670 diffractometer, (right) Huber G670 Powder Diffractometer at JCNS-2.		29
Figure 4.4: (left) Schematic View of VSM option, (right)PPMS Dynacool at JCNS-2.		30
Chapter 5		
Figure 5.1: (a) Fixing the sample on the holder. (b) Inserting the holder inside the MWL120 Laue camera. (c) The samples cut with spark erosion. (d) An image for Mn_5Si_3 single crystal along [001] axis obtained from the Laue camera. (e) The three oriented samples of Mn_5Si_3 along [100], [1-20] and [001] axis.		32
Figure 5.2: (a) Fixing the sample on the holder at a specific location using the mounting station, the red arrow is pointing to the sample. (b) The sample after Teflon covering. (c) The dialogue for the sample centering scan.		35
Figure 5.3: (left) The containers of the high purity elements of Mn , Ge , Fe , Si , (right) Cold Crucible Induction Melting device, (right) The glowing sample is visible.		37
Figure 5.4: (a) Polycrystalline sample as obtained from CCIM. (b) Crushed sample inside a mortar. (c) Final fine homogenous powder of $Mn_{4.2}Ge_{2.4}Fe_{0.8}Si_{0.6}$ compound.		38
Figure 5.5: (left) Powder sample inserted in sample holder to be used in x-ray diffraction experiment, (right) The Huber G670 diffractometer system in JCNS-2.		39
Figure 5.6: Trough-shaped holder in which the capsule of the sample is inserted, the red arrow is pointing to the sample.		41
Chapter 6		
Figure 6.1: (top) The calculated stereographic projection based on the lattice parameter from an Mn_5Si_3 single crystal along the [100] direction as obtained from the OrientExpress 3.4 program. (bottom) The real-time Laue camera image along the same crystallographic direction.		43
Figure 6.2: (top) The calculated stereographic projection based on the lattice parameter from an Mn_5Si_3 single crystal along the [120] direction as obtained from the OrientExpress 3.4 program. (bottom) The real-time Laue camera image along the same crystallographic direction.		44

Figure 6.3: The real-time Laue camera image along the [001] direction of Mn_5Si_3 .	45
Figure 6.4: The LeBail fit of the room temperature data of $Mn_{4.2}Ge_{2.4}Fe_{0.8}Si_{0.6}$ using two phases and the resulting difference profile from Jana2006.	47
Figure 6.5: Molar magnetic susceptibility of Mn_5Si_3 single crystal with fields of varying strength applied along the different crystallographic directions.	50
Figure 6.6: (top) The isofield magnetization curves $M(T)$ of the three crystallographic directions, at $H = 1.5$ T and at $H = 7.5$ T (bottom).	52
Figure 6.7: The field-dependent magnetization curves ($M(B)$) of Mn_5Si_3 . Decreasing H data, $H \parallel b$ -direction, in the temperature range 10 K - 120 K.	54
Figure 6.8: The first derivative of the $M(B)$ curves, (dM/dB) vs. (B).	55
Figure 6.9: (dM/dT) for the magnetization data of Mn_5Si_3 single crystal as a function of applied magnetic field and temperature, $H \parallel b$ -direction. Shades of red and blue represent the positive and negative (dM/dT) of the sweeping down data respectively.	57
Figure 6.10: The field-dependent magnetization curves ($M(B)$) of Mn_5Si_3 . Decreasing H data, $H \parallel c$ -direction, in the temperature range 10 K - 76 K.	59
Figure 6.11: The (dM/dB) vs. (B) curves of Mn_5Si_3 , $H \parallel c$ – direction, for three temperature ranges, (bottom) $T < 25$ K, (middle) $25 < T(K) < 41$, and (top) $41 < T(K) < 63$.	60
Figure 6.12: The (dM/dT) of the magnetization data of Mn_5Si_3 single crystal as a function of the magnetic field applied \parallel to the c-direction and the temperature. Shades of red and blue represent positive and negative (dM/dT) of the sweeping down data respectively.	62
Figure 6.13: The Isofield magnetization data at 0.5 T, with the field applied \parallel to the three different directions a, b, and c. The dots in orange and blue correspond to the magnetization data which are extracted from the isothermal measurements at 0.5 T during increase and decrease of the magnetic field respectively.	63
Figure 6.14: Magnetic entropy change ($-\Delta S_M$) of Mn_5Si_3 as a function of temperature, for a field change of 5.0 T; (left) $H \parallel b$, (right) $H \parallel c$.	66
Figure 6.15: Magnetic entropy change ($-\Delta S_M$) of Mn_5Si_3 as a function of temperature, for a field change of 1.0 T; (left) $H \parallel a$, (right) $H \parallel b$ -direction.	67
Figure 6.16: Isofield magnetization measurements of the compounds in the system $(Mn_5Ge_3)_x(MnFe_4Si_3)_{1-x}$ measured in $\mu_0 H = 0.1$ T, FC mode is the blue color, FW mode is the red color.	69

Figure 6.17: Isothermal magnetization measurements of the compounds in the system $(Mn_5Ge_3)_x(MnFe_4Si_3)_{1-x}$. Full hysteresis measurements ($\pm 8 T$) are shown.	69
Figure 6.18: Field-dependent magnetization data of a polycrystalline sample of $Mn_{4.2}Ge_{2.4}Fe_{0.8}Si_{0.6}$ in the temperature range from 350 K to 20 K.	70
Figure 6.19: Temperature-dependent magnetization data of a polycrystalline sample of $Mn_{4.2}Ge_{2.4}Fe_{0.8}Si_{0.6}$ at a magnetic field setting of 0.1 T.	71
Chapter 7	
Figure 7.1 The (dM/dB) vs. (B) curves for the a, b, and c-direction.	74

List Of Abbreviations

Abbreviation	Representation
MCM	Magnetocaloric material
MCE	Magnetocaloric effect
AFM	Antiferromagnetic
FIM	Ferrimagnetic
PM	Paramagnetic
FM	Ferromagnetic
T_C	Curie Temperature
T_N	Néel temperature
SOPT	Second order magnetic phase transition materials
FOPT	First order magnetic phase transition materials
ΔT_{ad}	Adiabatic temperature change
S	Entropy
C	Heat capacity
ΔS_M	Magnetic entropy change
ΔS_{iso}	Isothermal entropy change
S_L	Lattice entropy
S_E	Electronic entropy
T	Absolute temperature
H	Magnetic field strength
B	Magnetic flux density
M	Magnetization
μ_0	Magnetic permeability of free space
μ_B	Bohr magneton
Oe	Oersted
Mn	Manganese
Si	Silicon
λ	Wavelength
FWHM	Full width at half maximum parameter
R_p	Profile R-factor
R_{wp}	Weighted profile R-factor
CCIM	Cold crucible induction melting
PPMS	Physical properties measurement system
VSM	Vibrating sample magnetometer
χ_{mol}	Molar magnetic susceptibility

1 Introduction

1.1 Motivation

Recently, the magnetocaloric materials (MCM) are gaining more attention due to their promising magnetocaloric effect (MCE) in which the magnetic entropy of the material is changed when it is exposed to a magnetic field. The potential of MCE is the base of magnetic refrigeration which is considered as an efficient and environmentally friendly cooling and temperature control system [17].

Mn_5Si_3 has received special attention with respect to its magnetic properties. At room temperature (300 K) the compound is found to be in a paramagnetic state and crystallizes in a hexagonal structure type $D8_8$ with space group ($P6_3/mcm$) [18]. During cooling, the compound behaves unusually concerning the structural and magnetic transformations [19]. It shows two first-order transitions to two antiferromagnetic phases AFM1 and AFM2 [20], at 66 K and 99 K respectively. Moreover, the first magnetic transition at 99 K is associated with a structural phase transition at which the symmetry of the crystal structure is changed from hexagonal with unit cell parameters, $a_h = 6.910 \text{ \AA}$, $c_h = 4.814 \text{ \AA}$, $Z = 2$ [21], to face centered orthorhombic symmetry with space group C_{cmm} , and lattice parameters $a_o = 6.89856(1)$, $b_o = 11.9120(2)$, $c_o = 4.79330(1) \text{ \AA}$, $Z = 4$ [22]. Another intermediate magnetic configuration AFM1' occurs if a magnetic field is applied, through which the compound transforms from the AFM1 phase to the AFM2 state. The magnetic structure of Mn_5Si_3 at low temperatures is somehow complicated and unusual.

This compound exhibits a less common type of MCE which is named inverse MCE, where the material cooled down when exposed to a magnetic field in the context of adiabatic process ($\Delta T_{ad} < 0$), while $\Delta S_M > 0$ or in other words, the magnetic entropy is increased while the material is exposed to an external magnetic field [17].

Concerning Mn_5Si_3 , the inverse MCE is associated with the phase transition between the two antiferromagnetic phases where the spin arrangement changes from collinear to non-collinear magnetic order [23]. Moreover, topological anomalous Hall effect was observed in the non-collinear AFM phase, which can potentially be used to develop new storage or computational devices [13, 24, 25].

In this thesis, the macroscopic magnetic properties of Mn_5Si_3 compound in the form of single crystal were investigated by direction dependent magnetization measurements, and the MCE has been characterized as well.

On the other hand, I will present mass magnetization measurements on $(Mn_5Ge_3)_x(MnFe_4Si_3)_{1-x}$ for a value of $(x = 0.8)$. The quasi-binary system $(Mn_5Ge_3)_x(MnFe_4Si_3)_{1-x}$, was already investigated with x-ray powder diffraction and macroscopic magnetic properties in the course of a previous master thesis of K. Al-Namourah [9]. According to the observations described there, for $(Mn_{4.2}Ge_{2.4}Fe_{0.8}Si_{1.6})$ in which $(x = 0.8)$ the saturation magnetization value was doubled compared to other samples of the series $(x = 0.6, 0.4, 0.2)$. This observation was surprising and – if true – would potentially have been of importance for an application of the material. Therefore, there was a strong reason to reproduce the measurements for this sample.

2 Theory

2.1 The magnetocaloric effect (MCE)

2.1.1 History and definition

The MCE is considered to be a magnetic thermodynamic phenomenon in which the magnetic entropy is changed in an isothermal process, or the temperature of the material is changed in an adiabatic process, when it is exposed to a magnetic field [14].

The German physicist Warburg had noticed the MCE 140 years ago [26], followed by Weiss [27]. The basic principle of the MCE was introduced by P. Debye in 1926 and W. Giaque in 1927 [28]. The MCE is the basis of magnetocaloric refrigeration technology, which depends on magnetocaloric materials exhibiting an MCE ideally near to room temperature. The first highly efficient environmentally friendly magnetic refrigerator was built in 1933 and was based on the adiabatic demagnetization of paramagnetic salts adiabatically to reach a very low temperature ($< 0.5\text{ K}$) [29]. A series of different designs and research investigation on this promising technology have followed over the years [17].

For a simple ferromagnetic material near its Curie temperature (T_c), randomly oriented magnetic moments are aligned in an ordered way when the magnetic field is activated. This leads to a decrease in the magnetic entropy while increasing the lattice entropy and heating up the material. If the magnetic field is removed, then the magnetic moments return to be randomly oriented. This increases the magnetic entropy and to compensate the material cools down [30] (Fig.2.1).

The applicable magnetocaloric materials (MCM) can be classified into second order magnetic phase transition materials (SOPT) and first order magnetic phase transition materials (FOPT). The classification depends on the type of transition the material undergoes between the ferromagnetic and paramagnetic state. For SOPT materials, the magnetization changes continuously with changing the temperature, while for FOPT materials, the change in magnetization is discontinuous as a function of temperature. The rare earth metal Gd is a prototype of a material that undergoes

SOPT [31], with low thermal and magnetic hysteresis. $Gd_5Si_2Ge_2$ [32] on the other hand, is a typical FOPT magnetocaloric material with a giant MCE, as the magnetic transition is associated with a structural phase transition. One of the drawbacks of FOPT materials is the high thermal and magnetic hysteresis compared to SOPT materials.

Most of the research these days focus on the application of MCM that can be utilized e.g., in highly efficient magnetic refrigerator, and hence the research is strongly related to devices engineering and materials science. However, a lot still remains unknown about the mechanism of the MCE and its worthwhile to perform research in this direction to enrich our knowledge about the phase transitions and thermomagnetic characteristics of the materials. Hence, there are many compounds where the observed magnetocaloric properties are not appropriate for potential refrigerants, but still the investigation of the MCE in them is a suitable tool to determine and understand the underlying principles of the MCE [33].

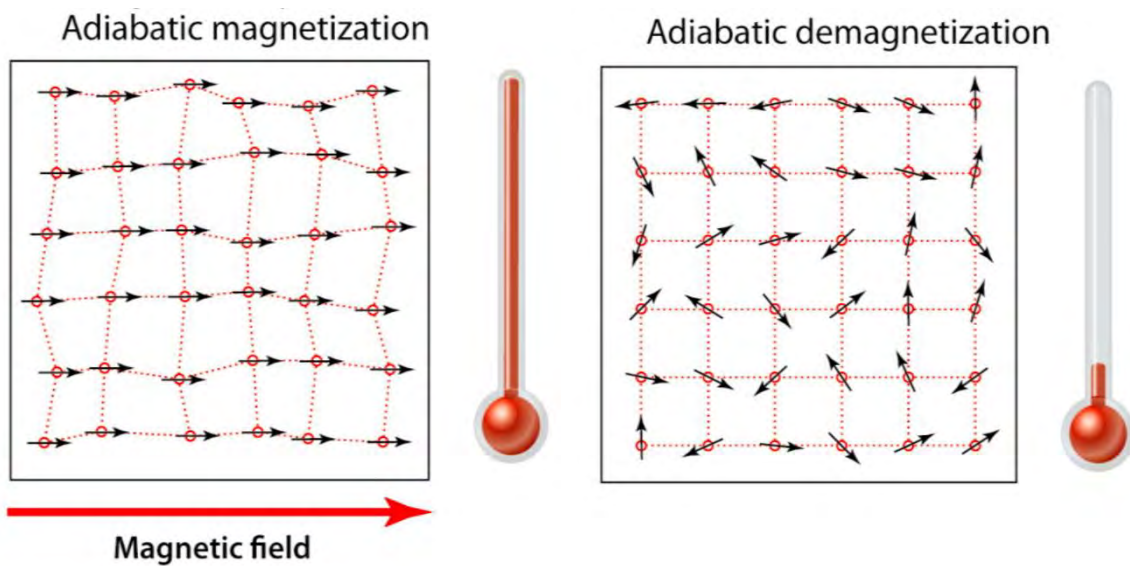


Fig.2.1 (left) The adiabatic magnetization, (right) The adiabatic demagnetization [10].

2.2 Thermodynamics of the MCE

There are two main quantities that characterize the MCE of a material: the change in temperature in an adiabatic process ΔT_{ad} , and the change in magnetic entropy in an isothermal process ΔS_M .

If the pressure is constant, the total entropy (S) of a material is a function of temperature (T) and the applied magnetic field (H). The overall entropy of the MCM is the sum of three contributions: the lattice entropy as a function of temperature $S_L(T)$ the magnetic entropy as a function of T and H $S_M(T, H)$, and the electronic entropy as a function of T $S_E(T)$.

$$S(T, H) = S_M(T, H) + S_L(T) + S_E(T) \quad (1)$$

As for the lattice and electronic entropy S_L, S_E , respectively, they are functions of the absolute temperature (T) and independent of the magnetic field (H), while the magnetic entropy $S_M(T, H)$ is highly dependent on (H). The MCE of all magnetocaloric materials result from the coupling of the magnetic field effect with the magnetic sub-lattice.

Fig.2.2 illustrates the two parameters that can represent the MCE of a ferromagnetic material, ΔT_{ad} and ΔS_M where the x-axis represents the temperature of the material, while the y-axis represents the total entropy of the material. Around T_C the material shows its maximum MCE [34].

The dashed lines represent the magnetic entropy S_M when the magnetic field is zero ($H_0 = 0$) and when it is at any value larger than zero ($H_1 > 0.0$), the third dashed line represents the sum of ($S_L + S_E$), while the solid lines show the total entropy (S) when the magnetic fields are H_0, H_1 , respectively.

If a magnetic field is applied (H_1) adiabatically (reversible adiabatic magnetization), then the magnetic entropy S_M is decreased while the overall entropy is constant and the solid is heated up [30]. In other words, to maintain $S(T_0, H_0) = S(T_1, H_1)$ the lattice entropy is increased. Under this adiabatic process, the MCE of the material is represented by the change in adiabatic temperature as $\Delta T_{ad} = T_1 - T_0$.

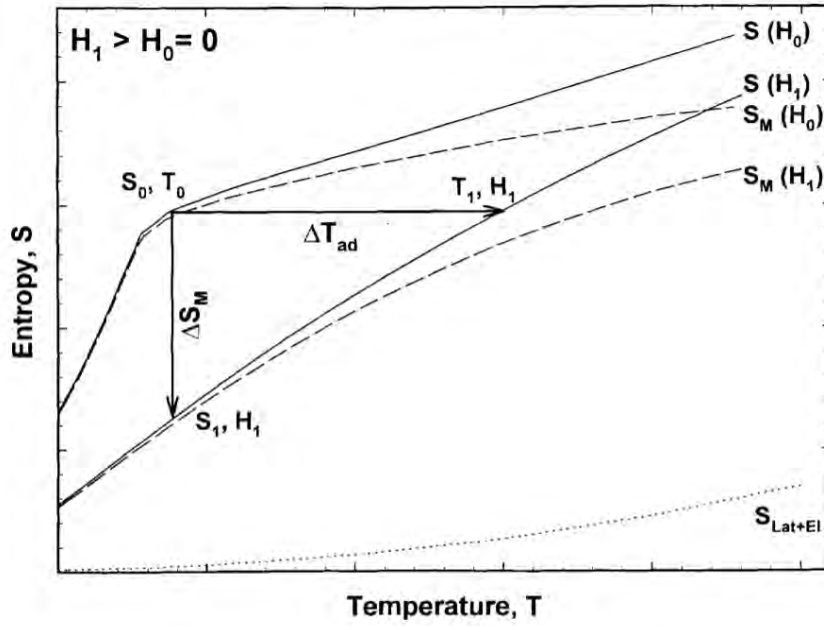


Fig.2.2 S-T diagram of MCE [7].

If the magnetic field is applied under isothermal conditions (at constant temperature (T_0)), the magnetic entropy is decreased, as a consequence the total entropy is decreased too. The MCE is given by the change in magnetic entropy:

$$\Delta S_M = S(T_0, H_0) - S(T_0, H_1) \quad (2)$$

Depending on Maxwell's relation [35], ΔS_M and ΔT_{ad} could be calculated:

$$\left(\frac{\partial S(T, H)}{\partial H} \right)_T = \left(\frac{\partial M(T, H)}{\partial T} \right)_H \quad (3)$$

where, H: magnetic field, T: temperature, M: magnetization, S: entropy.

By integrating both sides of Eq. 2 and regarding the isothermal process at constant pressure, it follows:

$$\Delta S_M(T, \Delta H) = \int_{H_1}^{H_2} \left(\frac{\partial M(T, H)}{\partial T} \right)_H dH \quad (4)$$

The previous equation states clearly that the greater the $\left(\frac{\partial M(T, H)}{\partial T} \right)_H$ the greater the MCE. The peak of MCE occurs around the phase transition temperature.

In adiabatic process, the infinitesimal adiabatic temperature rise is obtained from combining equation (2) and ($dQ = CdT = -Tds$), Q is the heat flux and C is the heat capacity. Which gives:

$$dT = - \left(\frac{T}{C(T, H)} \right)_H \left(\frac{\partial M(T, H)}{\partial T} \right)_H dH \quad (5)$$

By integrating Eq.4, it will give a quantitative value for ΔT_{ad} :

$$\Delta T_{ad}(T, \Delta H) = - \int_{H1}^{H2} \left(\frac{T}{C(T, H)} \right)_H \left(\frac{\partial M(T, H)}{\partial T} \right)_H dH \quad (6)$$

where, $C(T, H)$ is the heat capacity of the MCM.

It becomes clear from the previous equation that the MCE can be improved by a wide field variation, and/or by choosing MCM with small heat capacity, and/or greater $\left(\frac{\partial M(T, H)}{\partial T} \right)_H$.

The question now is: how to calculate the ΔT_{ad} and /or ΔS_M practically? In the context of next sections, a brief description about the determination of MCE will be provided.

2.3 Inverse MCE

It is clear that there is a strong relationship between the entropy of the system which is associated with structural and magnetic changes and the size of MCE. According to what has been mentioned previously, there are two main quantities that characterize the MCE of a material: the change in temperature in an adiabatic process ΔT_{ad} , and the change in magnetic entropy in an isothermal process ΔS_M . In regular MCE materials, the sample heats up when exposed to a magnetic field adiabatically, which means that $\Delta T_{ad} > 0$, while during the isothermal process, the instantaneous change of magnetization with respect to instantaneous change of temperature is negative $\Delta S_M < 0$. Effects obeying these characteristics are named traditional or direct MCE [1]. The opposite case, that is the temperature derivative of the magnetization is positive, and the sample cooled down when exposed to a magnetic field in the context of adiabatic process ($\Delta T_{ad} < 0$), while $\Delta S_M > 0$ or in other words, the magnetic entropy is increased while the material is exposed to an external magnetic field, this is the inverse MCE [17].

Although the inverse MCE is more rarely investigated than the direct one, it is found in many magnetic systems, in particular when antiferromagnetic order is involved.

Examples include: the magnetic transition from anti-ferromagnetic to a ferrimagnetic phase (AFM/FIM) like in $Mn_{1.82}V_{0.18}Sb$ [36], or the transition from collinear anti-ferromagnetic to non-collinear anti-ferromagnetic phase like in Mn_5Si_3 [14], or the anti-ferromagnetic to ferromagnetic phase (AFM/FM) as observed in $Fe_{0.49}Rh_{0.51}$ [37].

According to earlier investigations, the inverse MCE can be explained by the fact that the application of an external magnetic field induces spin fluctuations, which leads to an increase of the magnetic entropy [14, 38].

2.4 Determination of MCE

There are two different methods to measure the magnetocaloric effect: the direct measurements and the indirect ones. The direct method requires measurement of the samples temperature while applying and removing a magnetic field in an adiabatic process. On the other hand, the indirect method is based on the measurement of magnetization as a function of magnetic field and temperature.

2.4.1 Direct determination of MCE

The MCE could be obtained directly by measuring T_0 at H_0 and T_1 at H_1 under adiabatic conditions with an error ratio 5-10% which depends on the quality of the thermal insulation of the sample, the accuracy of the thermometer and the strategy that is followed to prevent the thermal sensor readings from being affected by the changes in magnetic field [7].

The adiabatic process is fulfilled if it is assured that no heat is exchanged, in practice this can be achieved by rapid changes of the magnetic field. So, if e.g. the material is moving at a specific speed through a fixed magnetic field or the magnetic field is moved at a certain speed while the material remains fixed, then we will ensure that the adiabatic conditions are met [30, 39].

2.4.2 Indirect determination of MCE

The indirect measurements of the MCE could be achieved by two methods, one is the calorimetric method which relies on the heat capacity of the material to calculate both $\Delta S_M(T, \Delta H)$ and $\Delta T_{ad}(T, \Delta H)$, the other one is the magnetization method which calculates ΔS_M as function of temperature and magnetic field.

$\Delta S_M(T, \Delta H)$ is the most commonly used parameter to characterize the MCE [40]. It can be calculated from the isothermal magnetization curves or isofield magnetization curves. Numerically, integrating Eq.3 will produce a quantitative value of ΔS_M [41].

The error ratio of ΔS_M which is obtained from the magnetization measurements is 3-10%, where the accuracy of the result depends on temperature, magnetic moment and field measurements.

It should be pointed out that, regardless of the methods that are used to characterize the MCE, the results should not be completely divergent or equal, but rather convincingly close. Both quantities of $|\Delta T_{ad}|$ and $|\Delta S_m|$ depend on (T_0) and the difference between the initial and the final field $(H_1 - H_0)$.

Experimentally, it is easier and faster to sweep the magnetic field continuously (stabilizing H at different values) than sweeping the temperature of the material at a ramp rate (stabilizing T at different values), in particular if one takes into account the time needed for a measurement [42].

In this thesis, indirect measurements were performed to characterize the MCE of Mn_5Si_3 in the form of single crystal. $\Delta S_M(T, \Delta H)$ was calculated via isothermal magnetization curves and/or isofield measurements.

2.5 Scattering basics and diffraction techniques

Scattering techniques are used to obtain detailed information about the crystal structure of a material at the microscopic level. In particular, X-ray diffraction is an analytical non-destructive elastic scattering method used to get structural information

of the materials [43]. If one compares the wave length of the X-rays with the inter-atomic distances in the crystals, they are approximately similar ($\sim .15 - .4 \text{ nm}$). This means that X-rays are a very appropriate choice to perform diffraction experiments on crystalline materials [44].

In crystals, when electromagnetic radiation hits parallel lattice planes spaced apart by an interplanar distance d , the incoming wave will be scattered. if the difference between the path lengths of the diffracted beams from a neighboring lattice planes is an integer multiple of the incident wavelength, the scattered waves are in phase. This condition was defined by Lawrence Bragg, and it is described by Bragg's equation [43]. Bragg's law [6] describes the conditions at which constructive interference between the scattered waves occurs, (see **Fig.2.3**) , that is:

$$n\lambda = 2d \sin \theta \quad (7)$$

where n : is the order of diffraction (a positive integer), λ : the wavelength, d : the distance between two parallel lattice planes (d_{hkl}), θ : the glancing diffraction angle.

The previous relationship is the basis for a diffraction experiment where the diffracted intensity is recorded as a function of the diffraction angle.

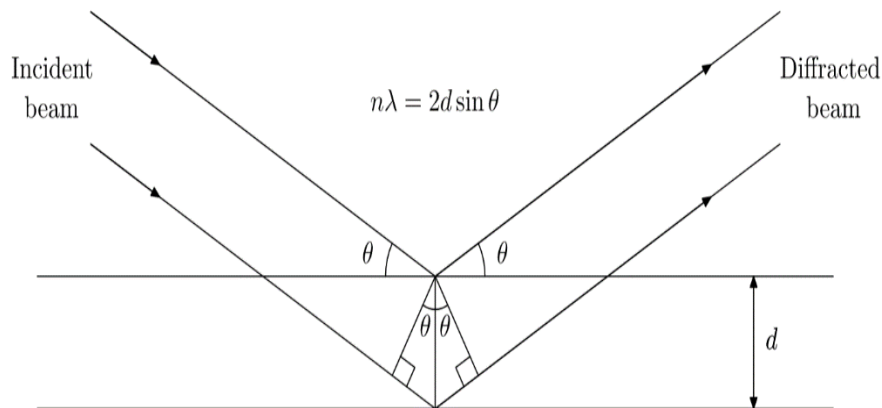


Fig.2.3 Bragg's Law is represented as schematic illustration, taken from Ref. [6].

In this thesis Laue diffraction was used to define the correct crystallographic orientation of the single crystals of Mn_5Si_3 for the magnetization measurements and

X-ray powder diffraction was used to check the phase purity of the polycrystalline material of $Mn_{4.2}Ge_{2.4}Fe_{.8}Si_{.6}$. The basic concepts of the two diffraction methods will be explained in the next section.

2.5.1 X-ray powder diffraction

x-ray powder diffraction is a non-destructive technique which uses X-ray radiation on polycrystalline samples to characterize the structure of the material. It is also used in quantitative phase analysis or for tracking of phase transitions under the influence of temperature, pressure, and magnetic or electrical fields [6]. Powder samples can be considered as ideal if a large number of crystallites exists where all possible orientations of a crystal lattice exist in equal proportions.

In an X-ray powder diffraction experiment, a beam of monochromatic X-ray radiation hits the powder sample. As the crystal lattice in the powder has all possible orientations, one will observe all the possible diffraction peaks from lattice planes for which the Bragg condition is fulfilled. Peaks with identical Bragg angles form cones which are called Debye-Scherrer cones. Every Debye-Scherrer cone is related to a single set of lattice planes. In a flat plate detector, these cones will be projected as a 2-D image of smooth concentric rings. Usually, the diffraction patterns are presented by a diffractogram in which the intensity (I) is represented as a function of the scattering angles (2θ) (Fig.2.4) [44].

2.5.2 Laue single crystal diffraction

In this work, Laue diffraction was employed to define the crystal orientation of a single crystal of Mn_5Si_3 . For the Laue method a polychromatic beam is used. In other words, multiple wavelengths are used to irradiate the fixed single crystal sample. This means that the incident angle θ and the incoming beam have a specific orientation with respect to individual lattice planes (hkl). If Bragg's law is satisfied for a particular

lattice plane and a specific wavelength, constructive interference occurs. In this case the detector will record a diffraction spot [45].

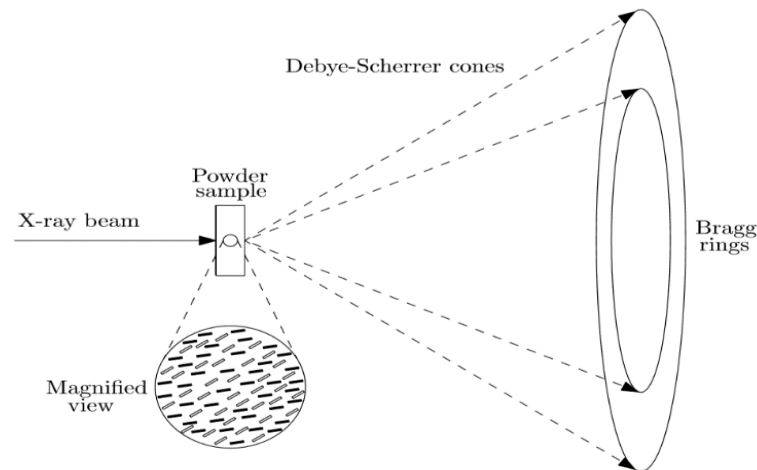


Fig.2.4 Schematic drawing of Debye-Scherrer cones, taken from Ref. [6]

2.5.3 The Le Bail method

The Le Bail method is a technique used to fit the measured powder diffraction pattern to a calculated one which follows from an assumed model. With this method the unit cell parameters of the crystal structure can be determined, and an initial idea about the space group of the crystal structure can be obtained. For this, an algorithm which depends on an iterative least squares analysis is used [46]. In addition to refining the unit cell parameters, many other parameters could be refined e.g., the background, the profile function, and the zero-shift parameter.

As an initial step in this method, approximate values of unit cell parameters and an initial space group of the crystal structure are provided. Using this primary input, the diffraction patterns diagram is calculated and then compared to the measured one. Then one starts adjusting the mentioned parameters (unit cell parameters, background parameters, profile function and zero shift parameter) to reduce the difference between the measured and calculated diagrams. In the next step, a new diffraction

diagram is calculated and the processes of comparing, adjusting and calculating another new diffraction diagram is repeated, until a satisfactory agreement between the measured and the calculated diagrams is reached. Numerical criteria are used to quantify the agreement. These are: the profile R-factor (R_p) and the weighted profile R-factor (R_{wp}),

$$R_p = \frac{\sum_j |y_{obs,j} - y_{cal,j}|}{\sum_j y_{obs,j}} \quad (8)$$

where, $y_{obs,j}$: observed intensity at a specific diffraction profile point, $y_{cal,j}$: calculated intensity at a specific diffraction profile point.

$$R_{wp} = \sqrt{\frac{\sum_j w_j (y_{obs,j} - y_{cal,j})^2}{\sum_j w_j y_{obs,j}^2}} \quad (9)$$

where, w_j : weighting factor = $1/y_{obs}$.

R_{wp} is a well-known indicator that expresses the quality of the refinement. In practice many programs are available which use the Le Bail technique like e.g. BGMN [47], ARITVE [48], FullProf [49], Jana2006. In this thesis Jana2006 [50] is used.

3 The magnetocaloric materials of this work

3.1 Introduction

The Pseudo binary system $Mn_{5-x}Fe_xSi_3$ with ($x = 0,1,2,3,4,5$) has MCE at different temperatures depending on the different values of (x). The parent structure of all compounds in the system crystallizes in a hexagonal structure with space group ($P6_3/mcm$) [51]. Mn and Fe ions occupies two different crystallographic sites, 6(g) and 4(d) respectively, the occupation ratio depends on the compositional (x) parameter [52].

The magnetocaloric properties and the magnetic transitions in this system was investigated by [16], using magnetization measurements as a function of magnetic field and temperature. At low temperatures the Mn-rich compounds ($x = 0,1,2$) shows two different antiferromagnetic phases (AFM1, AFM2). It was found that, the temperature of antiferromagnetic ordering shifts to higher temperature, as the parameter (x) is increasing, in another word, as increasing the ratio of Fe. For Fe-rich compounds ($x = 4,5$) ferromagnetic order was observed (**Fig.3.1, (left)**).

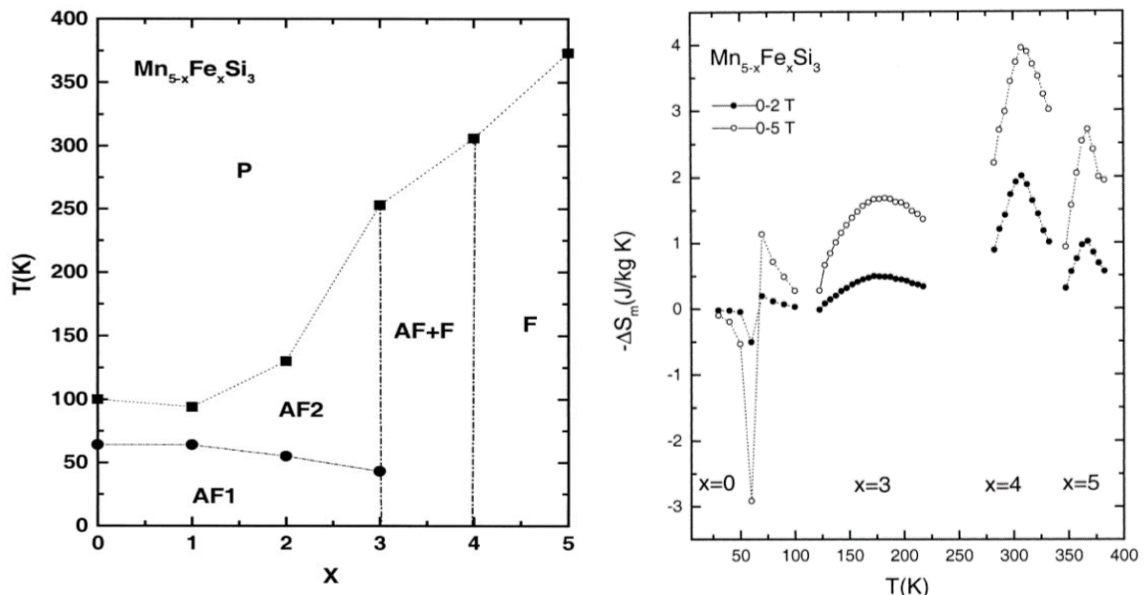


Fig.3.1 (left) Sketch of a magnetic phase diagram of the system $Mn_{5-x}Fe_xSi_3$ ($x = 0, 1, 2, 3, 4, 5$), (right) The magnetic entropy change for a field change of 2T and 5T. Figure taken from [16].

The compound $MnFe_4Si_3$ ($x = 4$) crystallizes in space group $P-6$ with lattice parameters $a = 6.8054(7) \text{ \AA}$ and $c = 4.7290(5) \text{ \AA}$ [53]. It shows the largest magnetocaloric effect compared to the other compounds in this system (**Fig.3.1, (right)**) at a transition temperature around room temperature ($T_c = 300K$) where it changes from a paramagnetic to a ferromagnetic phase. The closely related compound Mn_5Ge_3 , which crystallizes in the same structure type (space group $P6_3/mcm$, and cell's dimensions $a = 7.184(2)\text{ \AA}$, $c = 5.053(2)\text{ \AA}$) [54], also shows a ferromagnetic transition at a similar temperature ($T_c = 304K$). Around (T_c), this compound shows a second order transition phase with considerably larger MCE, as the magnetic entropy change is about (3.8) and (9.3) $J/kg.K$ at field change of 2.0 and 5.0 T respectively [23]. In addition to a rapid change in magnetization [23]. This compound would therefore be more suitable for applications than $MnFe_4Si_3$, yet there is a limitation which decreases the usage of this compound on a large scale, due to the high content of the rather expensive element Ge.

As both compounds crystallize in the same structure type and show MCEs at similar temperatures, it is interesting to look at the properties of the quasi-binary solid solution of $MnFe_4Si_3$ and Mn_5Ge_3 . This quasi-binary system $(Mn_5Ge_3)_x(MnFe_4Si_3)_{1-x}$, contains mainly (Mn, Fe, Si) which are abundant, non-toxic, and non-expensive elements. The potential of the magnetocaloric effect was already investigated with x-ray powder diffraction and macroscopic magnetic properties in the course of a previous master thesis of K. Al-Namourah [9]. In this thesis, I will present the repetition of mass magnetization measurements of $(Mn_5Ge_3)_x(MnFe_4Si_3)_{1-x}$ for a value of ($x = 0.8$), the motivation for this repeating this investigation will be discussed later on.

Going back to the system $Mn_{5-x}Fe_xSi_3$, there is another remarkable compound which is one of the end members, Mn_5Si_3 ($x = 0$). This compound exhibits two well-known antiferromagnetic phase transitions and inverse MCE at low temperature. More deep details about this intermetallic compound will be provided in the next section.

In short, in this thesis I worked on two different compounds which are: Mn_5Si_3 single crystal compound and a polycrystalline sample of $Mn_{4.2}Ge_{2.4}Fe_{0.8}Si_{1.6}$. The DC-field mass magnetization measurements with different protocols were performed on both of them to investigate the macroscopic magnetic properties and to calculate the potential of the MCE.

3.2 The intermetallic compound Mn_5Si_3

3.2.1 Crystal structure of Mn_5Si_3

At room temperature (300 K) the compound is found to be in paramagnetic state and crystallizes in a hexagonal structure type $D8_8$ with space group ($P6_3/mcm$) [18], with unit cell parameters, $a_h = 6.910 \text{ \AA}$, $c_h = 4.814 \text{ \AA}$, $Z = 2$ [55]. The atomic positions of this structure were first determined by Aronsson in 1960 [21] and later confirmed by Lander and Brown in 1967 [22]. **Table (3.1)** contains more detailed crystallographic data on the compound.

Table (3.1) Crystallographic data of Mn_5Si_3 [22].

Space group: $P6_3/mcm$, $Z = 2$		
At 300 K, unit cell parameters: $a_h = 6.910 \text{ \AA}$, $c_h = 4.814 \text{ \AA}$		
	Atomic positions	site symmetry
(4) Mn1 in 4(d)	$\pm(\frac{1}{3}, \frac{2}{3}, 0); (\frac{2}{3}, \frac{1}{3}, \frac{1}{2})$	32
(6) (Mn2 in 6(g)	$\pm(x, 0, \frac{1}{4}); (0, x, \frac{1}{4}); (-x, -x, \frac{1}{4})$ $x = .2360(1)$	mm
(6) Si in 6(g)	$\pm(x, 0, \frac{1}{4}); (0, x, \frac{1}{4}); (-x, -x, \frac{1}{4})$ $x = .5991(2)$	mm

Fig.3.2 shows the projection of the crystal structure of Mn_5Si_3 along [001] that was proposed by [56]. The hexagonal unit cell is displayed and the different atomic positions of Mn1, Mn2 and Si atoms are shown. Manganese ions occupy two different crystallographic sites, namely 4(d) which is occupied by Mn1 ions and 6(g) that is occupied by Mn2 ions [55].

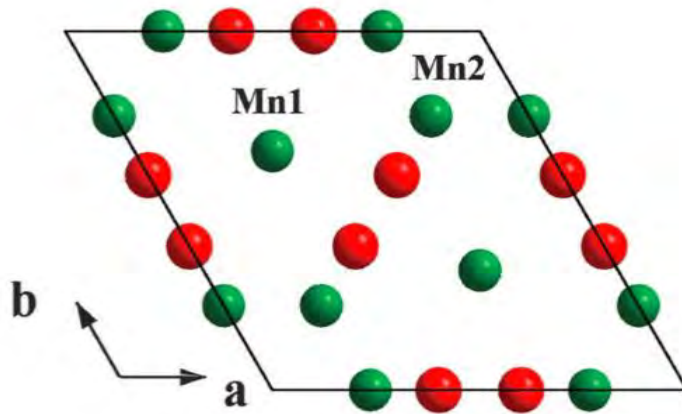


Fig.3.2 Mn_5Si_3 hexagonal unit cell projected along [001], green spheres represent Mn ions, red ones represent Si ions, taken from [1].

The low temperature (4.2 K) structure of Mn_5Si_3 was first studied by [22] before more than 50 years ago. At low temperatures, the compound undergoes a structural phase transition at which the crystal structure is changed to orthorhombic unit cell with lattice parameters $a_o = 6.89856(1), b_o = 11.9120(2), c_o = 4.79330(1)\text{\AA}$. The lattice parameters of orthorhombic unit cell could be represented with respect to those of the hexagonal unit cell as $a_h \approx a_o, c_h \approx c_o$ and $\sqrt{3}a_h \approx b_o$, Fig.3.3 shows the projection of the structures along [001] and illustrates the relation between the hexagonal unit cell and the orthorhombic one.

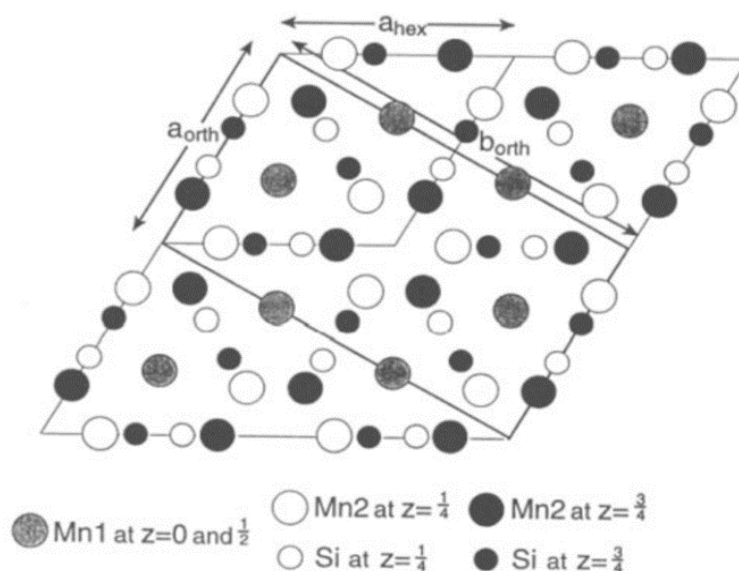


Fig.3.3 Projection of the crystal structure of Mn_5Si_3 along [001]. The hexagonal unit cell and orthorhombic unit cell are presented with bold lines. The figure taken from [15].

3.2.2 Magnetic structures of Mn_5Si_3

During cooling, the compound Mn_5Si_3 behaves in an unusual way and exhibits structural and magnetic transformations [19, 20]. When the compound is cooled down to Néel temperature $T_{N2} \approx 99\text{ K}$, a magnetic transition from the paramagnetic phase (PM) to a collinear antiferromagnetic phase (AFM) is observed. This magnetic phase is known as AFM2 [1, 11, 15, 22, 57, 58]. As cooling continues down to $T_{N1} \approx 66\text{ K}$ another transition takes place from the AFM2 to a non-collinear antiferromagnetic phase which is known as AFM1 [20].

The first magnetic transition at T_{N2} is associated with above-described change in the crystal structure, where the symmetry is reduced to a face centered orthorhombic phase with space group C_{mmm} and $Z = 4$.

In the AFM2 phase, only two third of the Mn2 ions have an ordered magnetic moment of $\mu = 1.5\mu_B$. Spins are arranged in a collinear style and aligned parallel and antiparallel with respect to the b-axis of the orthorhombic unit cell (see **Fig.3.4 (1)**). The Mn1 ions and the remaining one third of Mn2 show no ordered magnetic moments. This implies that, the Mn2 ions are not symmetry equivalent any more but split into two independent sets [1, 15, 56]. Mn21 atoms occupying Wyckoff positions 4(c) with site symmetry (mm) and Mn22 atoms on Wyckoff positions 8(g) with site symmetry (m). As illustrated before, only Mn22 atoms exhibits an ordered magnetic moment.

In the AFM1 phase, the magnetic moments re-oriented to different directions in a highly non-collinear fashion. One third of Mn2 atoms still does not show an ordered magnetic moment, yet in contrast to this the atoms on the Mn1 do develop an ordered moment. This fact has been related to the expansion of the crystallographic c axis at the AFM2-AFM1 transition which leads to an increased distance between the Mn1 atoms [56]. This increased distance is above the critical distance for magnetic ordering on the Mn-ions (**Fig.3.4 (2)**).

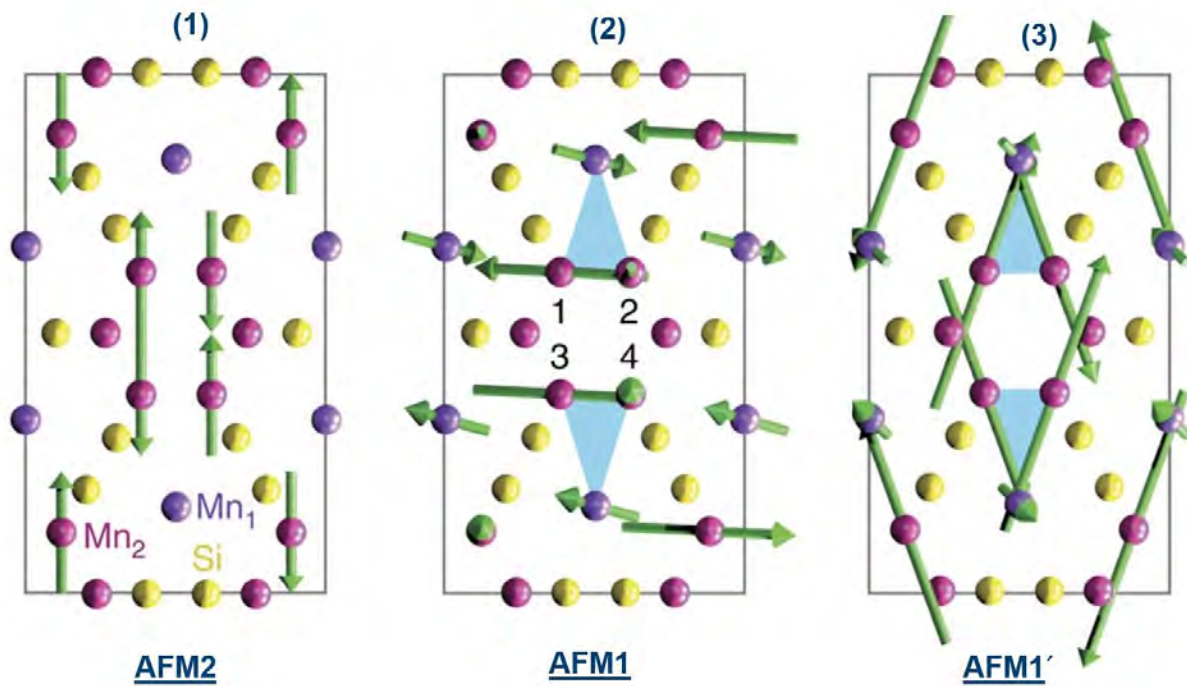


Fig.3.4 The magnetic structure of Mn_5Si_3 . (1) The collinear AFM2 Phase. (2) The non-collinear AFM1 phase. (3) The non-collinear AFM1' phase [12]. (View along the c-direction)

Below 66 K (AFM1), the symmetry of the crystal structure is still orthorhombic, yet the atoms occupying the Mn22 sites are magnetically different. They split into two parts, Mn23 and Mn24. In reference [56], the AFM1 was investigated at 4.2 K with single-crystal neutron diffraction and zero-field neutron polarimetry, and it was shown that atoms of Mn1 exhibit ordered moments of $\mu = 1.20(5) \mu_B$ oriented parallel and anti-parallel to the direction with polar coordinates $\varphi = 105(1)^\circ$, $\theta = 116(1)^\circ$, where φ is measured from [010] and θ from [001] axis. Still Mn21 exhibits no ordered magnetic moment, but Mn23 exhibit magnetic moment of $\mu = 2.30(9) \mu_B$ with polar coordinates $\varphi = 93(1)^\circ$, $\theta = 70(1)^\circ$, while Mn24 atoms exhibit a different value of magnetic moment of $1.85(9) \mu_B$ oriented to the directions with polar coordination of $\varphi = 11(7)^\circ$ and $\theta = 21(1)^\circ$.

According to all these observations, the magnetic structure of Mn_5Si_3 at low temperatures is complex and unusual, as the atoms exhibit different magnetic moments even, they have similar chemical environments.

In addition, Sürgers et al. [13] observed an intermediate magnetic configuration which occurs if a magnetic field is applied. This phase was named AFM1', and represents a

state through which the compound transforms from the AFM1 phase to the AFM2 phase. In this intermediate transition, a non-collinear phase was suggested as well, however with a different spin arrangement compared to the AFM1 phase (**Fig.3.4(3)**).

The inverse magnetocaloric effect (Inverse MCE) is an effect which coincides with the transition from the collinear AFM2 to the non-collinear AFM1. At this transition, the sign of ΔS_m changes around T_{N1} from negative to positive [16]. As mentioned before, following Maxwell's thermodynamic relationship $(\partial S/\partial B)_T = (\partial M/\partial T)_B$, cooling can be obtained if a sample that was isothermally magnetized before is adiabatically demagnetized. In the AFM1 phase, cooling can be obtained through adiabatic magnetization [17]. More details about what is known in the literature about this effect in Mn_5Si_3 will be provided in the next section.

3.2.3 Summary of macroscopic magnetization measurements on Mn_5Si_3 as described in the literature

Many experimental studies were carried out to investigate the physical characteristics and magnetic properties of Mn_5Si_3 due to the attractiveness of its unusual magnetic, structural and magneto-functional properties.

A single crystal of Mn_5Si_3 compound grown by Czochralski method was experimentally investigated in [57]. Static magnetic fields of up to 15 T was applied parallel to the hexagonal axis (H || c). Besides the two well-known first-order transitions, an additional magnetic transition associated with hysteresis was observed in the temperature range from $T \approx 30$ K to 64 K. The field-dependent magnetization curves in the mentioned temperature range showed, that this intermediate transition is highly dependent on both the magnetic field and the temperature.

In the context of Hall-effect measurements on the non-collinear AFM1 phase of Mn_5Si_3 , isothermal magnetization measurements as a function of applied magnetic field (H) along the [001] axis of the hexagonal unit cell of the compound were performed [13]. The measurements indicated the two transitions of AFM1-AFM2 and AFM2-PM at zero fields around T_{N1} and T_{N2} , respectively. In addition, another transition to an intermediate phase (AFM1') was observed which is highly dependent

on temperature and magnetic field. The magnetic phase diagram shown in **Fig.3.5** was obtained based on the Hall effect measurements, resistivity and magnetization measurements .

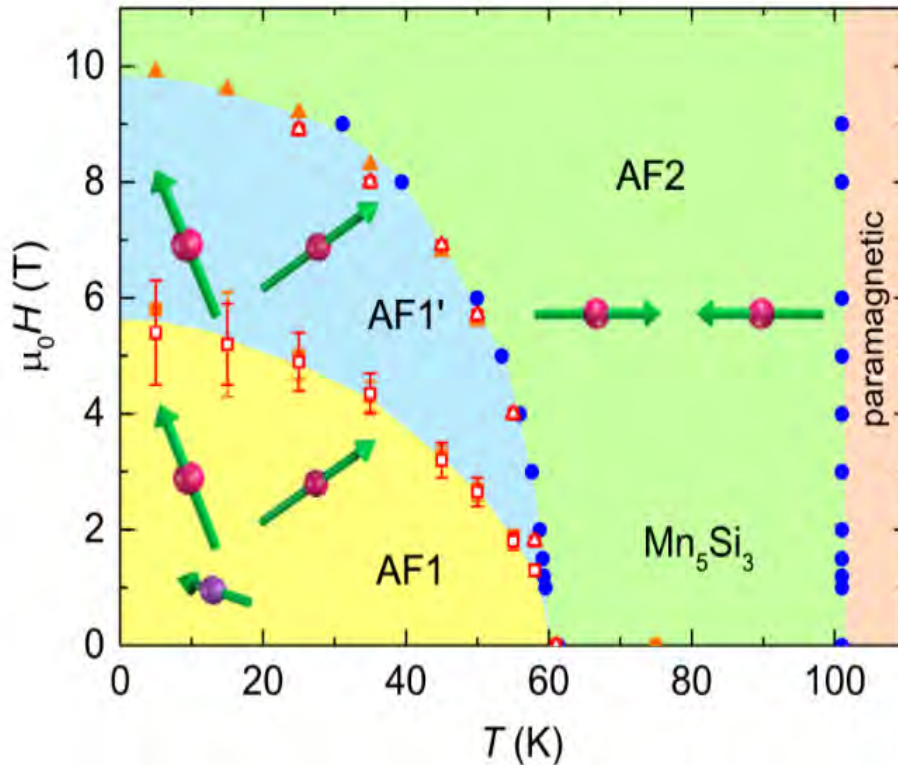


Fig.3.5 Magnetic phase diagram of Mn_5Si_3 . Open red symbols represent the data collected from Hall effect measurements, dots of blue data represent resistivity data, and orange triangles correspond to magnetization measurements. The hysteresis width corresponding to the Hall resistivity ($\rho_{yx}(H)$) is indicated by error bars. The relative non-coplanar orientations are visualized by arrows of Mn1 moments (violet) and Mn2 moments (red) in the AMF1 and AMF1' phases [13].

Another determination of the magnetic phase diagram on a Mn_5Si_3 single crystal was done by [2]. Based on magnetoresistance, magnetization and the Hall effect measurements, three phase transitions at different temperatures were observed. The observed transition temperature for the AFM2-PM was 95 K. A transition to an intermediate phase (represented in blue colour in **Fig.3.6**) at T_{N1} 65 K. Both transition temperatures hardly change as a function of magnetic fields up to 7.0 T. At $T_{N1}^* = 45 K$ the transition to the non-collinear AFM1 phase was observed. The phase transition temperature T_{N1}^* is highly dependent on magnetic field and decreases to 30 K at 7 T.

The inverse magnetocaloric effect was observed around the temperature T_{N1}^* (see Fig.3.6).

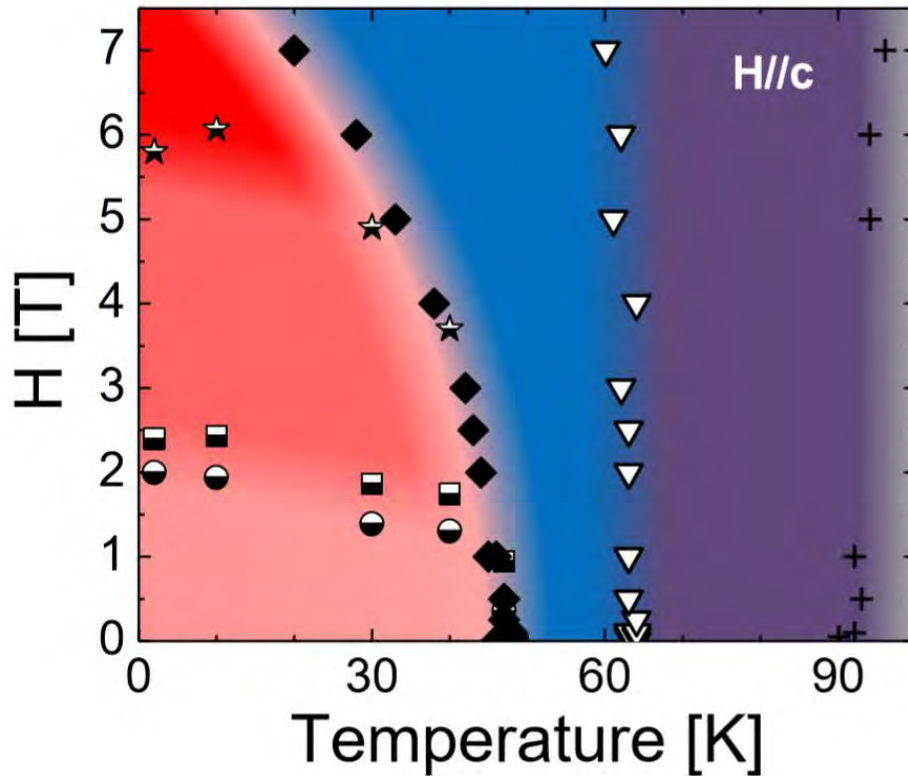


Fig.3.6 Magnetic phase diagram of Mn_5Si_3 (Temperature vs. Magnetic field), (+) symbol relates to T_{N2} , (∇) symbol represents T_{N1} , (\blacklozenge) corresponds to the third transition T_{N1}^* . Data are extracted from magnetization measurements as a function of temperature. Half-filled symbols correspond to magnetization measurements as a function of magnetic field [2].

A detailed magnetization measurement was performed on powder samples in fields up to 12 T and over a temperature range from 120 K to 2 K in [11]. The study showed that, if a magnetic field is applied at low temperatures, transition associated with hysteresis from a non-collinear AFM phase to a collinear AFM phase is observed (Fig.3.7). The corresponding critical field is highly temperature-dependent, as it decreases with increasing temperature in a quadratic relationship. The study confirmed the two transitions AFM1-AFM2 and AFM2-PM. But it also indicated the existence of another transition at much smaller fields and temperatures, This transition is associated with the kinks in the isothermal magnetization curves of 2 and 10 K (Fig.3.8).

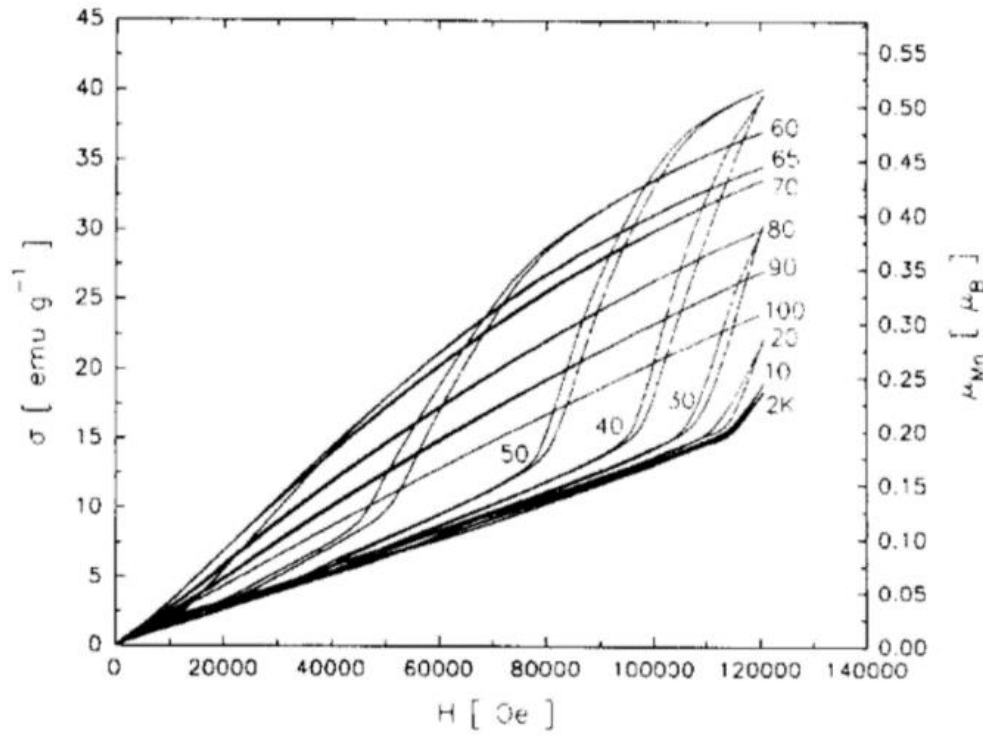


Fig.3.7 Isothermal magnetization curves of Mn_5Si_3 from (2-100) K [11].

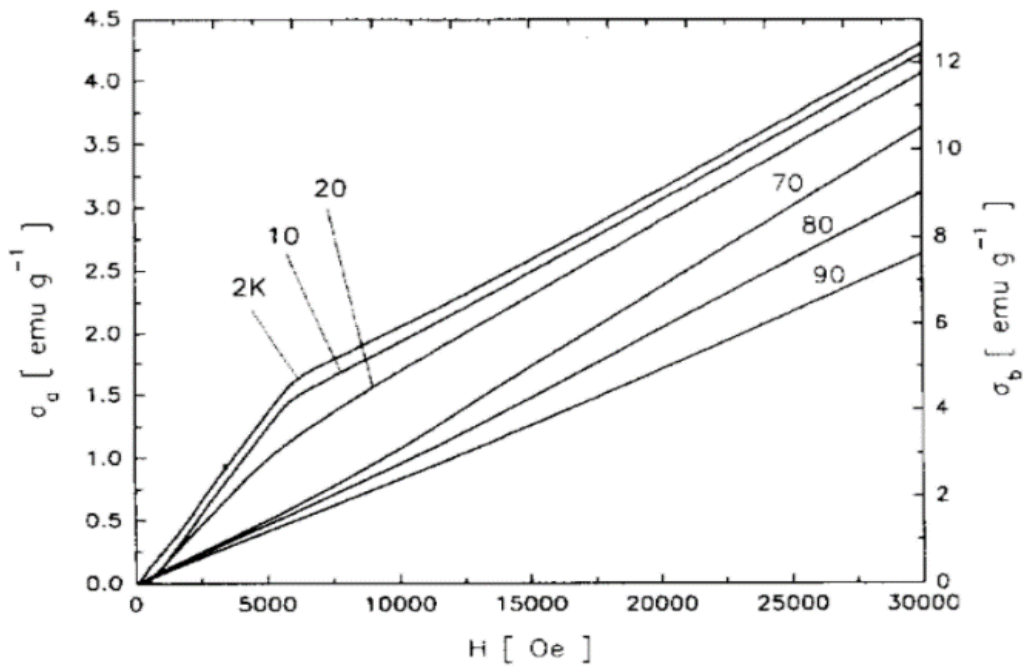


Fig.3.8 Isothermal magnetization curves. σ_a , σ_b represent the magnetization values in the non-collinear and collinear phases respectively. The knees in 2 K and 10 K indicate the third mentioned transition [11].

A detailed DC magnetic measurements on powder samples of Mn_5Si_3 was accomplished in [59]. In this study, the magnetization measurements as a function of temperature were performed in a field-cooled heating protocol (FCH) with different applied magnetic fields. It was found that the transition temperature from the PM phase to the AFM2 phase was hardly affected by changes in the strength of the magnetic field, while the transition temperature corresponding to the change from the AFM2 to the AFM1 phase was significantly shifted towards lower temperatures with increasing the magnetic field.

The reason for this shift is the existence of the third intermediate magnetic transition from the AFM1 to the AFM1' phase. This phase occurs in the intermediate regime between the AFM1 and AFM2 phase, was also reported in [13].

Several compounds in the system of $Mn_{5-x}Fe_xSi_3$ with $x = 0,1,2,3,4,5$ had been investigated in [16]. Here, the magnetization was measured as a function of magnetic field and temperature, and the magnetic phase diagram was created for the system. The inverse MCE was observed around 67 K for Mn_5Si_3 ($3 J/kg.K$ for a field change of 5.0 T).

According to [14], the temperature of the Inverse MCE in Mn_5Si_3 is around 58 K and as high as $4 J/kg.K$ for a field change of 5.0 T. In this work, the change in magnetic entropy was presented as a function for different field changes. Presumably, due to the presence of antiferromagnetic interactions, there are negative values of the magnetic entropy changes ($-\Delta S_M$) below T_{N1} due to the increase in magnetic entropy originating from disordering of the non-collinear spins on the Mn1 and Mn2 atoms. Above T_{N1} , ($-\Delta S_M$) becomes positive, while no particularly striking change of ($-\Delta S_M$) was observed around T_{N2} (**Fig.3.9**).

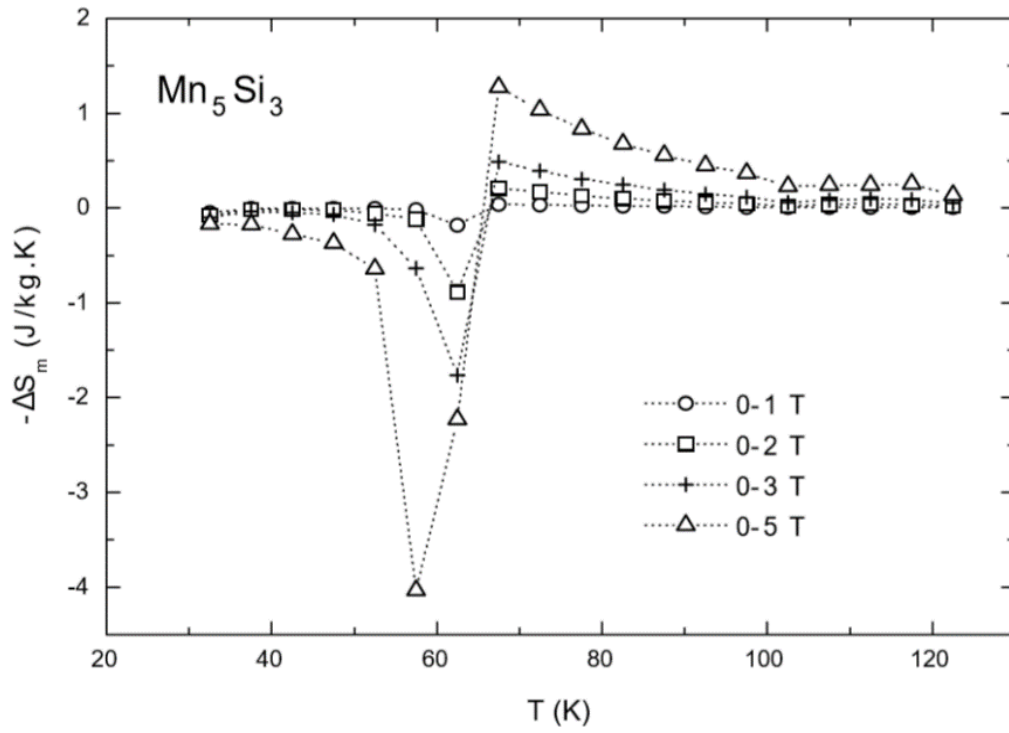


Fig.3.9 The magnetic entropy change ($-\Delta S_M$) of the Mn_5Si_3 compound [14].

4 Instrumentation

4.1 Cold crucible induction melting device

Cold crucible induction melting (CCIM) is a fast, innovative, and reliable process to provide a highly homogeneous melt, both thermally and chemically. Also, if there is a necessity for a high purity melting, CCIM is a prime option for achieving this [60].

When a high-frequency electric current (AC) passes through the coils surrounding a glass cap over a copper crucible, the generation of a high-frequency magnetic field induces eddy currents within the conductive material inside the copper crucible. The Joule heating needed to melt the sample is generated by the electrical resistance that the material creates to disperse the eddy currents. Once the sample is melted, the rotating currents contribute to stirring the mixture and ensuring homogeneity (Fig.4.1) [61].

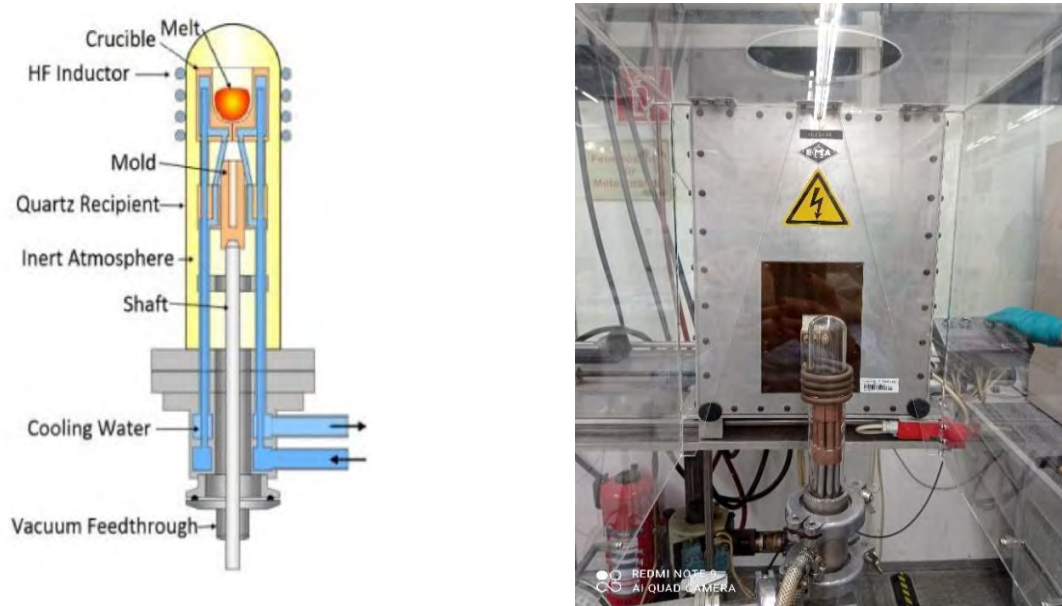


Fig.4.1 (left) Scheme of a cold crucible induction melting apparatus (Schematic view) (with permission from [3]), (right) Photo of the CCIM device at the JCNS-2.

In this system, a copper crucible in which the elements of a compound are placed in stoichiometric amounts, is formed from several vertical pieces. They are placed closed to each other yet separated carefully in such a way they are isolated, to ensure the

passage of the magnetic field produced by a powerful AC through the crucible wall. In other words, they provide electromagnetic transparency.

A water-based cooling system is attached with two cooling cycles, once for the copper induction coils and the other for the crucible. The system of CCIM is connected to an Argon source and evacuating pumps.

In this thesis, the CCIM device was used to obtain the polycrystalline material of composition $Mn_{4.2}Ge_{2.4}Fe_{.8}Si_{.6}$ by melting a highly pure stoichiometric amounts of the constituent elements.

4.2 The MWL120 real-time back-reflection Laue camera

The system of the MLW 120 Laue camera uses the back-reflection Laue method [62] to identify the crystallographic axis of single crystal grains. It is equipped with a multiwire detector and a tungsten X-ray tube.

The sketch in **Fig.4.2**, shows the main parts of the system. A tungsten X-ray tube connected to a high voltage generator emits a polychromatic X-ray beam that passes through a collimator which is positioned in the center of the detector screen. This X-ray beam hits the single crystal sample. The diffracted beams are back-scattered and collected by the detector. The collected diffraction patterns are then transferred to the connected computer which uses specific software to display the image in real-time. The user can control the movement of the crystal by a motor, and view the image on the detector screen in real-time. A water-cooling system is used to cool the X-ray tube and the generator during the operation process. In this thesis, the MWL120 Laue camera was used to define the crystallographic orientation of the measured single crystals of Mn_5Si_3 .

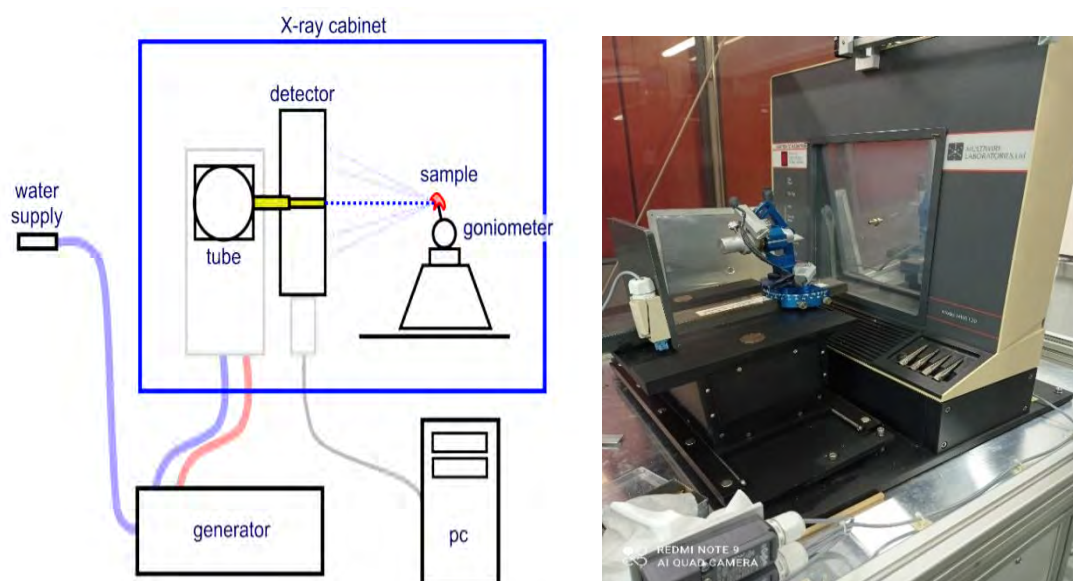


Fig.4.2 (left) A sketch of the MWL120 camera [4], (right) A photo of the MWL120 camera at JCNS-2 which was used in this work.

4.3 Huber G670 powder diffractometer

A schematic view of the device Huber G670 diffractometer is shown in Fig.4.3 [63]. It consists of five basic components: the detector, a sample platform, a collimator, a monochromator, and the X-ray source. The system uses monochromatic $K\alpha_1$ radiation of a wavelength of 1.541 \AA , which is selected with the help of a Germanium single crystal that is placed between the sample and the source of the X-ray beam. Before this monochromatic beam hits the sample passes soller slits (collimator) which reduces the divergence of the radiation. The detector of the Huber G670 camera is an integrated system of a laser recording unit that contains a photomultiplier and preamplifier to record and read the information of the scattered beam. This information is then digitally transformed to obtain the recorded intensity as a function of 2θ which can be visualized on the computer screen. Finally, to delete the recorded signal on the image plate, a halogen white lamp is used [63].

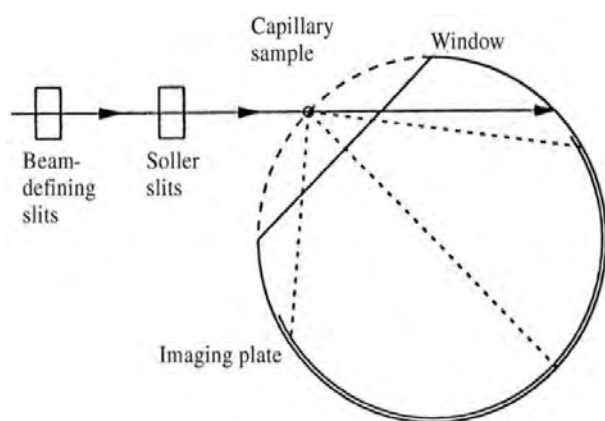


Fig.4.3 (left) Schematic view of the G670 diffractometer [8], (right) Huber G670 Powder Diffractometer at JCNS-2.

The Huber G670 powder diffractometer is used in this work to collect powder diffraction patterns of a polycrystalline sample of $Mn_{4.2}Ge_{2.4}Fe_{.8}Si_{.6}$ and to check the phase purity of the sample and determine the lattice parameters of this compound.

4.4 Vibrating sample magnetometer (VSM) of physical property measurement system (PPMS)

The vibrating sample magnetometer (VSM) option in the quantum design physical property measurement system (PPMS) Dynacool was used to perform the DC magnetization measurements for a Mn_5Si_3 single crystal and of a polycrystalline sample of $Mn_{4.2}Ge_{2.4}Fe_{.8}Si_{.6}$.

The quantum design physical property measurement System (PPMS) [64] allows many different measurements, like thermal properties, electrical transport properties, specific heat, and magnetic measurements. The PPMS Dynacool is a further developed edition of the (PPMS) which provides similar capabilities without requiring an external liquid-based cooling system. The generation of PPMS employed in this work uses a single, two-stage pulse tube cryocooler for temperature control and a superconducting magnet, this way using a minimum amount of condensed liquid He^4 .

There are many measurement options in this system like AC resistivity, heat capacity, ACMSII (AC susceptibility), and the VSM (Vibrating Sample Magnetometer) option. Each of the previous options has a special option in the software, different sample holders, and different measurement inputs.

The vibrating sample magnetometer (VSM) [65], is a measurement Option in which the sample is placed on a high-precision linear actuator that oscillates linearly between coils surrounded by a highly uniform magnetic field. This vibratory motion of the sample will generate a difference in voltage, according to Faraday law, (see Fig.4.4).

The measurement of the induced voltage in the coils allows the determination of the magnetic moment of the sample as a function of field or temperature.

In this thesis, (VSM) Option Magnetization Measurements were performed to investigate the macroscopic magnetic properties of Mn_5Si_3 and $Mn_{4.2}Ge_{2.4}Fe_{0.8}Si_{1.6}$ compounds.

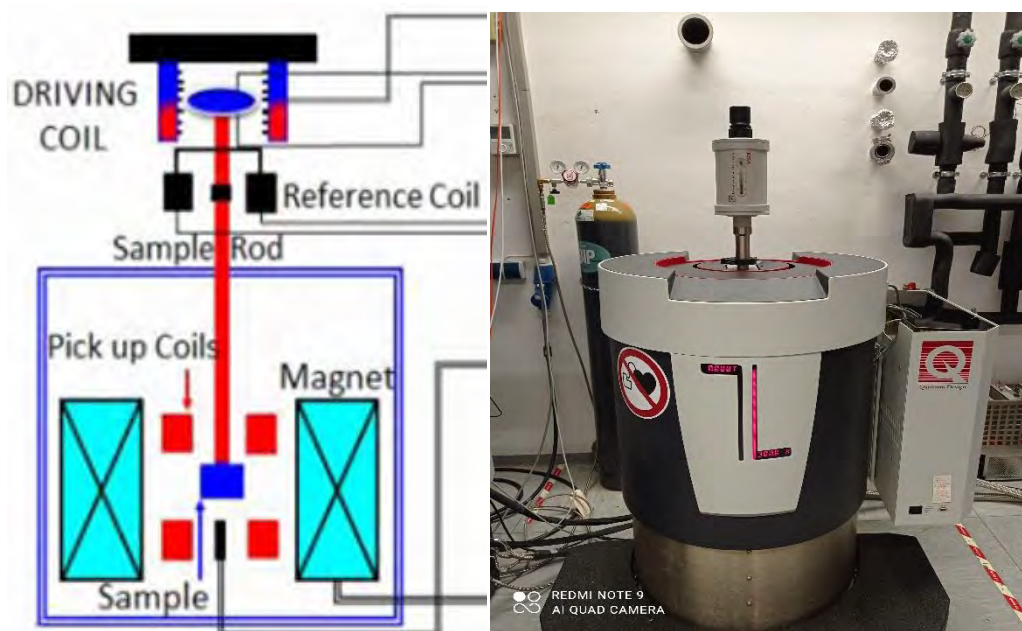


Fig.4.4 (left) Schematic View of VSM option [5], (right) PPMS Dynacool at JCNS-2.

5 Experimental procedures

5.1 Experimental part concerning Mn_5Si_3 samples

5.1.1 Sample preparation

5.1.1.1 Sample synthesis and single crystal growth

The sample of this work was a part of the single crystal that was also investigated in [66] and prepared according to the procedures described there. Stoichiometric proportions of high purity ($\geq 99.9\%$) Mn and Si were melted using cold crucible induction melting in argon atmosphere [60]. The ingot was melted four consecutive times to ensure the homogeneity of the intermetallic alloy. The Polycrystalline sample of Mn_5Si_3 was characterized by the powder x-ray diffraction at room temperature and it was confirmed, that there were no impurity phases. The Polycrystalline samples were then used to grow a single crystal using the Czochralski method [67].

5.1.1.2 Laue diffraction experiment using MWL120 camera

To perform the magnetization measurements in DC fields with the field applied in a defined crystallographic direction, the orientation of the crystals has to be defined.

MWL120 real-time back-reflection Laue camera equipped with a multiwire detector and a tungsten X-ray tube were used to identify the direction crystallographic axis. As a first step, the sample was fixed on the holder with a piece of doubled face sticker, it was ensured that the sample was adhered well before placing the holder on a rotatable platform inside the camera cabinet (**Fig.5.1 (a, b)**). After fixing the holder, the user can control the movement of the crystal easily by a motor and at the same time viewing the image on the screen in real time. The program OrientExpress 3.4 [68] was used to simulate the Laue patterns in the different crystallographic directions. The simulated patterns were compared with the real-time Laue image, and the sample was rotated until real and simulated image matched (**Fig.5.1 (d)**).

Three different samples of single crystals of Mn_5Si_3 were oriented with respect to the crystallographic [100] axis, [1-20] axis and [001] axis of the hexagonal unit cell. Then,

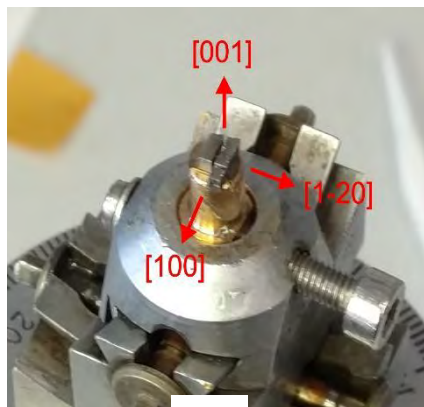
to obtain samples close to a cubic shape and weights around 7.0 mg, we used spark erosion to cut the samples (**Fig.5.1 (c)**). After cutting, the orientations were re-checked using MWL120 Laue camera. Finally, three samples were obtained ready for the magnetization measurements (**Fig.5.1 (e)**).



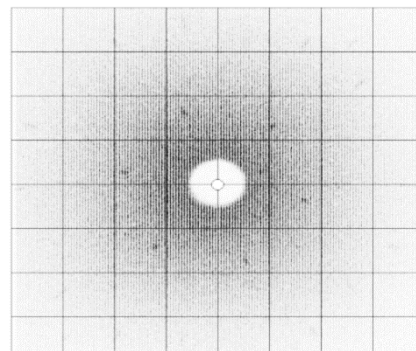
(a)



(b)



(c)



(d)



(e)

Fig.5.1 (a) Fixing the sample on the holder. **(b)** Inserting the holder inside the MWL120 Laue camera. **(c)** The samples cut with spark erosion. **(d)** An image for Mn_5Si_3 single crystal along [001] axis obtained from the Laue camera. **(e)** The three oriented samples of Mn_5Si_3 along [100], [1-20] and [001] axis.

5.1.2 Magnetization measurements

In this section, I will provide explanations about the isofield and the isothermal magnetization measurements protocols.

To investigate the macroscopic magnetic properties of Mn_5Si_3 single crystal, DC field magnetization measurements were performed. Two protocols were adopted in this work, iso-thermal and iso-field magnetization measurements.

The vibrating sample magnetometer (VSM) option in the quantum design physical property measurement system (PPMS) Dynacool was used to accomplish the measurements.

5.1.2.1 Iso-field magnetization measurements

The Iso-field magnetization measurements were performed with magnetic fields directed along the [001], [100], and [1-20] crystallographic directions. These three directions were chosen as they are the symmetry directions in the hexagonal system.

In the first experiment the magnetization measurements were performed with magnetic field $H \parallel [001]$.

The sample was weighed, as the magnetization will be calculated as magnetic moment per the unit mass of the sample. The 6.3 mg sample and the holder were cleaned carefully with acetone, then a very tiny amount of GE varnish was used to glue the sample at a specified location on the holder. This specific location is determined by a mounting station which is used to confirm that the position of the sample on the holder is appropriate. It is an external scale that recommends $35 \pm 3 \text{ mm}$ as location for the sample (**Fig.5.2 (a)**). Then, the sample was placed under the light for more than 20 minutes, to ensure that the glue was dried and then wrapped with Teflon (**Fig.5.2 (b)**). After that, the holder was fixed to a special stick and with care, the rod was finally entered into the Dynacool system.

It is worth mentioning that the process of fixing the sample with the correct direction on the holder is a delicate process that requires stability of hand movement to ensure putting it in the right direction.

Initially, a new datafile was created, to include the scan sequence of the measurements and then the sample was exposed to a small field of 100 Oe (**Fig.5.2 (c)**) to make sure that the sample is in the center of the magnetic field (i.e., within the range of the recommended line $35 \pm 3mm$).

Later on, the temperature of the sample was cooled down from 120 K to 10 K. The sequence of the measurements was entered with a scan field from 0.5 T to 8.5 T at 198.0 Oe / sec, in 9 steps. In practice this means that the magnetic field was fixed at 0.5 T and the magnetization was measured as a function of temperature in a first step, then the magnetic field was set to 1.5 T and the magnetization was measured as a function of temperature again and so on up to 8.5 T.

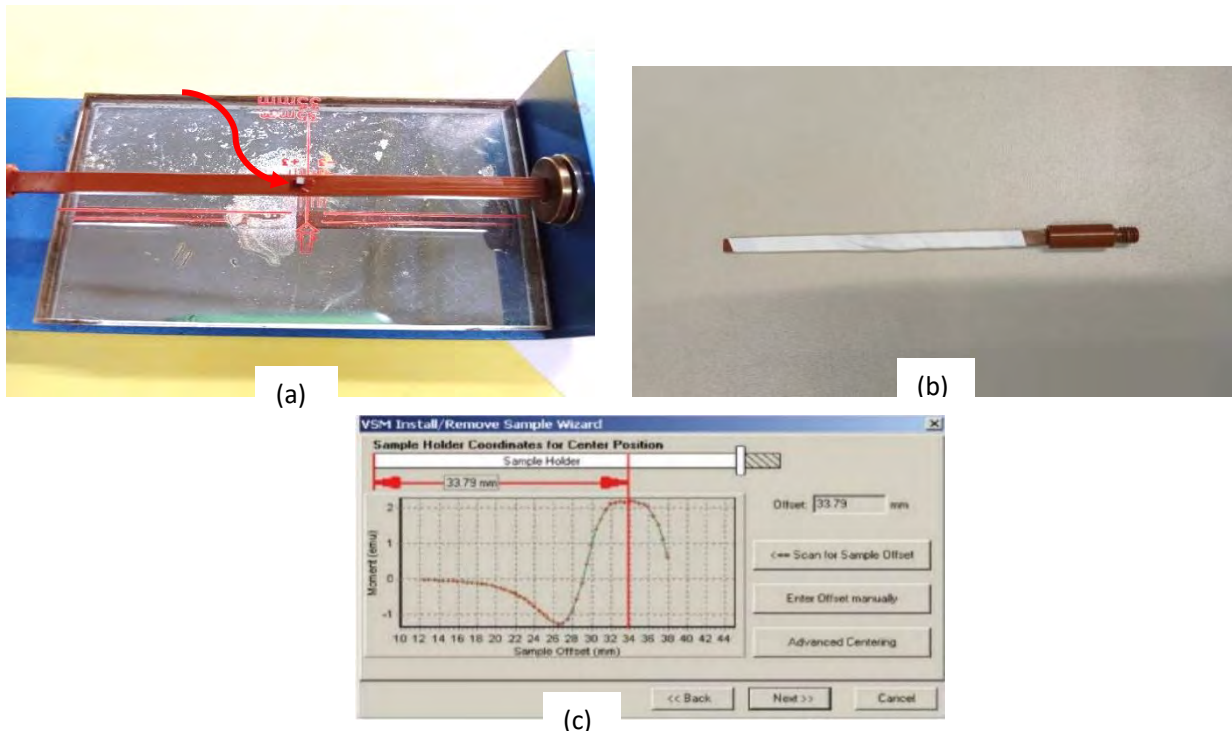


Fig.5.2 (a) Fixing the sample on the holder at a specific location using the mounting station, the red arrow is pointing to the sample. (b) The sample after Teflon covering. (c) The dialogue for the sample centering scan.

5.1.2.2 Iso-thermal magnetization measurements

After the iso-field magnetization measurements were performed with $H \parallel [001]$, the iso-thermal magnetization measurements were executed for the same sample with the same field direction ($H \parallel [001]$). The sequence was fast cooling to 10 K in 100.0 Oe field. Then, measurements were implemented with a field range from -9 T to 9 T (full hysteresis) with a sweep rate of 50.0 Oe/sec, starting from 10 K to 76 K in 3 K steps.

A second set of measurements were done on the second sample (7.3 mg) with the magnetic field directed along $[100]$ with the same previous isofield sequence, yet the isothermal sequence was started from 10 K and measured up to 120 K in 5 K Steps.

These two protocols were repeated afterwards for the other remaining sample (7.7 mg) with the magnetic field applied along $H \parallel [1-20]$.

5.2 Experimental part corresponding to the $Mn_{4.2}Ge_{2.4}Fe_{0.8}Si_{0.6}$ sample

5.2.1 Sample preparation

5.2.1.1 Synthesis of the polycrystalline sample of $Mn_{4.2}Ge_{2.4}Fe_{0.8}Si_{0.6}$

Stoichiometric amounts of high purity (> 99.98 puriyt) elements of Mn, Ge, Fe, and Si (**Fig.5.3 (left)**) corresponding to the composition of $Mn_{4.2}Ge_{2.4}Fe_{0.8}Si_{0.6}$ were used for cold crucible induction melting (CCIM). An amount of 10 g of $Mn_{4.2}Ge_{2.4}Fe_{0.8}Si_{0.6}$ was targeted, the real weighed mass was 9.996 g.

As a first step, the metal pieces were placed inside the crucible by clean sterile forceps. Larger pieces were put first and then the smaller ones, to ensure that the pieces did not fall out from the lower hole of the crucible. Then the glass cover was placed over the crucible, the chamber was sealed, and the vacuum pressure (10^{-6}) mbar was activated. This ensures the purity of the resulting compound. The components were carefully heated until the sample began to glow, which is noticeable visually. After this the Aragon atmosphere was activated with a pressure of 1000 mbar, and the high-frequency electric current (AC) started to melt the sample. To achieve high homogeneity, the sample was re-melted four times. Before each melting cycle the sample was turned upside down (**Fig.5.3 (right)**).



Fig.5.3 (left) The containers of the high purity elements of Mn , Ge , Fe , Si , (right) Cold Crucible Induction Melting device, (right) The glowing sample is visible.

5.2.1.2 X-ray powder diffraction using Huber G670 diffractometer

X-ray powder diffraction was used to check the phase purity of the synthesized $Mn_{4.2}Ge_{2.4}Fe_{0.8}Si_{0.6}$ sample and to determine the lattice parameters of the unit cell of this compound.

After obtaining the synthesized polycrystalline sample from CCIM (**Fig.5.4 (a)**), its outer surface was cleaned with sandpaper to remove any stuck contaminations. After that, the sample was crushed inside a mortar to get a very fine and homogenous powder. Before this step, the mortar was cleaned with sand and water and sterilized with alcohol to ensure that any suspended pollutants, which may affect the purity of the compound, were removed (**Fig.5.4 (b, c, d)**).

For the X-ray powder diffraction experiment using the G670 diffractometer, milligrams of fine and homogenous powder of the compound were sufficient. In a first step, the sample holder was cleaned with isopropanol, then a suitable piece of foil (cellophane) was cut and was placed on the holder. Milligrams of the powder were placed in the center of a recommended rectangle a few drops of isopropanol were added and

everything was mixed to spread the sample in a flat and homogenous manner within the recommended area. The sample was left for a few seconds to dry slightly, then another piece of foil was applied to cover the sample. Finally, a special metal ring was pressed on the borders of the holder and the excess of foil was cut from the surroundings (see **Fig.5.5 (left)**). The use of the cellophane foil is feasible, as this material is sufficiently transparent and amorphous, so the powder diffraction patterns will not be significantly affected, although the background may be slightly increased.

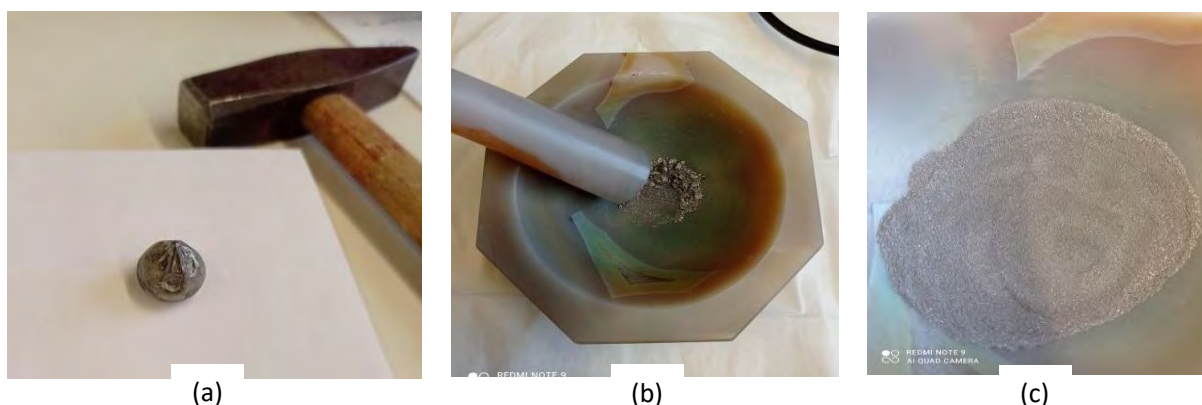


Fig.5.4 (a) Polycrystalline sample as obtained from CCIM. (b) Crushed sample inside a mortar. (c) Final fine homogenous powder of $Mn_{4.2}Ge_{2.4}Fe_{0.8}Si_{0.6}$ compound.

Afterwards the sample was ready to be exposed to the X-ray and was placed in the appropriate position inside the Huber G670 diffractometer system (**Fig.5.5 (right)**). CuK_{α} radiation with $\lambda = 1.541 \text{ \AA}$ was used. The measurement was performed at room temperature with 360 min of exposure time. During the exposure process, the sample holder moves in a harmonic horizontal frequency (1 Hz), to get better data by ensuring that more powder grains of different orientations are exposed to the radiation.

Once the diffraction diagram was obtained, a LeBail refinement was performed to check the phase purity of $Mn_{4.2}Ge_{2.4}Fe_{0.8}Si_{0.6}$ polycrystalline sample [50], but unfortunately no satisfactory match between the calculated and the observed diagram could be obtained (more details about the LeBail refinement in the theory chapter). To check the chemical composition, a chemical analysis was performed for this. iCAP 6500 the device was used. 100mg of $Mn_{4.2}Ge_{2.4}Fe_{0.8}Si_{0.6}$ powder was divided into two halves, and each quantity was dissolved separately in 3 mL of HCL/3 mL of H_2O_2 for

half an hour at room temperature. Out of 50 ml of each solution two 200-fold parallel dilutions were made for each solution, and finally, they were entered to the chemical analysis device.

Due to the problems in the LeBail fitting procedure, a second batch of the compound was synthesized following the above-described procedure. This time a lower rate of cooling was used (for the first sample the melt froze within a couple of seconds, for the second sample it took about one minute) to ensure a good crystallinity. Also, on the second sample an X-ray powder diffraction experiment was performed.



Fig.5.5 (left) Powder sample inserted in sample holder to be used in x-ray diffraction experiment, (right) The Huber G670 diffractometer system in JCNS-2.

5.2.2 Magnetization measurements

The magnetization measurements were performed to characterize the macroscopic magnetic characteristics of $Mn_{4.2}Ge_{2.4}Fe_{0.8}Si_{0.6}$. Two protocols were adopted in this work, iso-thermal and iso-field magnetization measurements. For the isofield measurements two procedures were used: The Field cooling (FC), and the Field warming (FW). Isothermal measurements were performed upon cooling. A detailed explanation about these protocols follows below.

The Vibrating Sample Magnetometer (VSM) option in the Quantum Design Physical Property Measurement System (PPMS) Dynacool was used to perform the measurements.

As the first step of the sample preparing procedure, 1.7 mg of the fine powder was placed inside a special capsule, then the sample was compressed and the capsule was sealed (**Fig.5.6**). The capsule was weighed empty and full and the net weight of the sample was determined. In the next step the sample was fixed on a clean and sterilized trough-shaped holder. An external scale was used to confirm that the position of the sample was $(35 \pm 3 \text{ mm})$. Finally, the holder was fixed to a special stick and with care the rod was entered into the Dynacool system.

The sample was exposed to a small field (100 Oe), as a first step to make sure that it was placed in the right position.

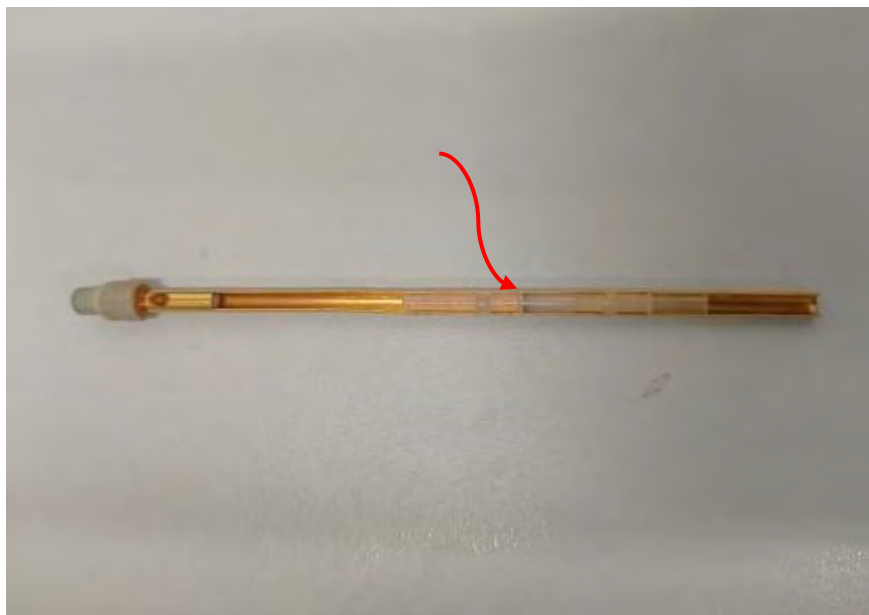


Fig.5.6 Trough-shaped holder in which the capsule of the sample is inserted, the red arrow is pointing to the sample.

5.2.2.1 Iso-field and iso-thermal magnetization measurements

The sequence of the isofield magnetization measurements were performed in two modes, FC and FW at an applied magnetic field of 0.1 T. During the FC mode, the magnetization was measured as a function of temperature while cooling the sample from 350 K to 20 K. The FW mode was activated at 0.1 T, while heating the sample from 20 K to 350 K in 10 K step, and the magnetization was recorded as a function of temperature.

The isothermal magnetization measurements were performed upon cooling the sample from 350 K to 20K in 10K step, with full hysteresis measurement in the field range of $\pm 2 T$.

Regarding the experimental data in this thesis, the source of uncertainties in the data comes from the sweep rate and the measurements time, as both the temperatures and the magnetic field settings are changing during the measuring process.

6 Data analysis (results and discussions)

6.1 Laue diffraction of Mn_5Si_3 single crystal samples

The OrientExpress 3.4 software was used as a simulation program to determine the Laue patterns corresponding to certain crystallographic directions. To distinguish the crystallographic direction to which an image belongs, one relies on measuring the angles between certain diffraction spots that were recorded by the Laue camera detector and a reference axis. Then the angles between the image of stereographic projection from the real-time Laue camera and the image from the simulation program along the assumed crystallographic direction are compared and -if they match- the orientation of the crystal is confirmed. **Fig.6.1,2** show the axis-recognition process for the [100] and [120] directions of the hexagonal unit cell of Mn_5Si_3 , respectively.

Regarding the identification of the projection along the [001] direction, it is sufficient to rely on a simple visual inspection, as the 6-fold symmetry along this direction is clearly visible. **Fig.6.3** represents the real time Laue image along this direction.

As explained before, the magnetization measurements were performed with magnetic fields directed along the [001], [100], and [1-20] crystallographic directions. These three directions were chosen as they are the symmetry directions in the hexagonal system. The crystals were oriented along these directions using the Laue camera and then cut to suitable sizes by spark erosion. However, all magnetization measurements in this thesis will be presented with respect to the ortho-hexagonal setting and referring to the corresponding orthorhombic directions, a, b and c axis. In this setting the crystallographic direction [001] of the hexagonal unit cell system corresponds to the c-direction of the orthorhombic unit cell, the [100] direction of the hexagonal unit cell coincides with the b-direction of the orthorhombic unit cell, while the hexagonal [1-20] direction is parallel to the a-direction of the orthorhombic unit cell.

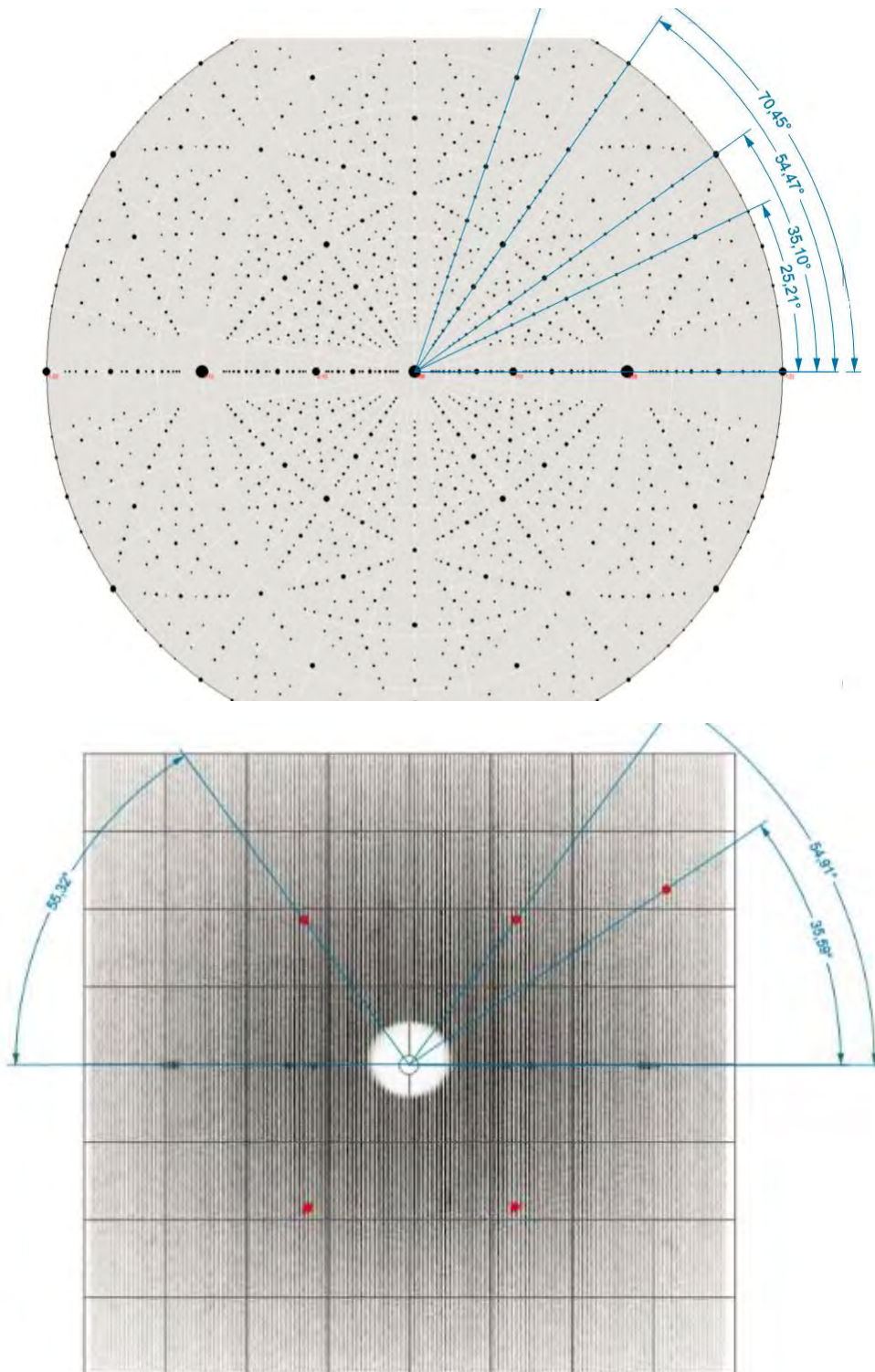


Fig.6.1 (top) The calculated stereographic projection based on the lattice parameter from an Mn_5Si_3 single crystal along the [100] direction as obtained from the OrientExpress 3.4 program. **(bottom)** The real-time Laue camera image along the same crystallographic direction.

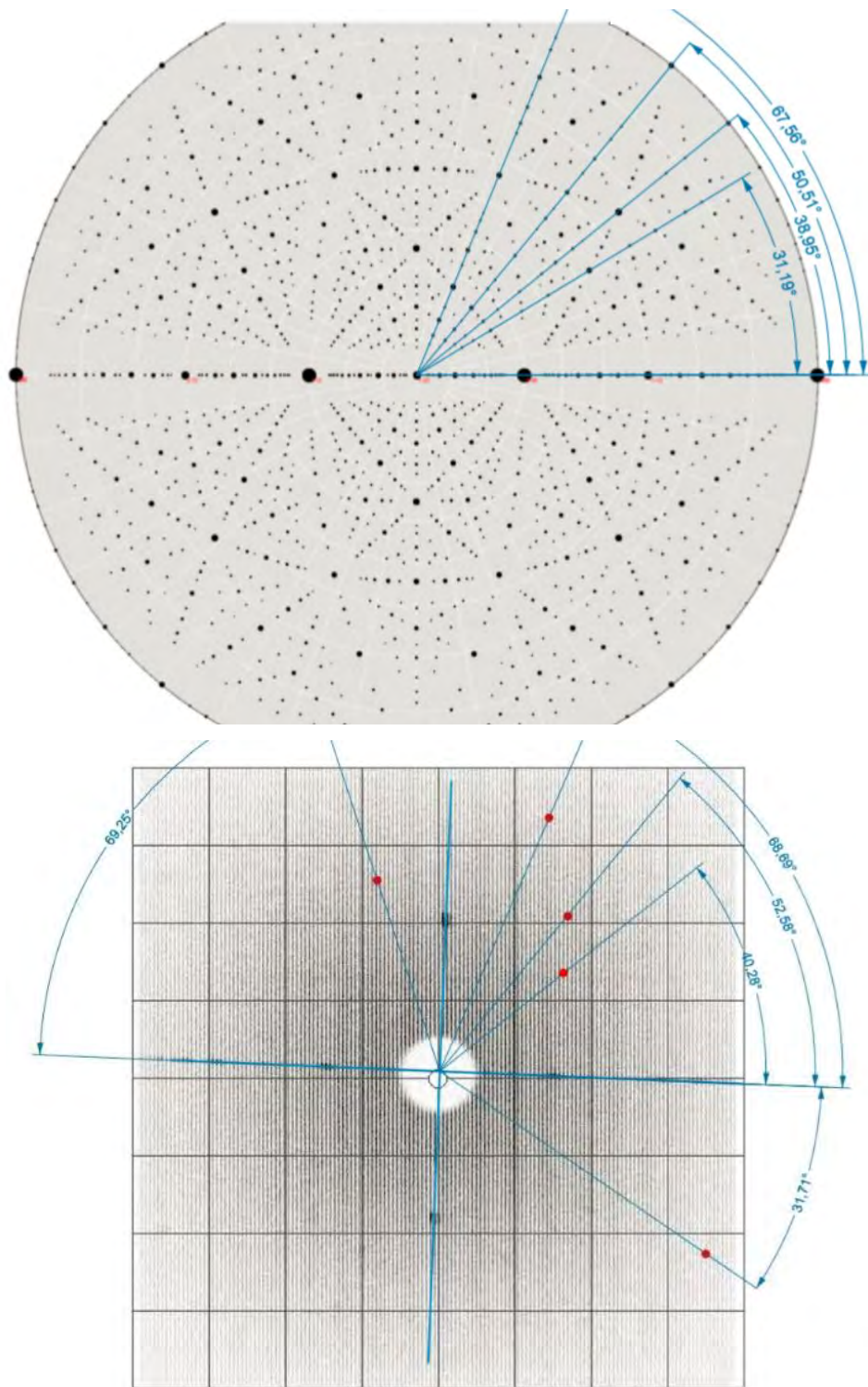


Fig.6.2 (top) The calculated stereographic projection based on the lattice parameter from an Mn_5Si_3 single crystal along the [120] direction as obtained from the OrientExpress 3.4 program. (bottom) The real-time Laue camera image along the same crystallographic direction.

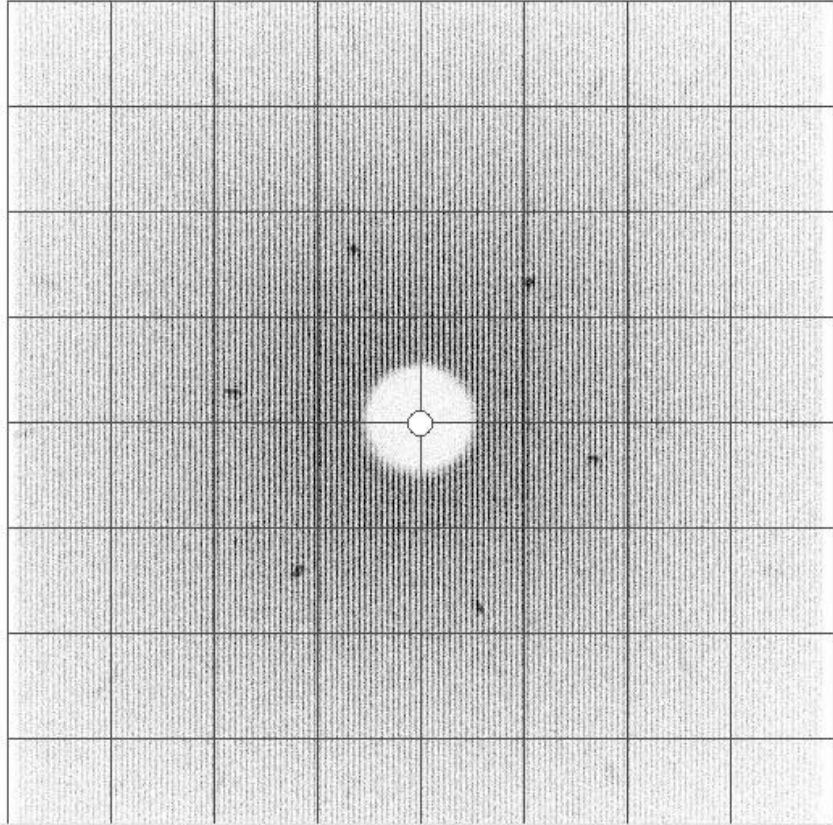


Fig.6.3 The real-time Laue camera image along the [001] direction of Mn_5Si_3 .

6.2 The LeBail refinement of $Mn_{4.2}Ge_{2.4}Fe_{0.8}Si_{0.6}$ powder diffraction data

The powder diffraction data of $Mn_{4.2}Ge_{2.4}Fe_{0.8}Si_{0.6}$ measured using the Huber G670 diffractometer were refined with the LeBail method [46]. The fit served to determine the unit cell parameters of the crystal structure, and to check the phase purity of the sample. The program Jana2006 [50] was used to perform this refinement. For the starting model, lattice parameters of this sample were entered according to the work of K. Al-Namourah [9]. Two crystalline phases were introduced to fit the observed profile to the calculated one, as it was not possible for all the peaks to be indexed by the lattice parameters of one single phase. The background was adjusted manually and a pseudo-Voigt function was used to fit the peak shapes. The pseudo-Voigt function is a linear combination between a Lorentzian and a Gaussian function. For the Gaussian part, the Gaussian parameter GW was used while LX was used as a fit parameter for the Lorentzian part. To describe the width of the peak profile, a FWHM parameter of 8 was used as a cut-off value for both phases. FWHM parameter is the abbreviation of (full width at half maximum) which describes the width of a peak profile at the half of its height.

A zero-shift parameter was also refined. **Fig.6.4** illustrates the LeBail refinement as obtained in Jana2006. The difference between the observed and calculated profiles is represented as difference curve at the bottom, while the vertical marks indicate the position of the peaks of the two phases.

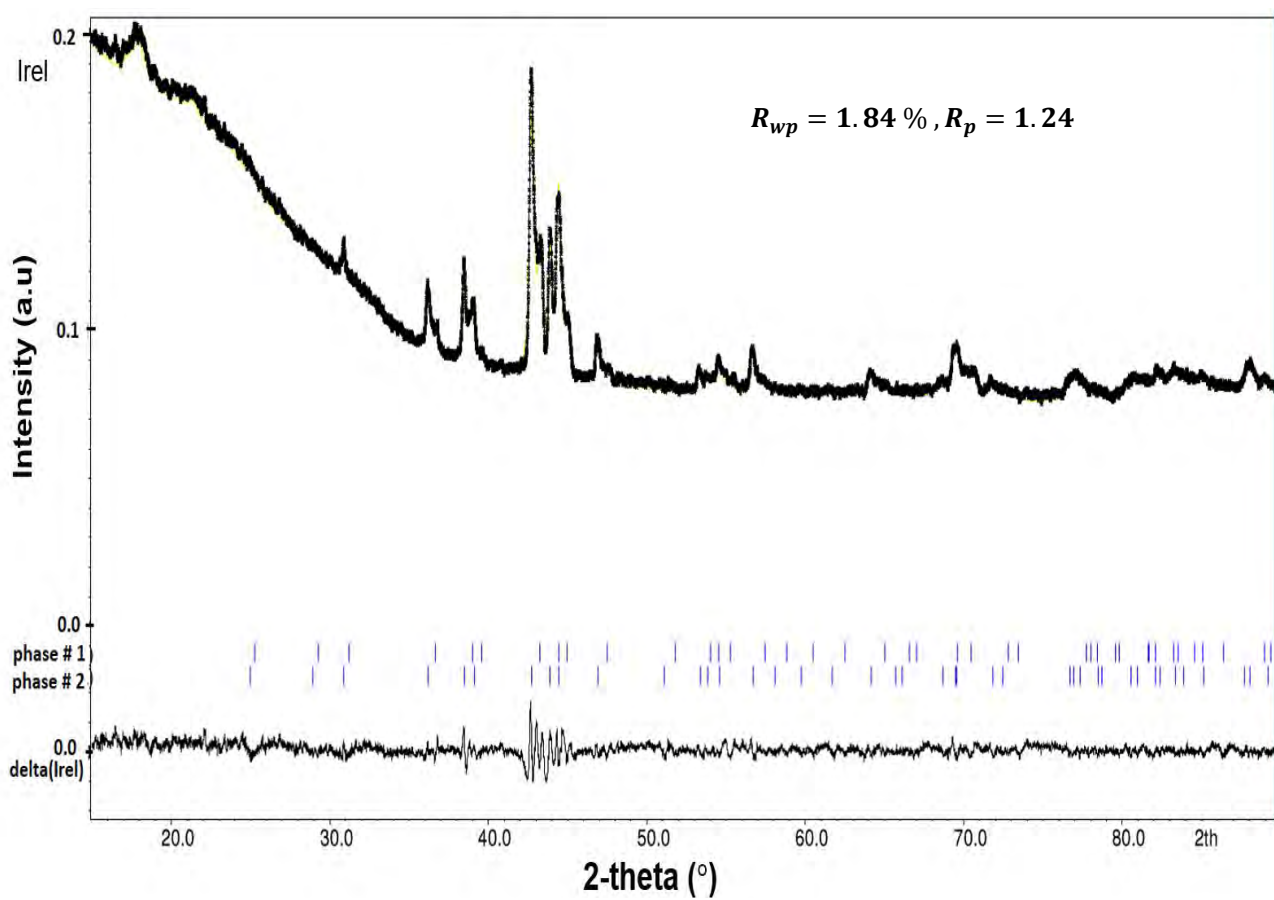


Fig.6.4 The LeBail fit of the room temperature data of $Mn_{4.2}Ge_{2.4}Fe_{0.8}Si_{0.6}$ using two phases and the resulting difference profile from Jana2006.

Table (6.1) provides the information about the initial lattice parameter from [9] and the refined lattice parameters of the two phases in the sample of $Mn_{4.2}Ge_{2.4}Fe_{0.8}Si_{0.6}$ investigated here. For both phases the space group $P6_3/mcm$ was assumed. A comparison of the refined lattice parameters of the newly synthesized sample shows that they are very similar to the ones obtained in [9].

Table (6.1) The initial unit cell parameters and the parameters from the LeBail refinements of the patterns measured with the Huber diffractometer of $Mn_{4.2}Ge_{2.4}Fe_{0.8}Si_{0.6}$ powder sample.

Phase no.	$a=b$ (Å)	c (Å)
	Initial parameters *	
Phase # 1	7.153(2)	4.970(2)
Phase # 2	7.084(3)	4.914(2)
	Final parameters	
Phase # 1	7.156(2)	4.972(2)
Phase # 2	7.073(3)	4.916(2)
R-factors of the final refinement:		
	$R_{wp} = 1.84\%$, $R_p = 1.24$	

*Source of data : K. Al-Namourah [9]

6.3 Magnetization measurements on Mn_5Si_3

6.3.1 Magnetization measured under isofield conditions

In the context of investigating the macroscopic magnetic properties of Mn_5Si_3 , isofield magnetization measurements were performed with the field applied along the three crystallographic directions a, b, and c of the orthorhombic unit cell. The magnetization curves as a function of temperature ($M(T)$) were performed for different magnetic field settings, starting from 0.5 T to 8.5 T with a 1.0 T step.

Based on the $M(T)$ curves, the molar magnetic susceptibility (χ_{mol}) was calculated. **Fig.6.5**, shows the χ_{mol} for different magnetic field settings along the three crystallographic directions.

In general, upon cooling from 120 K to 60 K, all curves for all magnetic field settings increase and reach the highest point (indicated by a red-dashed line in **Fig.6.5**) at the transition temperature from the collinear to the non-collinear antiferromagnetic phase before exhibiting a sharp decrease. With the exception of the 0.5 T filed curve, both the maximum and the edge of the curves shift toward lower temperatures as the magnetic field setting increases.

For the 0.5 T setting, the behavior of the curves is different compared to the larger magnetic field settings and the maximum susceptibility occurs at the lowest temperatures when $H \parallel c$ -direction.

Again, for an applied magnetic field of $\mu_0H \leq 1.5$ T parallel to the b-direction, a small broad peak in the magnetization is observed around 100 K which is attributed to the phase transition from PM to AFM2 (indicated by a blue arrow in **Fig.6.5**).

For low magnetic fields ($\mu_0H \leq 4.5$ T), the magnetic response curves increase again in the low temperature range (< 40 K), and continue increasing with further decrease of the temperature. At about 20 K the susceptibility rises at a slower rate. Comparing the different directions for magnetic fields ($\mu_0H \leq 4.5$ T), the response below 40 K is the strongest, if the field is applied $\parallel c$.

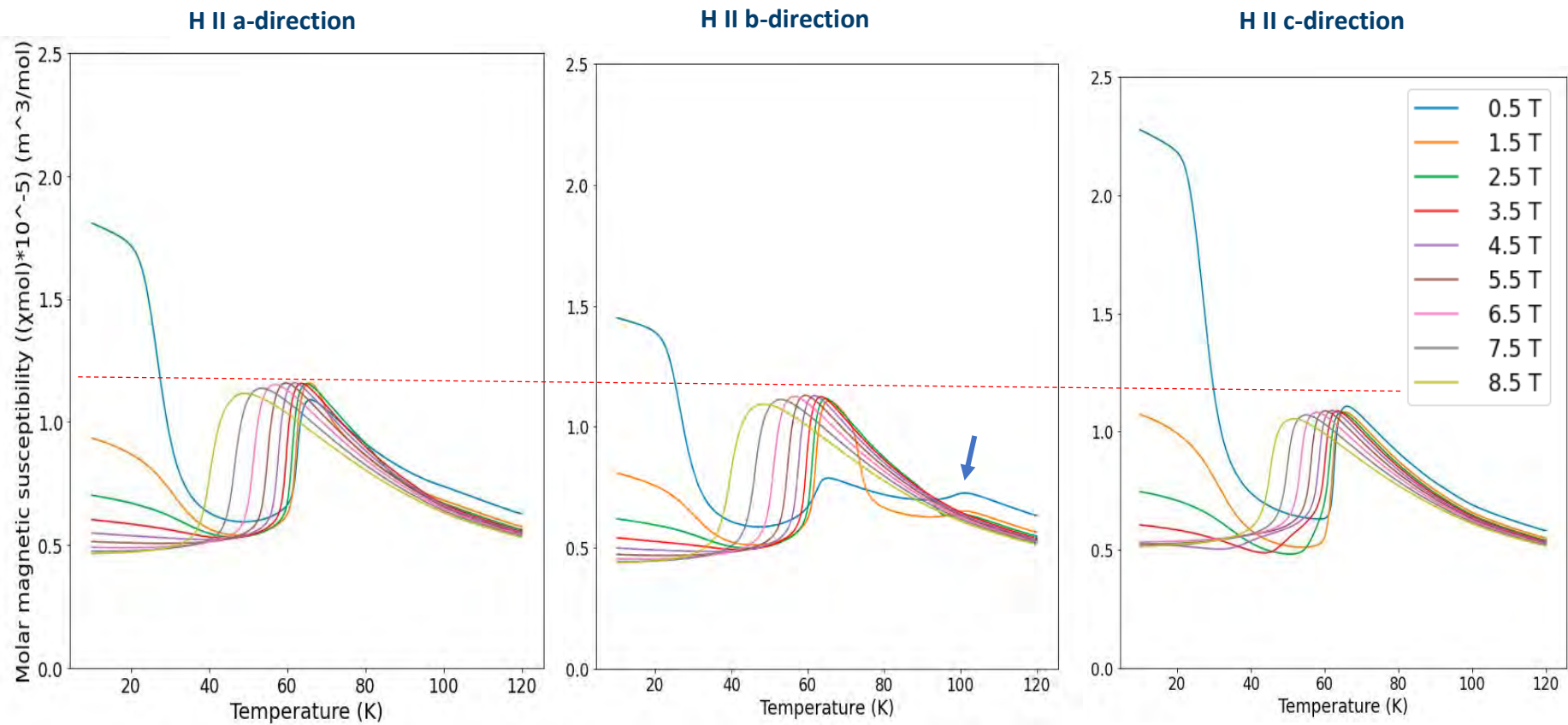


Fig.6.5 Molar magnetic susceptibility of Mn_5Si_3 single crystal with fields of varying strength applied along the different crystallographic directions.

Fig.6.6 compares the $M(T)$ curves for two different field settings, 1.5 and 7.5 T. In general, for a given temperature, the magnetic response is strongest for a field along the a-direction above 45 K, while for lower temperatures, the magnetization values are higher when the field is parallel to the c-direction.

For the low field setting 1.5 T (**Fig.6.6 (top)**), the maximum magnetization occurs when $H \parallel$ a-direction around the transition temperature from the collinear to the non-collinear antiferromagnetic phase (AFM2-AFM1) around 66 K. Both, the maximum and the inflection point are basically equal for the three directions (indicated by a red dashed line in **Fig.6.6 (top)**). Only for the field \parallel b-direction, the magnetization curve of (1.5 T) shows an apparent change that can be attributed to the transition from the AFM2 to the paramagnetic phase at $\sim 100K$.

Concerning the higher magnetic field setting (7.5 T) (**Fig.6.6 (bottom)**), the material still exhibits the maximum magnetization around the transition temperature of (AFM2-AFM1) phase, if the magnetic field is applied along the a-direction. On the other hand, the transition temperature of the AFM2 to the AFM1 phase is shifted to a lower temperature if the magnetic field is applied in the ab-plane. Different from the low field behavior, the shift is stronger, if the field is applied \parallel to the a- or b-direction than if it is applied \parallel to the c-direction (indicated by a red dashed arrow in **Fig.6.6 (bottom)**).

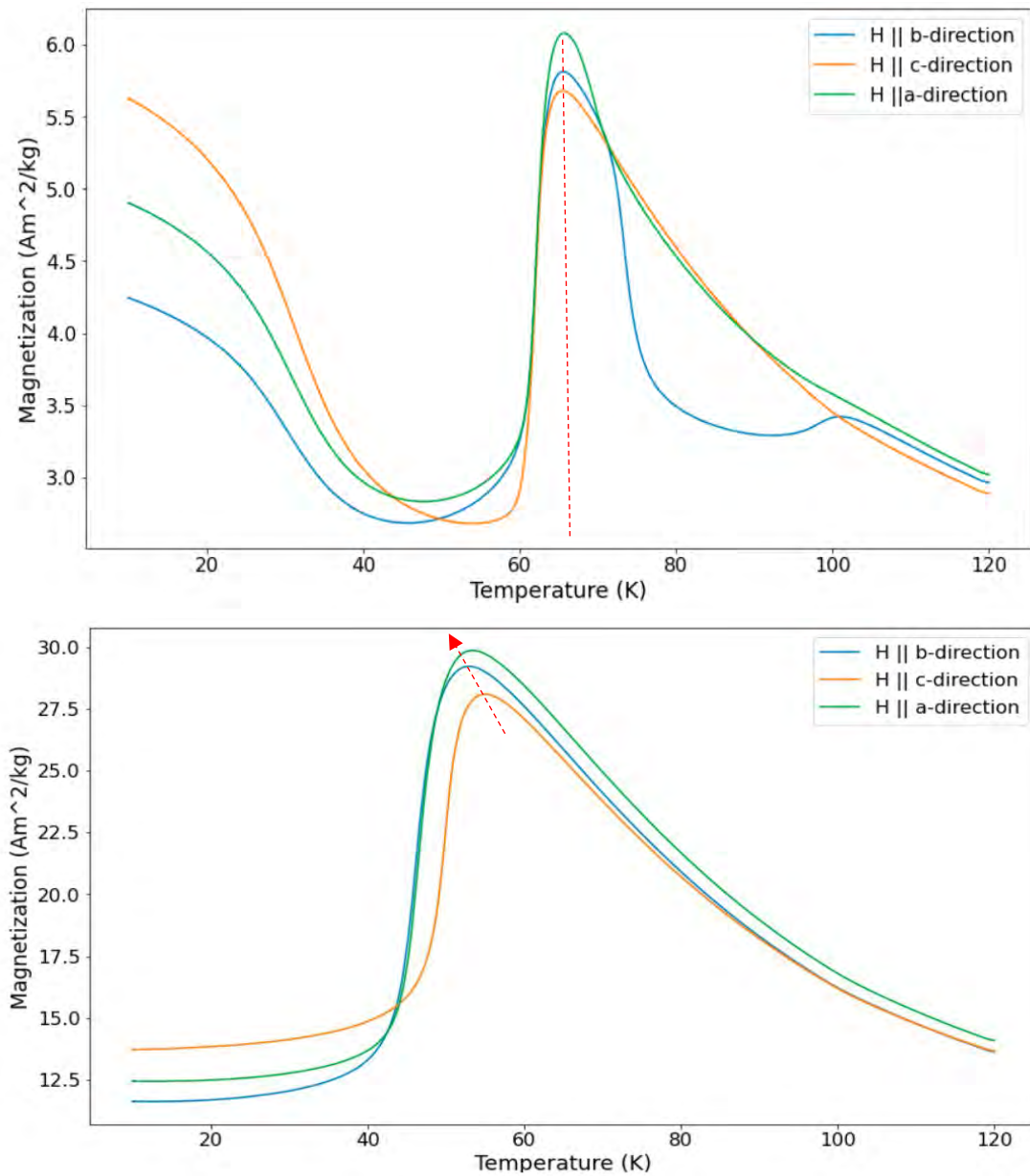


Fig.6.6 (top) The isofield magnetization curves $M(T)$ of the three crystallographic directions, at $H = 1.5$ T and at $H = 7.5$ T (bottom).

6.3.2 Magnetization measured under isothermal conditions

6.3.2.1 Magnetization measurements with H applied || to the a- and b-direction

The mass magnetization was also measured as a function of the applied magnetic field along the three crystallographic a, b, and c-direction under isothermal conditions. As the results of magnetization measurements with the field along the a- and b-direction are similar, only the measurements with the field along the b-direction will be provided in this section.

Fig.6.7 shows the $M(B)$ curves for all the measured temperatures, starting from 10 K to 120 K in 5K step, for decreasing field from 9T to -9 T. Three main features are observed. The first one (i) is a sharp kink at low temperatures (<25 K) and low magnetic fields (<1.0T). The second observation (ii) is a steep change in the magnetization curves in the temperature range between 30 and 70 K, which moves towards lower fields with increasing the temperature. This feature is linked to the transition from the AFM1' to the AFM2 phase. Feature (iii) is observed as a small kink in the $M(B)$ curves, in the high temperature range (70-100) K and at low magnetic fields.

To extract the field and the temperature behavior of these features, (dM/dB) was calculated numerically after a rebinding of the data with a step size of 25 mT.

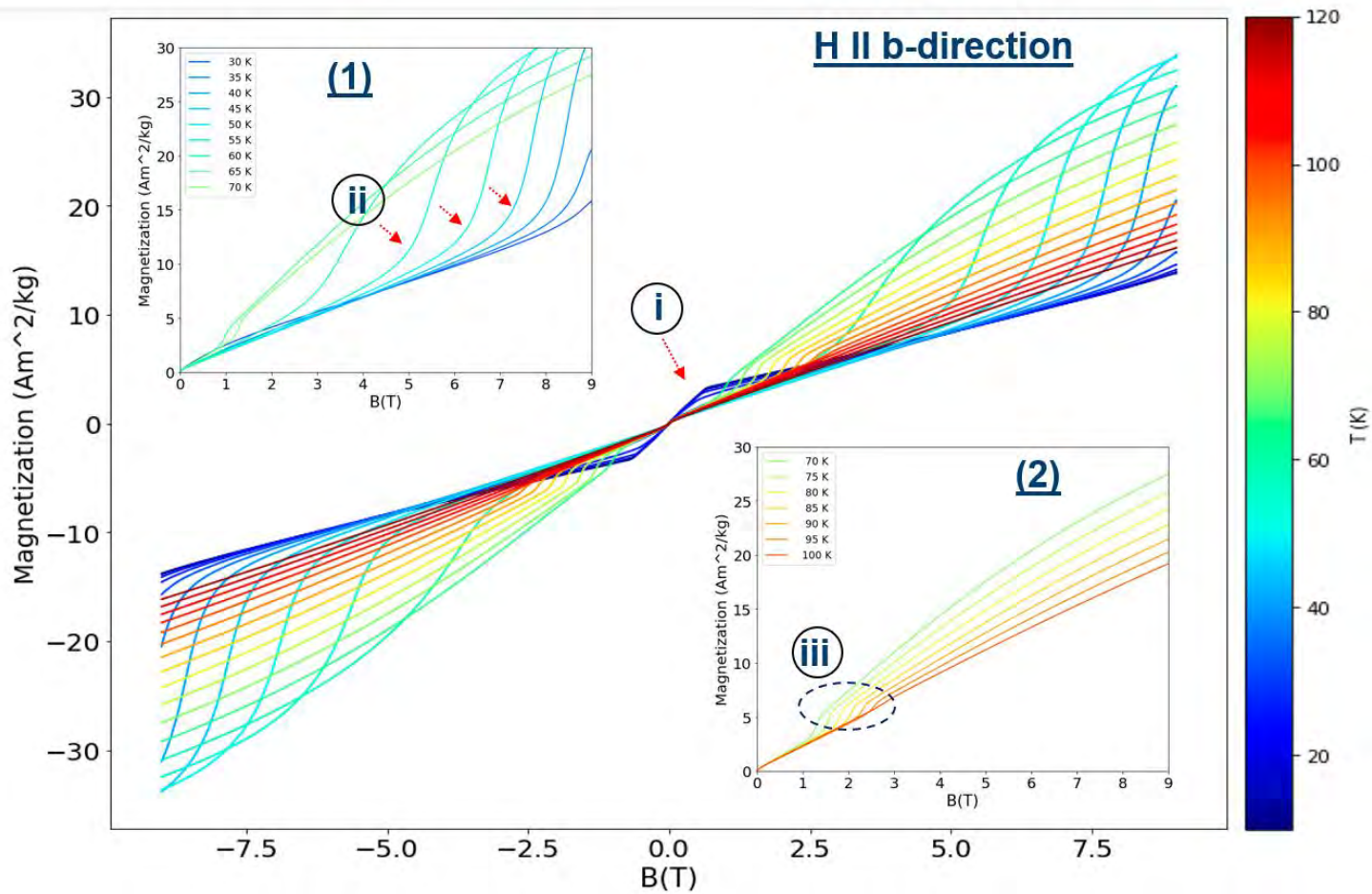


Fig.6.7 The field-dependent magnetization curves ($M(B)$) of Mn_5Si_3 . Decreasing H data, $H \parallel b$ -direction, in the temperature range 10 K - 120 K. (i) the low temperature-low magnetic field observation, (ii) the observations of the phase transition from AFM1'-AFM2, and (iii) the high temperature-low magnetic field feature.

Fig.6.8 shows the derivative of magnetization with respect to B (dM/dB) as a function of B, individually for the increasing (the dashed lines) and the decreasing (the solid line) field branch of the applied field loop. The broad structured peaks at low temperatures and low magnetic fields correspond to the feature (i) in **Fig.6.7**. Below 20 K, there is a step down of those peaks like decreasing the derivatives, which then broadens gradually. However, a very narrow peak still exists at highest temperature around 95 K. This feature hardly depends on the sign of the field change.

On the other hand, the features (ii) from **Fig.6.7** appear in the derivative curves as distinct peaks, that move to lower fields and get weaker with increasing temperature. This feature exhibits a small hysteresis.

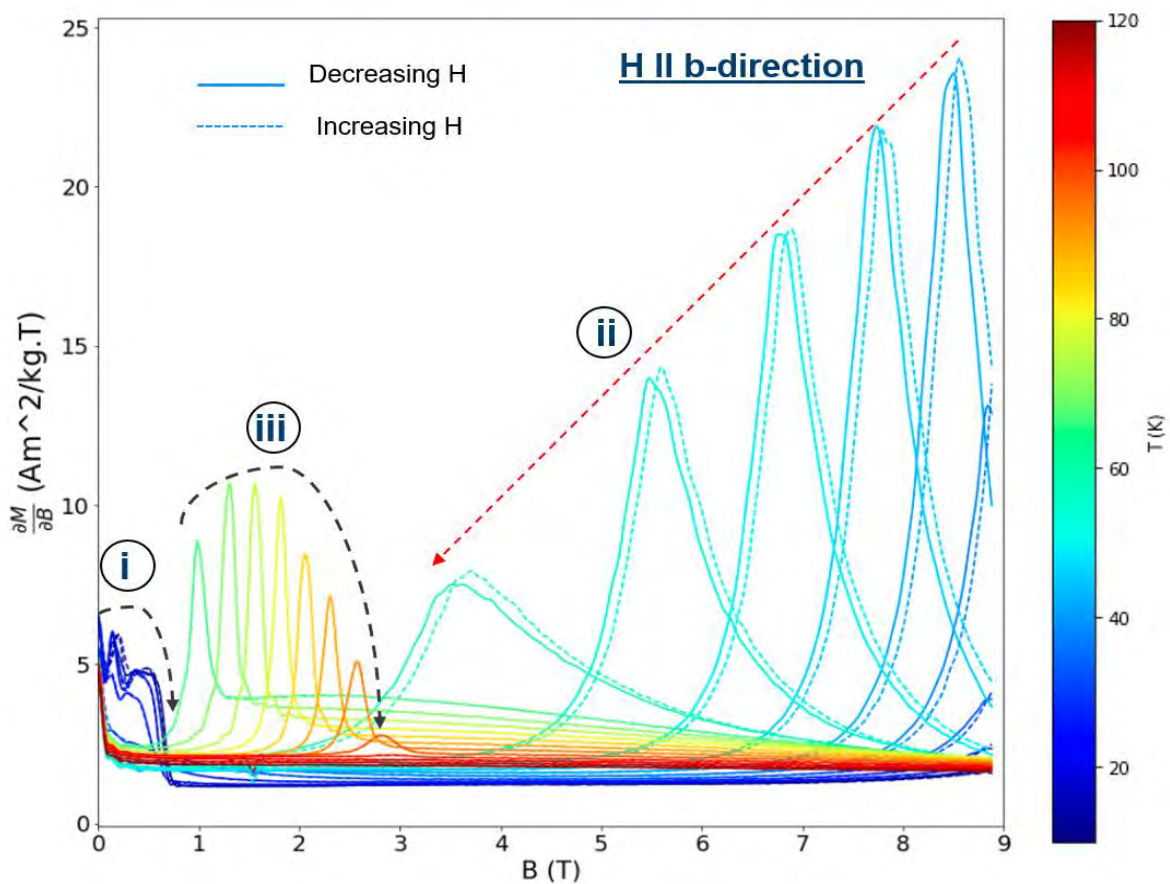


Fig.6.8 The first derivative of the $M(B)$ curves, (dM/dB) vs. (B). (i) the low temperature-low magnetic field observation, (ii) the observations associated with the phase transition of AFM1'-AFM2, and (iii) the features at high temperature and low magnetic field.

The third feature (iii) from **Fig.6.7** is observed as narrow peaks in the field region below 3.0 T and the high temperature range in **Fig.6.8**. It moves towards stronger magnetic fields upon increasing the temperatures and becomes weaker until it eventually vanishes at the transition temperature from AFM2 to the PM phase (100 K).

In **Fig.6.9**, the approximation of (dM/dT) is plotted as a function of the applied magnetic field and the temperature of the material. The blue and red colors indicate negative and positive (dM/dT) , respectively. For the positive part of magnetic field values, there is a change in the value and the sign of the derivatives over the temperature range of (10-120) K. At low magnetic fields and temperatures, the change of the magnetization with respect to change of the temperature is negative. In other words, the magnetization decreases with increasing the temperature. The maximum values of positive derivatives (reddish color) correspond to the steepest points in the temperature-dependent magnetization curves. The boundary line of the transition from the AFM1' to the AFM2 phase appears as a white line where the values of (dM/dT) are zero and correspond to the maximum in the $M(T)$ curves.

The symbols in **Fig.6.9** have been determined from the (dM/dB) curves. The blue stars correspond to the feature (i), blue circles correspond to (ii) observations, and the yellow diamonds correspond to the features (iii) in **Fig.6.7**.

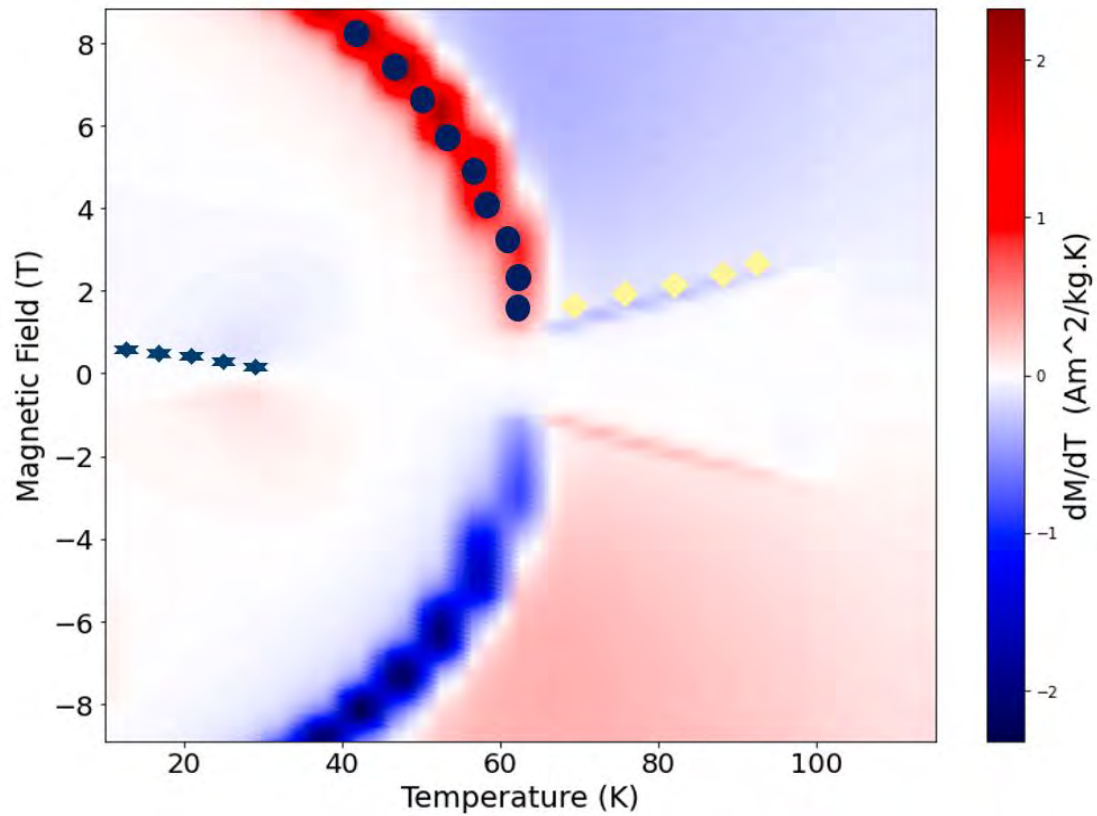


Fig.6.9 (dM/dT) for the magnetization data of Mn_5Si_3 single crystal as a function of applied magnetic field and temperature, H || b-direction. Shades of red and blue represent the positive and negative (dM/dT) of the sweeping down data respectively. The Star symbols represent observations corresponding to feature (i) in Fig.6.7, the filled circles correspond to features (ii), and the yellow diamonds correspond to feature (iii).

6.3.2.2 Magnetization measurements of H || c-direction

The $M(B)$ curves have been measured in the same field range as for the two other measured directions starting from 10 K to 76 K in 3K step (**Fig.6.10**).

Again, the (i) and (ii) features are observed in similar temperature field ranges as before, but an additional new observation (iv) is recorded, which is not observed when the magnetic field is applied in the ab-plane. The observation (iv) appears as a shallow kink in the $M(B)$ curves in the low temperature range (<60 K) and moves towards lower fields with increasing temperature. It is associated with the phase transitions from the AFM1 to the AFM1' phase (**Fig.6.10**)

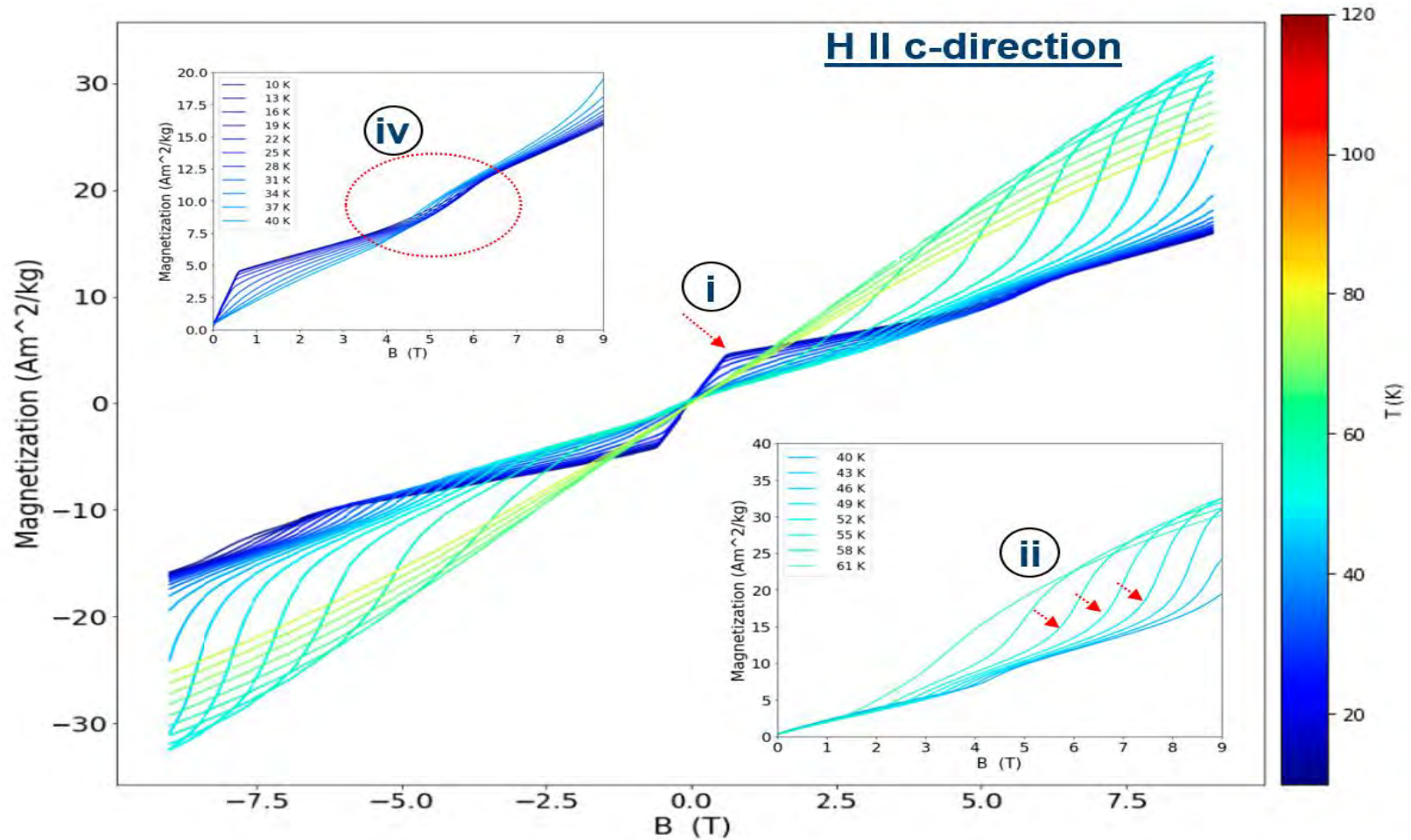


Fig.6.10 The field-dependent magnetization curves ($M(B)$) of Mn_5Si_3 . Decreasing H data, $H \parallel c$ -direction, in the temperature range 10 K - 76 K. (i) indicates the low temperature-low magnetic field observations, (ii) represents the observations associated with the phase transition of $AFM1'-AFM2$, and (iv) corresponds to the features associated with the phase transition $AFM1$ to $AFM1'$.

For closer examination of the data, **Fig.6.11** shows the (dM/dB) vs. (B) curves for the three-temperature ranges of interest. The dashed and solid lines correspond to the hysteresis branches with increasing and decreasing field, respectively.

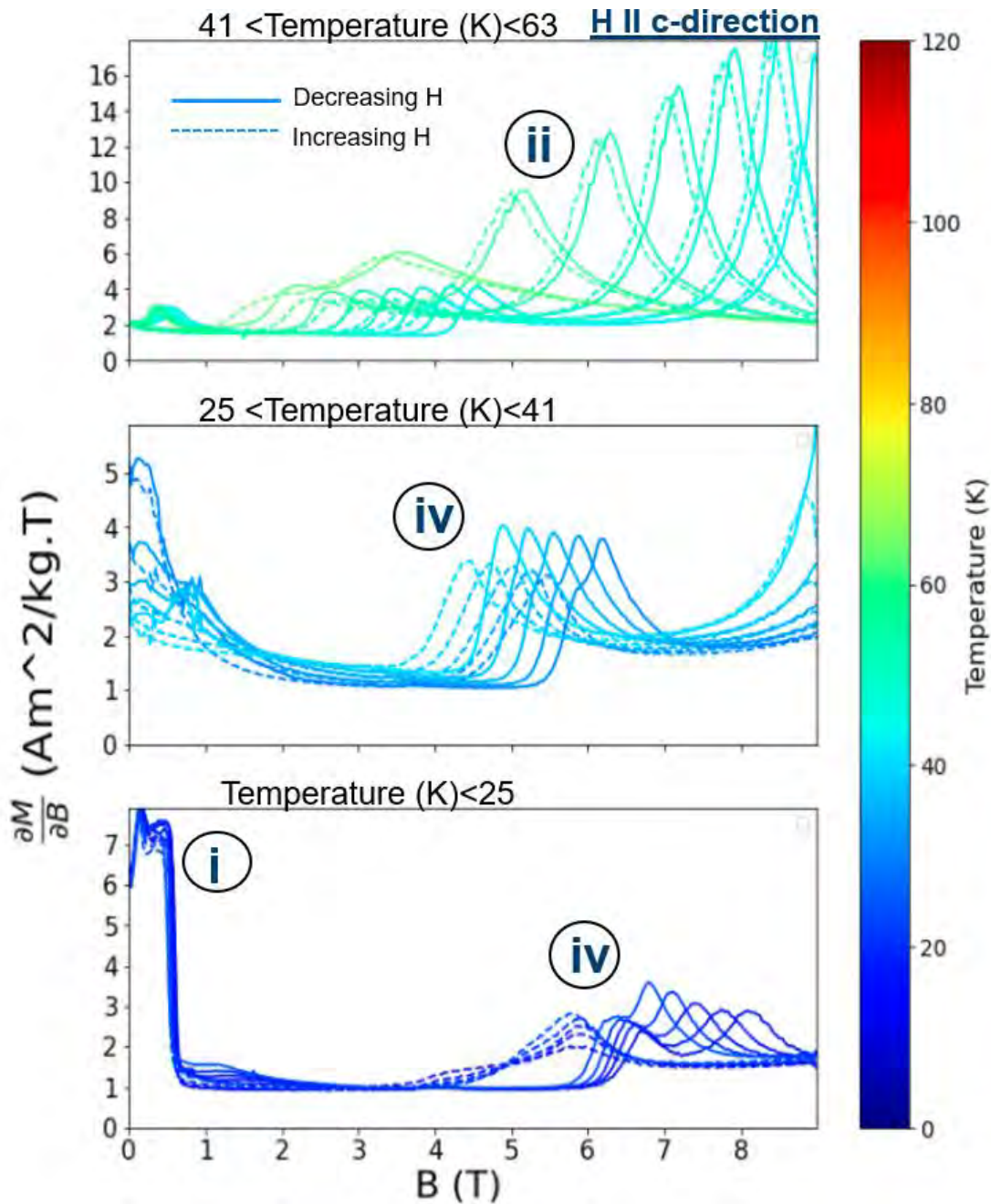


Fig.6.11 The (dM/dB) vs. (B) curves for three temperature ranges, (bottom) $T < 25$ K, (middle) $25 < T(K) < 41$, and (top) $41 < T(K) < 63$. (i) and (ii) features are seen as before in Fig.6.7. (iv) represents the features associated with the phase transition AFM1 to AFM1'.

The lowest temperature region (<25 K) (**Fig.6.11 (bottom)**) is characterized by the feature (i) below 0.8 T, and the feature (iv) which shows a highly asymmetric and hysteric behavior between the two branches of hysteresis loop. For the branch corresponding to the decrease of the field there are two peaks that merge together at around 25 K, and move towards lower field with increasing temperature. With increasing the field, the stronger of the two peaks hardly moves with temperature, while the weaker peak moves towards larger field values. Eventually they merge at around 5.0 T. The (iv) observation is assigned to the phase transition from AFM1 to AFM1'.

At the intermediate temperature region ($25 < T(K) < 41$) (**Fig.6.11 (middle)**), the feature (i) is still observed but the maxima of the peaks decrease with increasing temperature. The feature (iv) has no double peaks any more as they merge together and move towards lower magnetic field values with increasing the temperature. The shift to lower temperature is seen for the positive and the negative sign of the field change. The peak height varies only slightly in this temperature range.

For higher temperature range ($41 < T(K) < 63$) (**Fig.6.11 (top)**), the feature (ii) which is associated with the magnetic transition from the AFM1' to the AFM2 phase, becomes visible. The peaks move towards lower field values and get weaker with increasing temperature. Feature (iv) moves also to lower fields, but the changes in peak height are only minor. Other distinct peaks appear below 1.0 T, yet they begin to flatten and disappear when the temperature of 61 K is approached.

Above 61 K, all the features disappear and the magnetic response with the field H applied || to the c-direction looks paramagnetic.

Fig.6.12 shows the (dM/dT) of the magnetization data as a function of the applied magnetic field and the temperature of the material. The phase transitions correspond to points where the derivative is zero and appear as white lines., indicating maxima or minima in $M(T)$. The symbols in the figure have been determined from the (dM/dB) curves, the blue stars correspond to the features (i) of low temperatures and low magnetic fields, while the filled circles correspond to features (ii) that are associated with the phase transition from the AFM1' to the AFM2 phase. The filled triangles correspond to features (iv) which are associated with the phase transition from the AFM1 to the AFM1' phase.

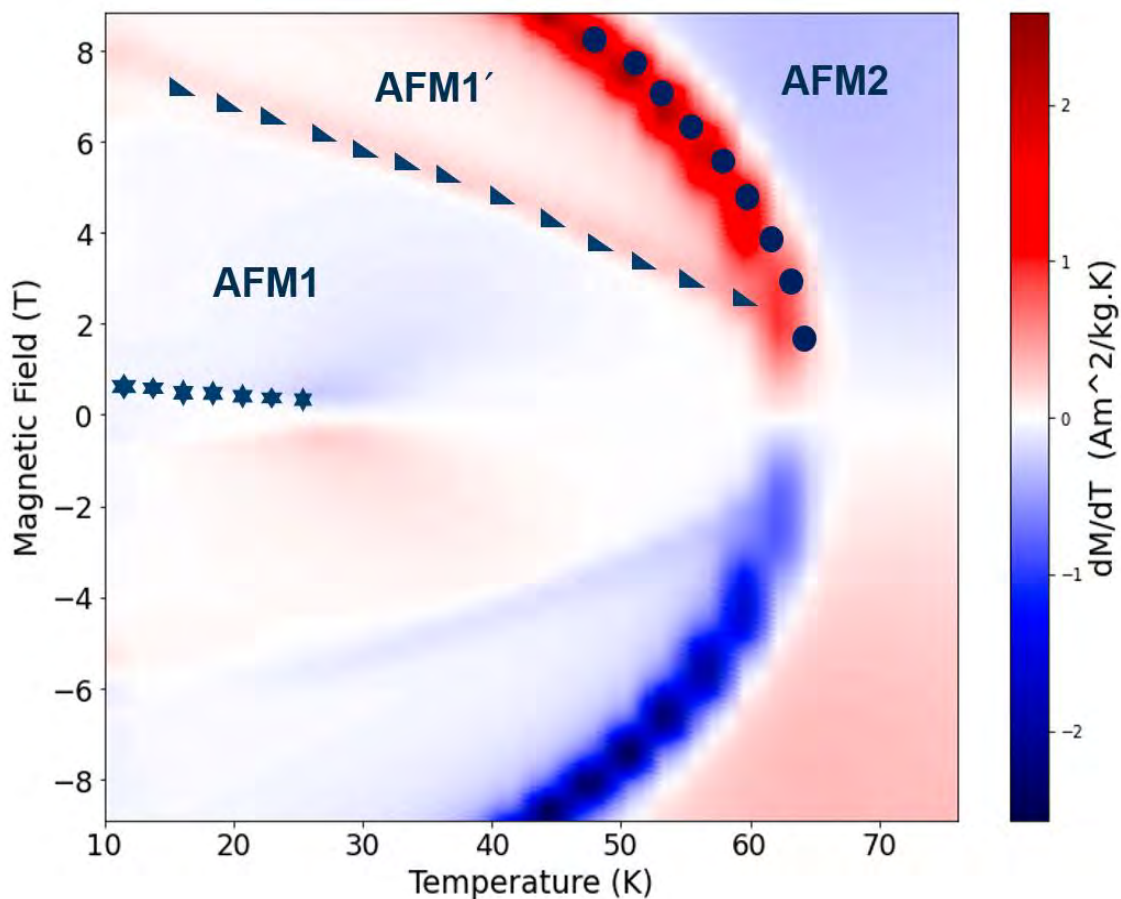


Fig.6.12 The (dM/dT) of the magnetization data of Mn_5Si_3 single crystal as a function of the magnetic field applied \parallel to the c-direction and the temperature. Shades of red and blue represent positive and negative (dM/dT) of the sweeping down data respectively. The star symbols represent feature (i). The filled circles correspond to feature (ii). The filled triangles correspond to feature (iv) associated with the phase transition from the AFM1 to the AFM1'.

For the purpose of investigating the magnetic response to the temperature-field protocol, we compared the isofield data to the data points obtained from the isothermal measurements at the corresponding magnetic fields (**Fig.6.13**), taking into account both signs of the field change. From this comparison, one can see that only if the field is applied $\parallel c$, the thermomagnetic history plays a role. For decreasing field, isofield and isothermal data match reasonably well, while for the isothermal data measured at increasing field, features have a distinct minimum at ~ 40 K.

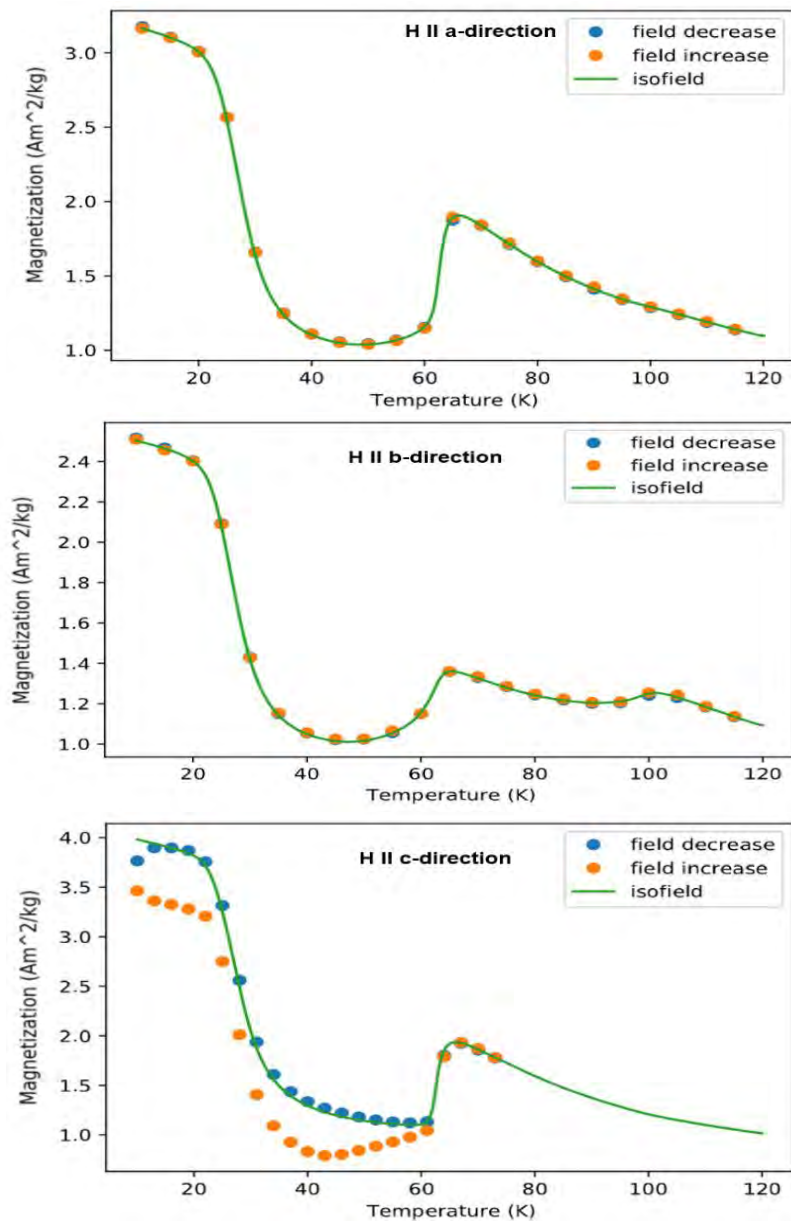


Fig.6.13 The Isofield magnetization data at 0.5 T, with the field applied \parallel to the three different directions a, b, and c. The dots in orange and blue correspond to the magnetization data which are extracted from the isothermal measurements at 0.5 T during increase and decrease of the magnetic field respectively.

6.3.3 Characterization of the MCE

In this thesis, the isothermal entropy change $\Delta S_M(T, \Delta H)$ is used to characterize the MCE. According to the Maxwell relation, the isothermal entropy change can be calculated from the change of the magnetization as a function of temperature under isofield conditions. Numerically, integrating Eq.4 (see theory part) will produce a quantitative value of ΔS_M .

As shown in **Fig.6.13**, the value of the magnetization under isofield conditions was extracted from the data that was measured at isothermal conditions. The data measured upon decreasing field was used for the previous extraction. A 2d-interpolation was performed for all the measured magnetization curves at decreasing field using the respective class from the SciPy module [69]. Then, the interpolated object was evaluated on a regular grid covering the range for which the isothermal entropy change was calculated. The step size for the interpolation is $\Delta T = 2.5$ K and $\mu_0 \Delta H = 0.5$ T. On this grid, the $\partial M / \partial T$ was approximated numerically:

$$\left(\frac{\Delta M}{\Delta T}\right)_{ij} = \frac{(M_{ij+1} - M_{ij})}{(T_{j+1} - T_j)} \quad (10)$$

where, i : is an index that runs over the magnetic field dimension of the grid, and j over the temperature. Then, the isothermal magnetic entropy change ΔS_{iso} is estimated by the numerical integration as follows:

$$\Delta S_{iso,j} = \mu_0 \sum_i \frac{\Delta M}{\Delta T} \Delta H_i \quad (11)$$

where i : is the index of the data points from the zero field to the field for which the entropy change was calculated.

Fig.6.14 shows the magnetic entropy change of Mn_5Si_3 as a function of the temperature in the field change of 5.0 T for H || b and H || c, respectively. The 5.0T field change is used here to compare with previous results in Refs.[16, 23].

The magnetic entropy changes ($-\Delta S_M$) or (ΔS_{iso}) is increased upon application of the magnetic field. A strong inverse MCE is observed for both field directions close to the

transition from the AFM1' to the AFM2. For temperatures further away from this transition temperature, one observes a small direct MCE (**Fig.6.14**).

Eq. 9 was also evaluated for a smaller field change of 1.0 T. If the field is applied \parallel b, a small inverse MCE is then also observable at the transition AFM2 to PM, (see **Fig.6.15**).

If one compares the MCE for the field applied in the two different directions b and c (**Fig.6.15**), the small difference which is observed at the transition AFM1'-AFM2 phase, might be a spurious effect due to the larger temperature step size of the isothermal measurements, which might result in a reduced slope. **Figs.6.5** and **6.6** show that dM/dT hardly varies for these two directions and we therefore expect a similar MCE for both of them.

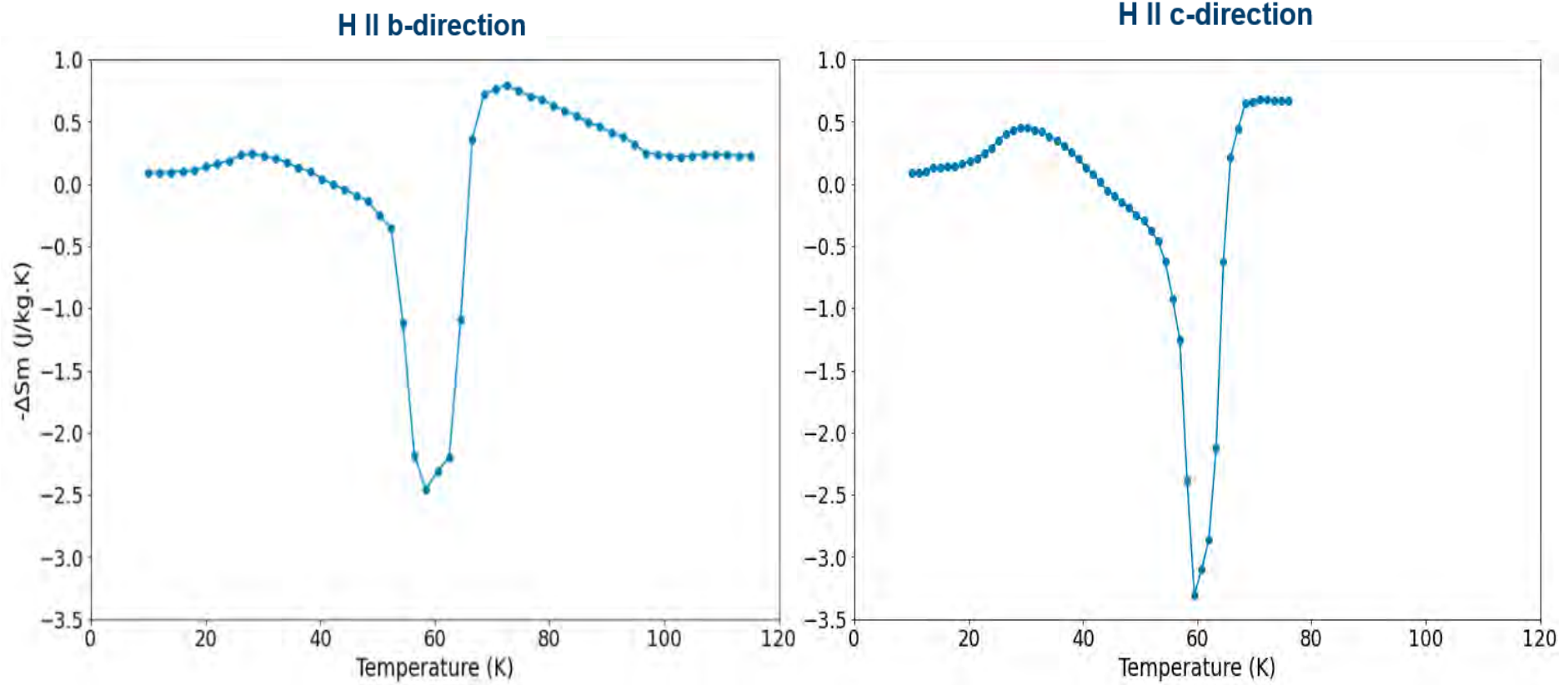


Fig.6.14 Magnetic entropy change ($-\Delta S_M$) of Mn_5Si_3 as a function of temperature, for a field change of 5.0 T; (left) H II b, (right) H II c.

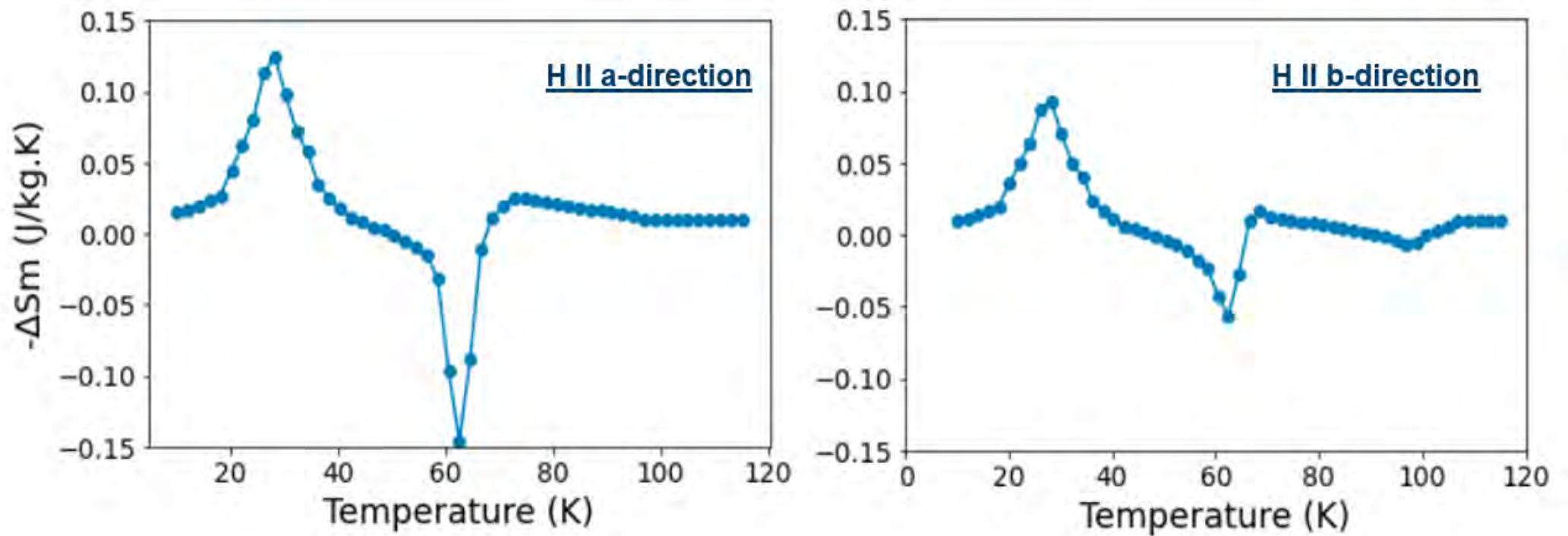


Fig.6.15 Magnetic entropy change ($-\Delta S_M$) of Mn_5Si_3 as a function of temperature, for a field change of 1.0 T; (left) H II a, (right) H II b-direction.

6.4 Magnetization measurements on $Mn_{4.2}Ge_{2.4}Fe_{0.8}Si_{0.6}$

6.4.1 The previous work results

Mass magnetization measurements of $(Mn_5Ge_3)_x(MnFe_4Si_3)_{1-x}$ for $(x = 0.8, 0.6, 0.4, 0.2)$ were performed earlier by K. Al-Namourah [9]. The polycrystalline samples were prepared from stoichiometric amounts of high purity materials using cold crucible induction melting. X-ray powder diffraction was used to check the phase purity of the samples. DC field magnetization measurements were performed to determine the macroscopic magnetic characteristics of the compound. Two types of measurements were performed: isofield measurements where the data was recorded upon cooling (field cooling (FC)) and warming (field warming (FW)) field, and isothermal measurements. In FC mode, the powder samples were cooled continuously from 390 K to 20 K in a magnetic field of $\mu_0H = 0.1$ T. Full hysteresis measurements (± 8 T) were performed upon cooling. Finally, data were measured in the FW mode, in which the magnetic field was set to 0.1 T and the measurements were taken during warming the samples from 20 K to 390 K.

The temperature dependence of the magnetization of the four samples ($x = 0.8, 0.6, 0.4, 0.2$) are shown in **Fig.6.16**. The figure was taken from the former Master thesis. According to these measurements, for $(Mn_{4.2}Ge_{2.4}Fe_{0.8}Si_{0.6})$ in which ($x = 0.8$), the saturation magnetization value is doubled compared to the other samples of ($x = 0.6, 0.4, 0.2$). This magnetization is not compatible with a fully ordered spin moment. Therefore, within this thesis this was cross checked to see whether the result is reproducible or whether an error occurred during the implementation of the former measurements.

For the field dependent magnetization measurements (isothermal), the results from the former Master thesis are shown in **Fig.6.17**. Again, the magnetization for the compound $Mn_{4.2}Ge_{2.4}Fe_{0.8}Si_{0.6}$ seems too high as it exceeds $250 Am^2Kg^{-1}$ at 20 K.

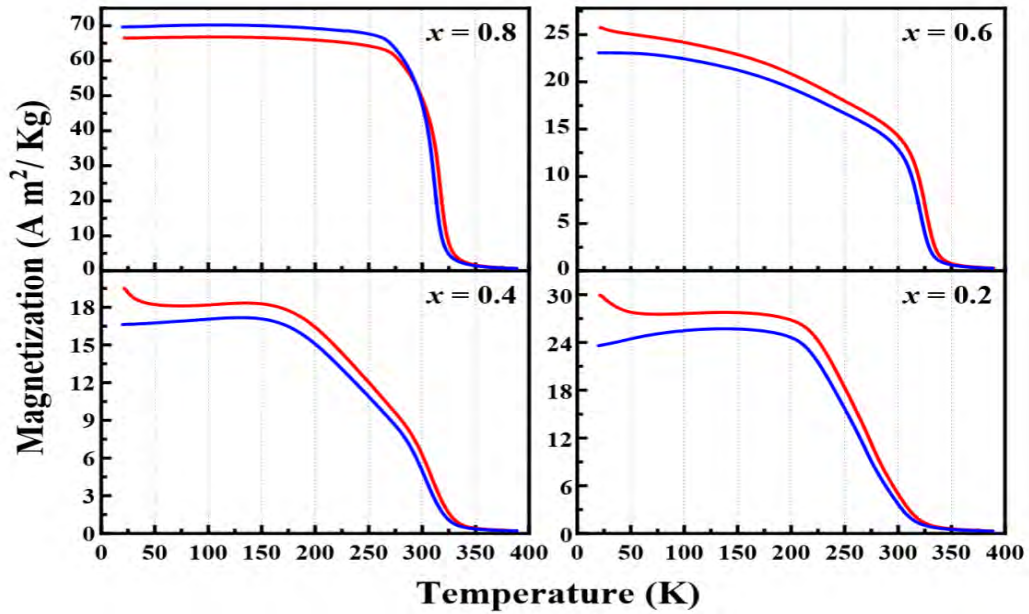


Fig.6.16 Isofield magnetization measurements of the compounds in the system $(Mn_5Ge_3)_x(MnFe_4Si_3)_{1-x}$ measured in $\mu_0H = 0.1 T$, FC mode is the blue color, FW mode is the red color, taken from [9].

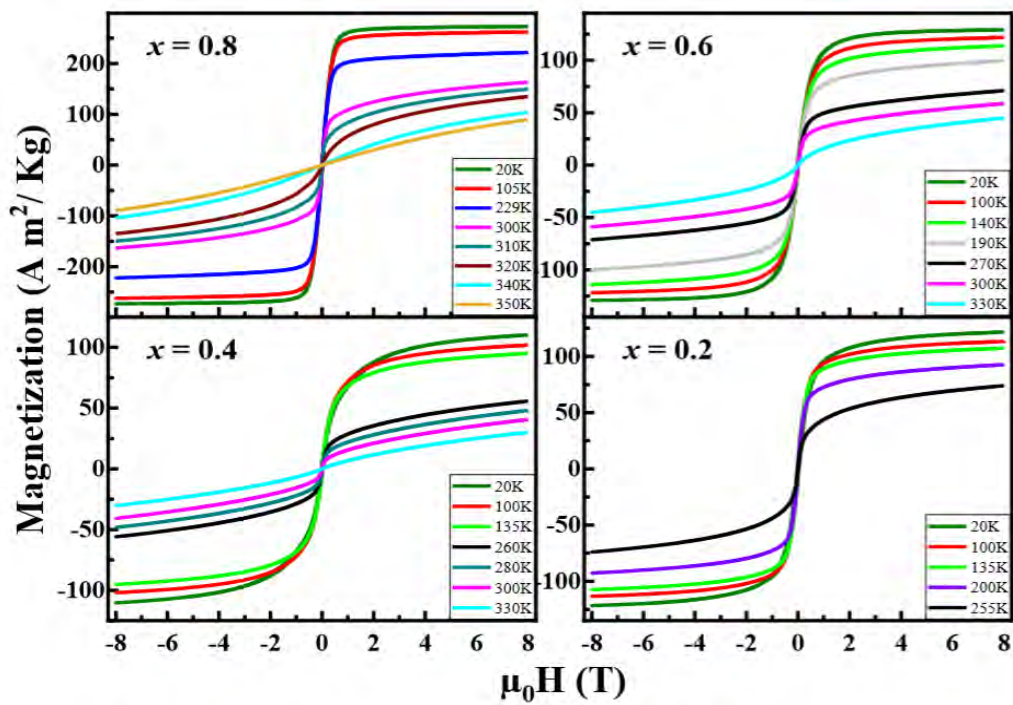


Fig.6.17 Isothermal magnetization measurements of the compounds in the system $(Mn_5Ge_3)_x(MnFe_4Si_3)_{1-x}$. Full hysteresis measurements ($\pm 8 T$) are shown. Figure taken from [9].

6.4.2 Results of the measurements performed in the course of this thesis

In this thesis, the magnetization measurements of $Mn_{4.2}Ge_{2.4}Fe_{0.8}Si_{0.6}$ sample were repeated. **Fig.6.18** illustrates the field dependent measurements in the temperature range from 350 to 20 K. The measurement yields a saturation magnetization of $100 Am^2Kg^{-1}$. This is the same order of magnitude as for the other samples (according to the former master thesis) and in agreement with the maximum moment to be expected from Fe and Mn.

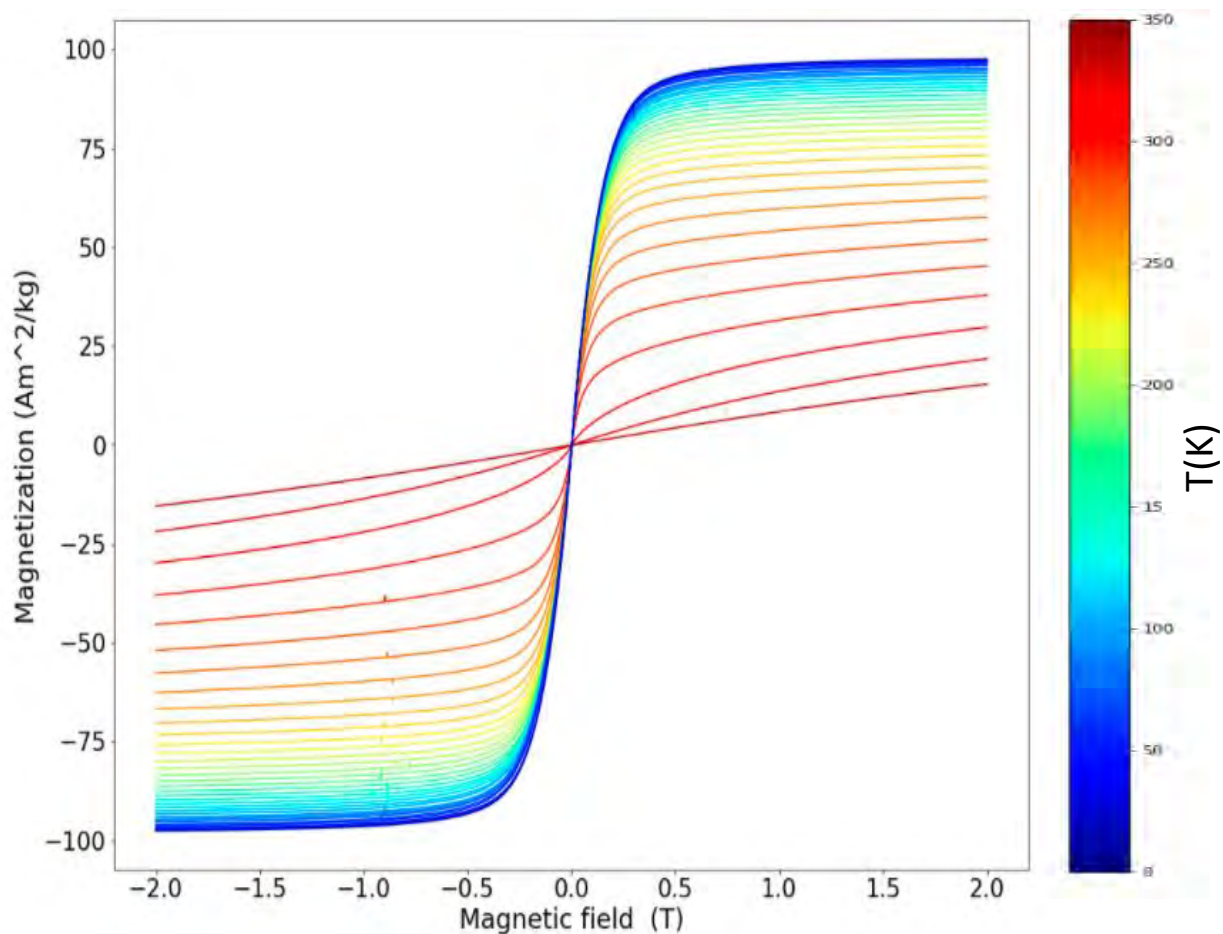


Fig.6.18 Field-dependent magnetization data of a polycrystalline sample of $Mn_{4.2}Ge_{2.4}Fe_{0.8}Si_{0.6}$ in the temperature range from 350 K to 20 K.

On the other hand, the temperature dependence of magnetization measurements of $Mn_{4.2}Ge_{2.4}Fe_{0.8}Si_{0.6}$ were performed at a field setting of 0.1T using the two modes FC and FW (**Fig.6.19**). The obtained value for the saturation magnetization is less than

$50 \text{ Am}^2\text{Kg}^{-1}$, while it was reported $70.0 \text{ Am}^2\text{Kg}^{-1}$ in the former field cooled measurements as presented in [9].

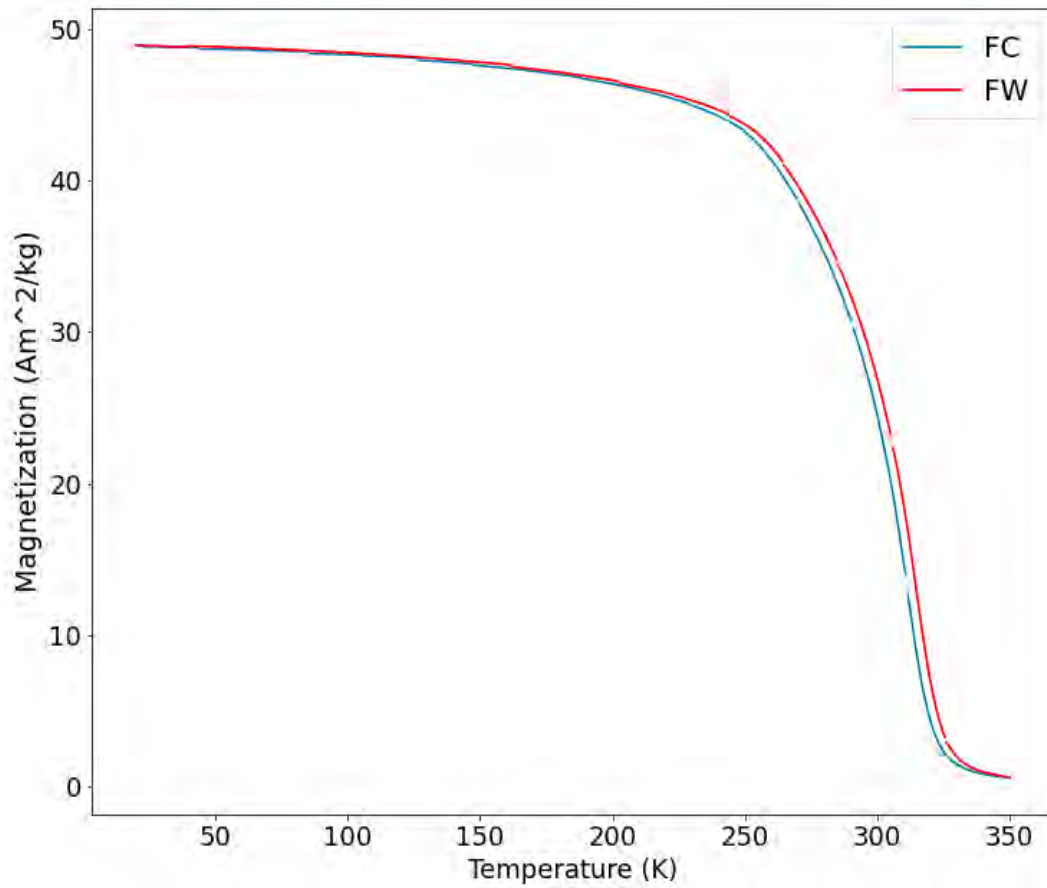


Fig.6.19 Temperature-dependent magnetization data of a polycrystalline sample of $Mn_{4.2}Ge_{2.4}Fe_{0.8}Si_{0.6}$ at a magnetic field setting of 0.1 T.

7 Conclusions and Outlook

The macroscopic magnetic properties of a single crystal of Mn_5Si_3 were investigated using the Vibrating Sample Magnetometer (VSM) option. The direction dependent mass magnetization measurements were performed with the magnetic field applied along the three different crystallographic directions a, b and c of the orthorhombic unit cell. The magnetization measurements were performed for every sample under two different protocols, the isothermal and the isofield conditions. For the measurements with H || a, b directions, the results were very similar but they are clearly different if the field is applied parallel to the c-direction.

Five main observations were obtained from field and temperature dependent magnetization curves (**Table (7.1), Fig.7.1**). The low temperature-low magnetic field feature **(i)** was observed when H || a, b and c directions as well as the features **(ii)** which are associated with the phase transition of AFM1' - AFM2 under the isothermal conditions. On the other hand, we observed the feature **(iii)** when the magnetic field is applied in the ab-plane. Features **(iv)** that are attributed to the transition from AFM1 to the AFM1' phase, were only observed when the magnetic field is applied parallel to the c-direction (**Table (6.2), Fig.7.1**).

The transition from the PM phase to the AFM2 state can only be observed, when small fields are applied || to the b-direction.

Based on what was mentioned previously, it can be concluded that the magnetic response of the sample is strongly affected by the direction of the applied magnetic field.

The described low temperature-low magnetic field features, as well as the high temperatures-low magnetic fields changes (**Fig.7.1**), are discussed for the first time in this thesis. However, a full explanation and understanding of these observations is difficult at the present time. More theoretical or/and experimental investigations will be necessary to obtain the full picture.

Moreover, the MCE of Mn_5Si_3 was characterized by the quantity of ΔS_M based on the Maxwell's relation and calculated from the field-dependent magnetization data. The

compound exhibits an inverse MCE which corroborates the prevalence of AFM interactions. A switch of the sign of magnetic entropy occurs around the transition temperature from the non-collinear AFM to the collinear AFM phase. The maximum positive value of ΔS_M is roughly 3.5 J/kg. K for a field change of 5.0 T at approximately 60 K, when the magnetic field is applied parallel to the c-direction. On the other hand, it is around 2.5 J/kg. K when H in the ab plane.

Table (7.1) Summary of the main anomalies observed in the isothermal and isofield magnetization measurements that were performed on the single crystal of Mn_5Si_3 .

#	The Main observation	H a- direction	H b- direction	H c- direction
(i)	Low temperature-low magnetic field	✓	✓	✓
(ii)	AFM1' - AFM2	✓	✓	✓
(iii)	High temperature -low magnetic field	✓	✓	
(iv)	AFM1 - AFM1'			✓
(v)	PM-AFM2 (Isofield measurements)		✓	

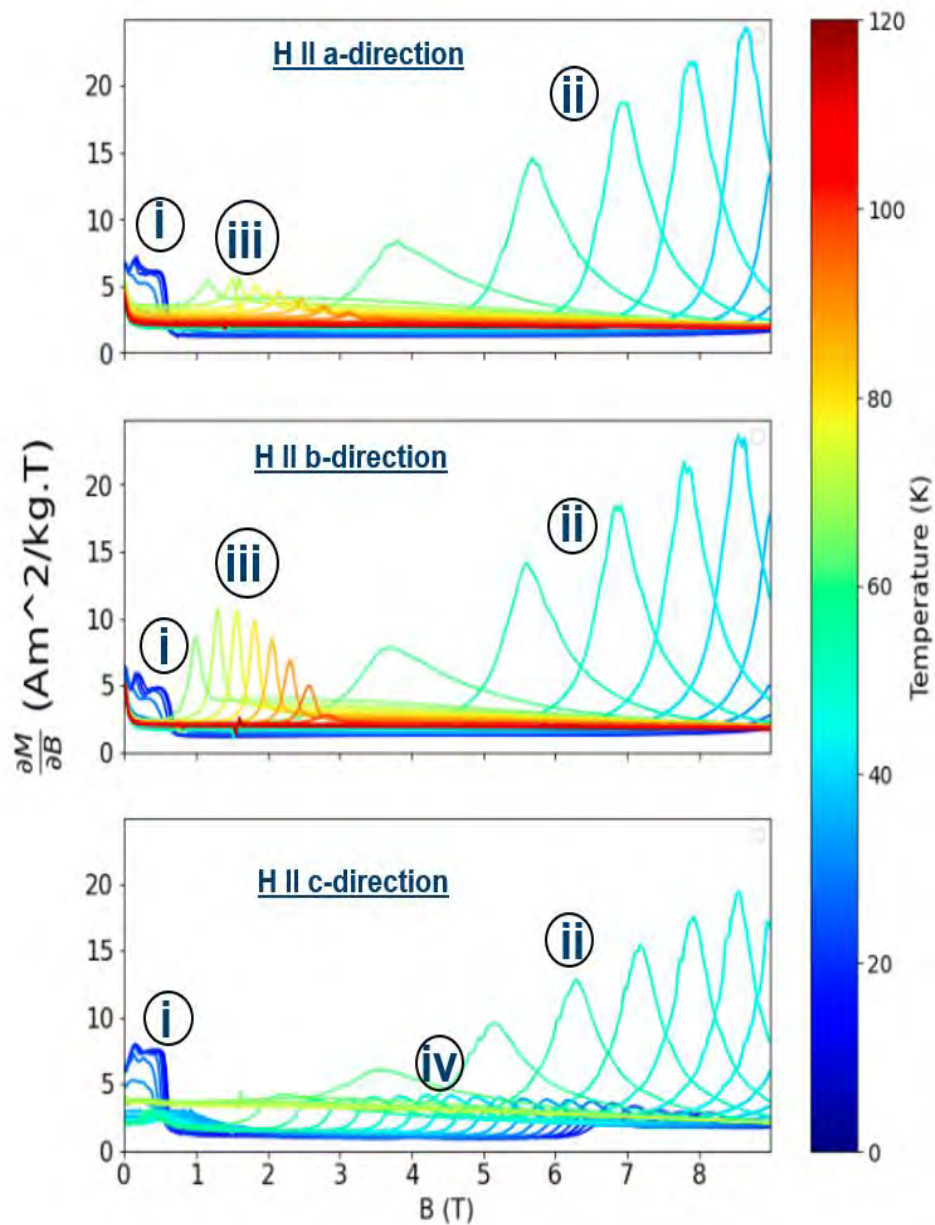


Fig.7.1 The (dM/dB) vs. (B) curves for the a, b, and c-direction. (i) The low temperature-low magnetic field observation. (ii) The observations associated with the phase transition of AFM1'-AFM2. (iii) The features at high temperature-low magnetic field feature. (iv) The features associated with the phase transition AFM1 to AFM1' .

Our results show clearly that the magnetic response in the low temperature phase AMF1 depends strongly on the field direction and is more complex than previously thought. Due to the systematic approach, these data are a solid test ground for any

theory. The data highlight also the insight that can be provided by macroscopic measurements on single crystal samples.

This complexity of the magnetic response of Mn_5Si_3 is partly due to the existence of two different crystallographic sites which are occupied by the Mn ions. By applying a magnetic field that some of the anti-parallel aligned Mn1 and Mn2 spins are decoupled which results in increasing disorder of the spin system. This increases the magnetic entropy, and causes the inverse MCE.

In a related work on $Mn_3Fe_2Si_3$ [70], it was found that the moments on the Mn1 sites are ordered in the AFM2 phase and cannot fluctuate. Macroscopically this compound does not show feature (iii) which is related to the transition from AFM1 to AFM2, and the MCE is about 10 times smaller.

Based on the above, the importance of the existence of two independent magnetic sites for the MCE is highlighted. This strongly suggests focusing the search for suitable magnetocaloric materials on compounds with different sites for the magnetic ions.

Regarding the $(Mn_5Ge_3)_x(MnFe_4Si_3)_{1-x}$ compound in powder form, there was a doubt about the reliability of the earlier magnetization results of the sample with $x = 0.8$ for which the saturation magnetization value exceeded $250 \text{ Am}^2\text{Kg}^{-1}$ at 20 K, compared to the much lower saturation magnetization of approximately $100 \text{ Am}^2\text{Kg}^{-1}$ for the other samples with $x = 0.6, 0.4, 0.2$. To check this observation, a polycrystalline sample of $Mn_{4.2}Ge_{2.4}Fe_{0.8}Si_{0.6}$ was re-synthesized. Then x-ray powder diffraction confirmed the phase purity of the compound. Afterwards, the magnetization was re-measured by performing isofield measurements with two modes: field cooling (FC) and field warming (FW), and isothermal measurements over a temperature range from 350 to 20 K. We find that the saturation magnetization at 20 K is around $100 \text{ Am}^2\text{Kg}^{-1}$ as expected, and that evidently the formerly reported value of $250 \text{ Am}^2\text{Kg}^{-1}$ is erroneous.

References

1. Gottschilch, M., et al., *Study of the antiferromagnetism of Mn₅Si₃: an inverse magnetocaloric effect material*. Journal of Materials Chemistry, 2012. **22**(30): p. 15275-15284.
2. Luccas, R.F., et al., *Magnetic phase diagram, magnetotransport and inverse magnetocaloric effect in the noncollinear antiferromagnet Mn₅Si₃*. Journal of Magnetism and Magnetic Materials, 2019. **489**: p. 7.
3. Gier, H., M.B.a., *private communication*, Forschungszentrum Jülich GmbH. 2014.
4. Neef, C., *F69 - Laue X-ray Diffraction*. 2015.
5. Behera, G., *Structural, Magnetic and Dielectric Investigation of Iron Tellurate Fe₂TeO₆*. 2016.
6. Sochi, T., *High throughput software for powder diffraction and its application to heterogeneous catalysis*. arXiv preprint arXiv:1012.4506, 2010.
7. Pecharsky, V.K. and K.A. Gschneidner Jr, *Magnetocaloric effect and magnetic refrigeration*. Journal of magnetism and magnetic materials, 1999. **200**(1-3): p. 44-56.
8. Ståhl, K., *The Huber G670 imaging-plate Guinier camera tested on beamline I711 at the MAX II synchrotron*. Journal of applied crystallography, 2000. **33**(2): p. 394-396.
9. Al-Namourah, K.K.J., *Synthesis, Magnetic Properties, and Crystal Structures of Magnetocaloric Materials in the System (Mn₅Ge₃)_x(MnFe₄Si₃)_{1-x}*, in *Deanship of Graduate Studies Al-Quds University*
10. Franco, V., et al., *The magnetocaloric effect and magnetic refrigeration near room temperature: materials and models*. Annual Review of Materials Research, 2012. **42**.
11. Alkanani, H.J. and J.G. Booth, *Magnetic-field-induced transitions in Mn₅Si₃*. Journal of Magnetism and Magnetic Materials, 1995. **140**: p. 1539-1540.
12. Sürgers, C., et al., *Large topological Hall effect in the non-collinear phase of an antiferromagnet*. Nature Communications, 2014. **5**.
13. Sürgers, C., et al., *Switching of a large anomalous Hall effect between metamagnetic phases of a non-collinear antiferromagnet*. 2017. **7**: p. 42982.
14. Tegus, O., et al., *Magnetic-phase transitions and magnetocaloric effects*. Physica B: Condensed Matter, 2002. **319**(1): p. 174-192.
15. Brown, P.J. and J.B. Forsyth, *Antiferromagnetism in Mn₅Si₃ - the Magnetic-Structure of the Af₂ Phase at 70 K*. Journal of Physics-Condensed Matter, 1995. **7**(39): p. 7619-7628.
16. Songlin, et al., *Magnetic phase transition and magnetocaloric effect in Mn₅-xFe_xSi₃*. Journal of Alloys and Compounds, 2002. **334**: p. 249-252.
17. Franco, V., et al., *Magnetocaloric effect: From materials research to refrigeration devices*. Progress in Materials Science, 2018. **93**: p. 112-232.
18. Villars, P. and L.J.A.S.o.M. Calvert, Cleveland, OH, *Pearson's Handbook of Crystallographic Data for Intermediate Phases*. 1985.
19. Menshikov, A.Z., A.P. Vokhmyanin, and Y.A. Dorofeev, *Magnetic-Structure and Phase-Transformations in Mn₅Si₃*. Physica Status Solidi B-Basic Research, 1990. **158**(1): p. 319-328.
20. Kappel, G., G. Fischer, and A.J.p.s.s. Jaegle, *Magnetic investigation of the system Mn₅Ge₃□ Mn₅Si₃*. 1976. **34**(2): p. 691-696.
21. Aronsson, B., *A NOTE ON THE COMPOSITIONS AND CRYSTAL STRUCTURES OF MNB₂ MN₃SI MN₅SI₃ AND FESI₂*. Acta Chemica Scandinavica, 1960. **14**(6): p. 1414-1418.
22. Lander, G.H., P.J. Brown, and J.B. Forsyth, *ANTIFERROMAGNETIC STRUCTURE OF MN₅SI₃*. Proceedings of the Physical Society of London, 1967. **91**(572P): p. 332-&.
23. Tegus, O., et al., *Magnetic and magnetocaloric properties of Mn₅Ge₃- xSbx*. Journal of Alloys and Compounds, 2002. **337**(1-2): p. 269-271.
24. Sürgers, C., et al., *Large topological Hall effect in the non-collinear phase of an antiferromagnet*. Nature communications, 2014. **5**(1): p. 1-8.

25. Surgers, C., et al., *Anomalous Hall effect in the noncollinear antiferromagnet Mn₅Si₃*. Aip Advances, 2016. **6**(5).
26. Warburg, E., *Magnetische Untersuchungen*. Annalen der Physik, 1881. **249**(5): p. 141-164.
27. Weiss, P. and A. Piccard, *Le phénomène magnétocalorique*. J. Phys. Theor. Appl., 1917. **7**(1): p. 103-109.
28. Zemansky, M.W., *Temperatures very low and very high*. 1981: Courier Corporation.
29. Giauque, W. and D. MacDougall, *Attainment of Temperatures Below 1 Absolute by Demagnetization of Gd₂(SO₄)₃·8H₂O*. Physical Review, 1933. **43**(9): p. 768.
30. Jr., K.A.G. and V.K. Pecharsky, *Magnetic refrigeration materials (invited)*. Journal of Applied Physics, 1999. **85**(8): p. 5365-5368.
31. Zimm, C., et al., *Description and performance of a near-room temperature magnetic refrigerator*, in *Advances in cryogenic engineering*. 1998, Springer. p. 1759-1766.
32. Pecharsky, V.K. and K.A. Gschneidner Jr, *Giant magnetocaloric effect in Gd₅(Si₂Ge₂)*. Physical review letters, 1997. **78**(23): p. 4494.
33. Franco, V., et al., *Magnetocaloric effect: From materials research to refrigeration devices*. Progress in Materials Science, 2018. **93**: p. 112-232.
34. Yu, B.F., et al., *Review on research of room temperature magnetic refrigeration*. International Journal of Refrigeration, 2003. **26**(6): p. 622-636.
35. Morrish, A.H., *The physical principles of magnetism*. 2001.
36. Zhang, Y.Q. and Z.D. Zhang, *Giant magnetoresistance and magnetocaloric effects of the Mn₁₋₈₂V₀₋₁₈Sb compound*. Journal of alloys and compounds, 2004. **365**(1-2): p. 35-38.
37. Nikitin, S., et al., *The magnetocaloric effect in Fe₄₉Rh₅₁ compound*. Physics Letters A, 1990. **148**(6-7): p. 363-366.
38. Pareti, L., et al., *Giant entropy change at the co-occurrence of structural and magnetic transitions in the Ni Mn Ga Heusler alloy*. The European Physical Journal B-Condensed Matter and Complex Systems, 2003. **32**(3): p. 303-307.
39. Dan'kov, S.Y., et al., *Experimental device for studying the magnetocaloric effect in pulse magnetic fields*. Review of scientific instruments, 1997. **68**(6): p. 2432-2437.
40. Jeppesen, S., et al., *Indirect measurement of the magnetocaloric effect using a novel differential scanning calorimeter with magnetic field*. Review of Scientific Instruments, 2008. **79**(8): p. 083901.
41. Földeàki, M., R. Chahine, and T. Bose, *Magnetic measurements: A powerful tool in magnetic refrigerator design*. Journal of applied physics, 1995. **77**(7): p. 3528-3537.
42. Franco, V., *Determination of the Magnetic Entropy Change from Magnetic Measurements*.
43. Whittig, L. and W. Allardice, *X-ray diffraction techniques*. Methods of Soil Analysis: Part 1 Physical and Mineralogical Methods, 1986. **5**: p. 331-362.
44. Birkholz, M., *Thin film analysis by X-ray scattering*. 2006: John Wiley & Sons.
45. Cullity, B.D., *Elements of X-ray Diffraction*. 1956: Addison-Wesley Publishing.
46. Le Bail, A., H. Duroy, and J.L. Fourquet, *Ab-initio structure determination of LiSbWO₆ by X-ray powder diffraction*. Materials Research Bulletin, 1988. **23**(3): p. 447-452.
47. Doebelin, N. and R. Kleeberg, *Profex: a graphical user interface for the Rietveld refinement program BGMN*. Journal of applied crystallography, 2015. **48**(5): p. 1573-1580.
48. Ebeid, M., et al., *Verification of crystallite theory of glass modeling using Rietveld method*. Egypt, J. Sol, 2000. **23**(1).
49. Rodríguez-Carvajal, J., *An introduction to the program FullProf*. Laboratoire Leon Brillouin (CEA-CNRS), 2001.
50. Petricek, V., M. Dusek, and L. Palatinus, *JANA: Crystallographic Computing System for Standard and Modulated Structures*. 2006.
51. Bińczycka, H., et al., *Atomic and magnetic structure of Mn_{5-x}FexSi₃*. Physica status solidi (a), 1973. **19**(1): p. K13-K17.

52. Johnson, V., et al., *Magnetic and Mössbauer effect studies of Mn₅Si₃: Fe₅Si₃ solid solutions*. Journal of Solid State Chemistry, 1972. **4**(2): p. 311-323.
53. Bińczycka, H., et al., *Atomic and magnetic structure of Mn_{5-x}Fe_xSi₃*. 1973. **19**(1): p. K13-K17.
54. Ciszewski, R., *Magnetic Structure of the Mn₅Ge₃ Alloy*. physica status solidi (b), 1963. **3**(11): p. 1999-2004.
55. Aronsson, B., *Borides and silicides of the transition metals*. Arkiv Kemi, 1960. **16**.
56. Brown, P.J., et al., *THE LOW-TEMPERATURE ANTIFERROMAGNETIC STRUCTURE OF MN₅Si₃ REVISITED IN THE LIGHT OF NEUTRON POLARIMETRY*. Journal of Physics-Condensed Matter, 1992. **4**(49): p. 10025-10036.
57. Vinokurova, L., et al., *Magnetic phase transitions and electronic structure of the manganese silicides*. Journal of Magnetism and Magnetic Materials, 1990. **90-91**: p. 121-125.
58. Silva, M.R., P.J. Brown, and J.B. Forsyth, *Magnetic moments and magnetic site susceptibilities in Mn₅Si₃*. Journal of Physics-Condensed Matter, 2002. **14**(37): p. 8707-8713.
59. Das, S.C., et al., *Observation of inverted hysteresis loop and thermomagnetic irreversibility in the antiferromagnetic Mn₅Si₃ alloy*. Physical Review B, 2019. **100**(2): p. 7.
60. Pericleous, K., et al., *Experimental and numerical study of the cold crucible melting process*. Applied mathematical modelling, 2006. **30**(11): p. 1262-1280.
61. Gombert, D., et al., *Cold-Crucible design parameters for next generation HLW melters*. 2002, Idaho National Engineering and Environmental Laboratory, Idaho Falls, ID (US ...
62. Bilderback, D., *A real-time back-reflection Laue camera*. Journal of Applied Crystallography, 1979. **12**(1): p. 95-98.
63. Guinebretière, R., *X-ray diffraction by polycrystalline materials*. 2013: John Wiley & Sons.
64. [22.3.2021]; Available from: <https://www.fz-juelich.de/jcms/jcms-2/EN/Leistungen/Laboratory-Facilities/MPMS-PPMS-CCMS/node.html>.
65. Tsui, S., *YBCO Magnetic Characterization (Vibrating Sample Magnetometer Option)*.
66. Biniskos, N., et al., *Spin Fluctuations Drive the Inverse Magnetocaloric Effect in Mn₅Si₃*. Physical Review Letters, 2018. **120**(25): p. 6.
67. Czochralski, J., *A new method for the measurement of the crystallization rate of metals*. Zeitschrift für physikalische Chemie, 1918. **92**: p. 219-221.
68. Laugier, J. and B. Bochu, *OrientExpress 3.4*. 2003.
69. [27.4.2021]; Available from: <https://docs.scipy.org/doc/scipy/reference/interpolate.html#module-scipy.interpolate>.
70. Ait Haddouch, M., *private communication, Forschungszentrum Jülich GmbH*. 2014.

لخصائص لمغناطيسية فيزيائية في مركب احادي للبلورة Mn_5Si_3 ومكب انتمش بقية

اعداد نور ثلثت احمد عبوشي

للمخص

في الآونة الأخيرة، فإنك انضمام في دراسة التغيرات في المغناطيسية للمركب (MCE) في المواد عند درجات حرارة منخفضة من شأنها أن تكون ذات أهمية كبيرة، ليس فقط بسبب الخصائص التطبيقية للمركب، بل أيضاً لانعكاساتهم الأثرية على الخصائص الفيزيائية للمواد. في هذا السياق، فإن دراسة الخصائص المغناطيسية للمركب Mn_5Si_3 في درجات حرارة منخفضة من شأنها أن تكون ذات أهمية كبيرة، ليس فقط بسبب الخصائص التطبيقية للمركب، بل أيضاً لانعكاساتهم الأثرية على الخصائص الفيزيائية للمواد. في هذا السياق، فإن دراسة الخصائص المغناطيسية للمركب Mn_5Si_3 في درجات حرارة منخفضة من شأنها أن تكون ذات أهمية كبيرة، ليس فقط بسبب الخصائص التطبيقية للمركب، بل أيضاً لانعكاساتهم الأثرية على الخصائص الفيزيائية للمواد.

ضمن هذه الأطروحة تمت فحص الخصائص المغناطيسية للمركب Mn_5Si_3 في درجات حرارة منخفضة من شأنها أن تكون ذات أهمية كبيرة، ليس فقط بسبب الخصائص التطبيقية للمركب، بل أيضاً لانعكاساتهم الأثرية على الخصائص الفيزيائية للمواد. في هذا السياق، فإن دراسة الخصائص المغناطيسية للمركب Mn_5Si_3 في درجات حرارة منخفضة من شأنها أن تكون ذات أهمية كبيرة، ليس فقط بسبب الخصائص التطبيقية للمركب، بل أيضاً لانعكاساتهم الأثرية على الخصائص الفيزيائية للمواد.

(1) لوحظت تغيرات فيزيائية في المغناطيسية للمركب عند درجات حرارة منخفضة من شأنها أن تكون ذات أهمية كبيرة، ليس فقط بسبب الخصائص التطبيقية للمركب، بل أيضاً لانعكاساتهم الأثرية على الخصائص الفيزيائية للمواد.

(2) لهيزات لم يتنبأ بتطبيق طور AFM1' - AFM2 .

(3) لهيزات في المغناطيسية للمركب عند درجات حرارة عالية من شأنها أن تكون ذات أهمية كبيرة، ليس فقط بسبب الخصائص التطبيقية للمركب، بل أيضاً لانعكاساتهم الأثرية على الخصائص الفيزيائية للمواد.

(4) لهيزات في المغناطيسية للمركب عند درجات حرارة منخفضة من شأنها أن تكون ذات أهمية كبيرة، ليس فقط بسبب الخصائص التطبيقية للمركب، بل أيضاً لانعكاساتهم الأثرية على الخصائص الفيزيائية للمواد.

(5) لهيزات لم يتنبأ بتطبيق طور AFM2 إلى حالة AFM1. لا يمكن ملاحظة ذلك إلا عند تطبيق تحويل غير عادي إلى اتجاه b.

بناءً على هذه النتائج، يمكن القول بأن الخصائص المغناطيسية للمركب Mn_5Si_3 في درجات حرارة منخفضة من شأنها أن تكون ذات أهمية كبيرة، ليس فقط بسبب الخصائص التطبيقية للمركب، بل أيضاً لانعكاساتهم الأثرية على الخصائص الفيزيائية للمواد.

علاوة على ذلك، تمت حساب تغيرات المغناطيسية للمركب Mn_5Si_3 في درجات حرارة منخفضة من شأنها أن تكون ذات أهمية كبيرة، ليس فقط بسبب الخصائص التطبيقية للمركب، بل أيضاً لانعكاساتهم الأثرية على الخصائص الفيزيائية للمواد.

في ما يتعلق بتركيب المركب $(Mn_5Ge_3)_x(MnFe_4Si_3)_{1-x}$ في شكل مسحوق، فإن اكتشاف حلي موثوق به في التركيب $x = 0.8$ فوق الترددات المنخفضة من شأنها أن تكون ذات أهمية كبيرة، ليس فقط بسبب الخصائص التطبيقية للمركب، بل أيضاً لانعكاساتهم الأثرية على الخصائص الفيزيائية للمواد.

لنلاحظ من هذه الملاحظة أن الخصائص المغناطيسية للمركب $Mn_4.2Ge_2.4Fe_{0.8}Si_{0.6}$ في درجات حرارة منخفضة من شأنها أن تكون ذات أهمية كبيرة، ليس فقط بسبب الخصائص التطبيقية للمركب، بل أيضاً لانعكاساتهم الأثرية على الخصائص الفيزيائية للمواد.

كل سنتي ج م في التركيب $100 Am^2 Kg^{-1}$ عند درجة حرارة $250 Am^2 Kg^{-1}$ في التركيب $100 Am^2 Kg^{-1}$.